

MAGYAR ÁLLAMI  
EÖTVÖS LORÁND  
GEOFIZIKAI INTÉZET

# GEOFIZIKAI KÖZLEMÉNYEK

ВЕНГЕРСКИЙ  
ГЕОФИЗИЧЕСКИЙ  
ИНСТИТУТ  
ИМ Л. ЭТВЕША

ГЕОФИЗИЧЕСКИЙ  
БЮЛЛЕТЕНЬ

# GEOPHYSICAL

T R A N S A C T I O N S

EÖTVÖS LORÁND GEOPHYSICAL INSTITUTE OF HUNGARY

## CONTENTS

Sequence stratigraphic analysis in the South Transdanubian region, Hungary	<i>K. Ujszászi, G. Vakarcs</i>	69
Reflection seismic surveys for oil and gas exploration in north-east Germany	<i>H. Gaertner, K. H. FeBer, W. Küstermann, S. Pröhl, H. Wolff, K. Wruck</i>	89
Seismic signal analysis in partially fluid saturated media	<i>A. A. A. Othman</i>	111
Flow of the Tibetan plateau and tectonics along the Burmese arc	<i>V. P. Singh, D. Shanker</i>	135
Direct interpretation of self-potential anomalies due to spherical structures — A Hilbert transform technique	<i>N. Sundararajan, M. Narasimha Chary</i>	151
Behaviour of SP log in a granite reservoir	<i>A. B. Bourima</i>	167

VOL. 38. NO. 2-3. MARCH 1994. (ISSN 0016-7177)



BUDAPEST

## TARTALOMJEGYZÉK

Szekvenciasztratigráfiai vizsgálatok a Dél-Dunántúlon	<i>Ujszászi K., Vakarcs G.</i>	87
Olaj és gázkutató reflexiós szeizmikus mérések Északkelet-Németországban	<i>H. Gaertner, K. H. FeBer, W. Küstermann, S. Pröhl, H. Wolff, K. Wruck</i>	110
Szeizmikus jel-analízis folyadékkal részlegesen telített közegben	<i>A. A. A. Othman</i>	134
A Tibeti-fennsík eltolódása és tektonikája a Burmai-ív mentén	<i>V. P. Singh, D. Shanker</i>	149
Gömb alakú szerkezetek által keltett sajátpotenciál anomáliák közvetlen értelmezése — egy Hilbert transzformációs eljárás	<i>N. Sundararajan, M. Narasimha Chary</i>	165
SP szelvényezés tulajdonságai gránit tározóban	<i>A. B. Bourima</i>	189

# ESS - 03 - 24

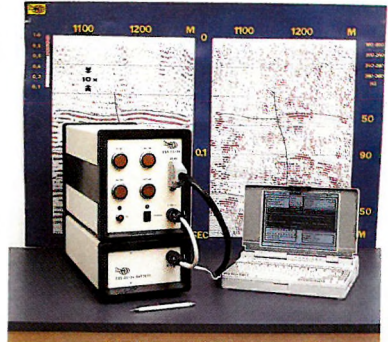
## PC based 24 channel portable seismograph

ESS-03 was designed for high-resolution subsurface imaging using up-to-date electronics and computer technology. Compared with excavation or dense drilling networks, it offers a highly cost-effective solution for geotechnical problems.

It is an excellent tool

- ◆ for raw material prospecting;
- ◆ for determining static corrections for surface seismic methods;
- ◆ for acquiring information when designing large scale foundations such as factories, dams or roads;
- ◆ for seismic investigation of well-sites;
- ◆ for in-mine exploration;
- ◆ for detection of destructive building-vibrations.

ESS-03 can be used not only for rapid and inexpensive data acquisition, but the built-in PC and software package offer excellent on-site processing, quick-look interpretation, and visual display of the results.



### Specifications:

- Frequency response: 1-8000 Hz
- Resolution: 12 bit A/D+42 dB IFP
- Built-in electronic roll along switch
- Microprocessor control 80386-SX-20
- Data recording on floppy disc 1.44 MB,  
hard disc 80 MB
- Menu-driven operating commands
- LCD display with VGA resolution
- Self-testing programs and parameter checking
- Weight: 10 kg
- Dimensions: 200\*220\*450 mm

### Eötvös Loránd Geophysical Institute of Hungary

- Budapest, XIV. Columbus u. 17-23.
- Letters: H-1440 Budapest, POB. 35.
- Phone: (36-1) 184-3309
- Fax: (36-1) 163-7256
- Telex: (61) 22-6194 elgi h
- E-mail: H6123 TIT@ELLA.HU



Founded in 1919

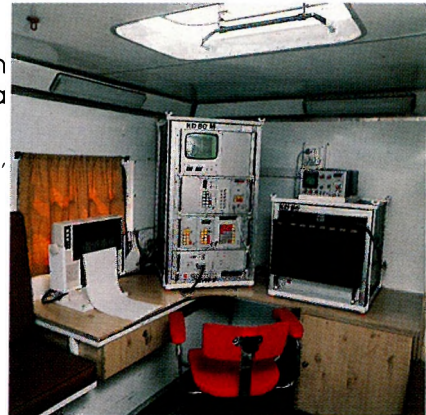
# **DON'T BUY EQUIPMENT OR SERVICES UNTIL YOU KNOW THE FACTS**



ELGI's Well Logging Division has put its 25 years of experience to work again in the new line of well logging technology in  
water,  
coal,  
mineral,  
geotechnical  
prospecting

## **HERE'S WHAT WE OFFER**

- > Complete series of surface instruments from portable models to the PC controlled data logger
- > Sondes for all methods: electrical, nuclear, acoustic, magnetic, mechanical, etc.
- > Depth capacity down to 5000 m
- > On-site or office computer evaluation
- > International Metrological Base for calibration to true petrophysical parameters
- > Training and in-house courses
- > Design laboratory for custom-tailored assemblies



Just think of us as the scientific source of borehole geophysics you may never have heard of

**SALES \* \* \* \* RENTALS \* \* \* \* SERVICES**



**Well Logging Division of ELGI**  
POB 35, Budapest, H-1440 Hungary  
Phone: (361) 252-4999, Telex: 22-6194,  
Fax: (361) 183-7316



# ASSOCIATION OF HUNGARIAN GEOPHYSICISTS

23th ANNUAL MEETING 13-14 October 1994,

## SÁROSPATAK

### CALL FOR PAPERS

The Association of Hungarian Geophysicists in cooperation with the Hungarian Geological Society holds its 23th Annual Meeting on October 13-14, 1994 in the historical city of Sárospatak

*The topics of the Annual Meeting are:*

- Geological-geophysical research in the Pannonian Basin
- Recent advances in geophysical exploration techniques

The deadline of submitting abstracts in English or Hungarian not exceeding 300 words is September 1, 1994. Abstracts should be taped in a 15 x15 cm space as follows:

TITLE

Authors and Institutions

Text

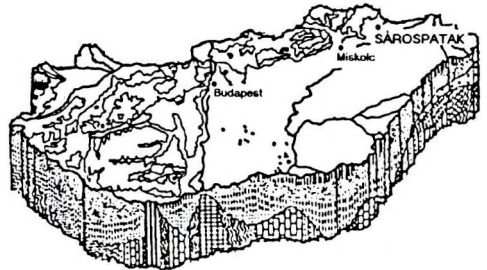
Both poster and oral papers are accepted. The official languages are English and Hungarian.

*For more information please write to our postal address:*

Association of Hungarian Geophysicists  
H-1371 Budapest,  
POB 433  
Hungary  
Fax and phone: 36-1-2019815

or to the

Local Organization Committee  
1994 Meeting of Association of  
Hungarian Geophysicists  
Miskolc University  
Geophysical Department  
H-3515 Miskolc-Egyetemváros  
Fax and phone: 36-46-361936



### REGISTRATION

Registration fee: appr. 6000 HUF (60 USD).

Hotel expenses: appr. 30 USD/night/person.

Registration should be done in letter addressed to the Association of Hungarian Geophysicists before September 5, 1994.

Your registration letter should be accompanied with a copy of the bank transfer order about 60 USD for

MHB Rt  
H-1052 Budapest  
Gerlőczy utca 11.  
323-10195

The Annual Meeting takes place in the City Cultural Centre, where exhibitors are welcome, too.

## INVITATION

The Association of Hungarian Geophysicists decided at its annual meeting to establish the "Foundation for Hungarian Geophysicists" and elected its first Advisory Board for 3 years. The foundation has been started with a moderate initial capital of 300 000 HUF, which has by now increased to more than 3 million and it is open for everybody.

The aim of the foundation is to help Hungarian geophysicists. There are two main target groups whose application for grants will be accepted with preference: young geophysicists needing assistance (travels, participation at conferences, publications, post-graduate education etc.) at the beginning of their professional life as well as retired and unemployed colleagues whose economic and social position became especially unfavourable.

The nine members of the Advisory Board invite everybody to join this foundation; donations should be communicated with the Board. Organisations and persons donating sums exceeding the initial capital will have the opportunity to delegate representatives into the Board. Detailed information is available at the following address:

Advisory Board of the  
"Foundation for Hungarian Geophysicists"  
H-1371 Budapest, P.O.B. 431  
Budapest, I., Fő u. 68.  
Telephone 201-2011/590  
Telex 22-4343  
Telefax 156-1215

## SEQUENCE STRATIGRAPHIC ANALYSIS IN THE SOUTH TRANSDANUBIAN REGION, HUNGARY

Katalin UJSZÁSZI\* and Gábor VAKARCS\*\*

A seismic sequence stratigraphic interpretation of the South Transdanubian region, Hungary, is given showing the first sequence stratigraphic model of this area.

We studied the Middle-Miocene - Pannonian s.l. deposits. From the end of the Middle-Miocene the Pannonian Basin gradually became isolated from the world-ocean. The Neogene sedimentary fill consists of depositional sequences. We identified three synrift and three postrift third-order sequence boundaries. Based on a study of the sedimentary facies of the systems tracts, these sequences show the same characteristics as the marine siliciclastic sequences. These lacustrine sequences are apparently associated with major falls in the water level of the Pannonian Lake and are considered to be third-order sequences. The water level of the Pannonian Lake and its fluctuation were most probably related to the global sea level changes.

**Keywords:** Pannonian Basin, sea level, sequences, systems tract, stratigraphy

### 1. Introduction

The first seismic stratigraphic interpretations of the Neogene infill of the Pannonian Basin were carried out by KÉSMÁRKY et al. [1981], BERKES et al. [1983] and POGÁCSÁS [1984]. In the eastern part of Hungary, MATTICK et al. [1988] did similar research. Later, based on integrated seismic and well-log analysis VAKARCS and VÁRNAI [1991] worked out a sedimentary facies model in eastern Hungary and identified depositional sequences.

POGÁCSÁS et al. [1988] identified four non-depositional hiatuses near the northern margin of the Pannonian Basin, and correlated the stratigraphic

\* MOL Rt. Geophysical Exploration Company, H-1039, Budapest, Batthyány u. 45

\*\* Rice University, Dept. of Geology and Geophysics, Houston, Texas, USA

unconformities with magnetostratigraphic data. POGÁCSÁS and SEIFERT [1991] were the first to apply the sequence stratigraphic method for the Pannonian Basin. TARI et al. [1992] also recognized that the major depositional sequences of non-marine sedimentary fill of the Pannonian Basin can be subdivided into systems tracts defined by stratal pattern. VAKARCS et al. [in press] made the first sequence stratigraphic model of the Pannonian Basin.

The seismic sequence stratigraphic interpretations on the Pannonian Basin published up till now have dealt with the eastern part of the Great Hungarian Plain. On the South Transdanubian region detailed seismic sequence stratigraphic study has not been done yet.

Our interpretation, using the sequence stratigraphic method of VAIL [1987], VAN WAGONER et al. [1987] and VAIL et al. [1991], shows the sequence stratigraphic model of the South Transdanubian region, some identified sequences in this region, in addition we attempt to show the influence of sea level changes on the sedimentary infill of the inland Pannonian Lake.

## 2. Geological setting

In the Preneogene basement there is a main tectonic line in the northern part of the studied area, the so called Balaton line. The basement north of the Balaton line verged here as a result of lateral escape, probably during the Eocene [KÁZMÉR 1984] or Early Miocene [TARI et al. in press]. The basement south of the Balaton line is insufficiently known, it is deep and mainly covered with Miocene volcanics. It can be considered as a huge shear zone. The southern part of this shear zone is of European origin, and probably verged here due to the escape [CSONTOS et al. 1992].

The subject of our study is the Neogene basin infill which deposited on the Preneogene basement.

The Neogene Pannonian Basin is a Mediterranean back-arc basin [BALLY, SNELSON 1980, HORVÁTH et al. 1981]. The opening of the Pannonian Basin in the Neogene was contemporaneous with the last compressional phases of the Outer Carpathians [HORVÁTH et al. 1988]. The main activity period of Neogene extensional fault systems and deformations is called synrift, the following period is called postrift.

## 3. Data set

The reflection seismic data were acquired and processed by the MOL Rt. Geophysical Exploration Company. The interpreted seismic sections were measured between 1980 and 1991, their minimum fold was 24. The well logs were provided by MOL Rt. The chronostratigraphic data adopted in this study

are based on the magnetostratigraphic calibration of the Szombathely-II and Iharosberény-I boreholes of the Hungarian Geological Survey [LANTOS et al. 1990].

#### 4. Sequences

The sequence-boundaries were identified on the basis of VAIL's model [1987] (*Fig. 1*). According to this the sequence boundaries are due to falls in the water level. On the basis of water level changes, the sequences can be divided into systems tracts: lowstand systems tract (LST), transgressive systems tract (TST), highstand systems tract (HST). These systems tracts all have a characteristic seismic reflection configuration and log curve pattern. It is best to integrate these data during interpretation work.

The global sea level curve of HAQ et al. [1987] (*Fig. 2*) shows the major sea level falls of the world-ocean; these falls result in third-order sequences. As a result of our study, we assume that the identified third-order sequence boundaries show strong correlation with the sea level falls of the HAQ et al. [1987] global sea level change curve.

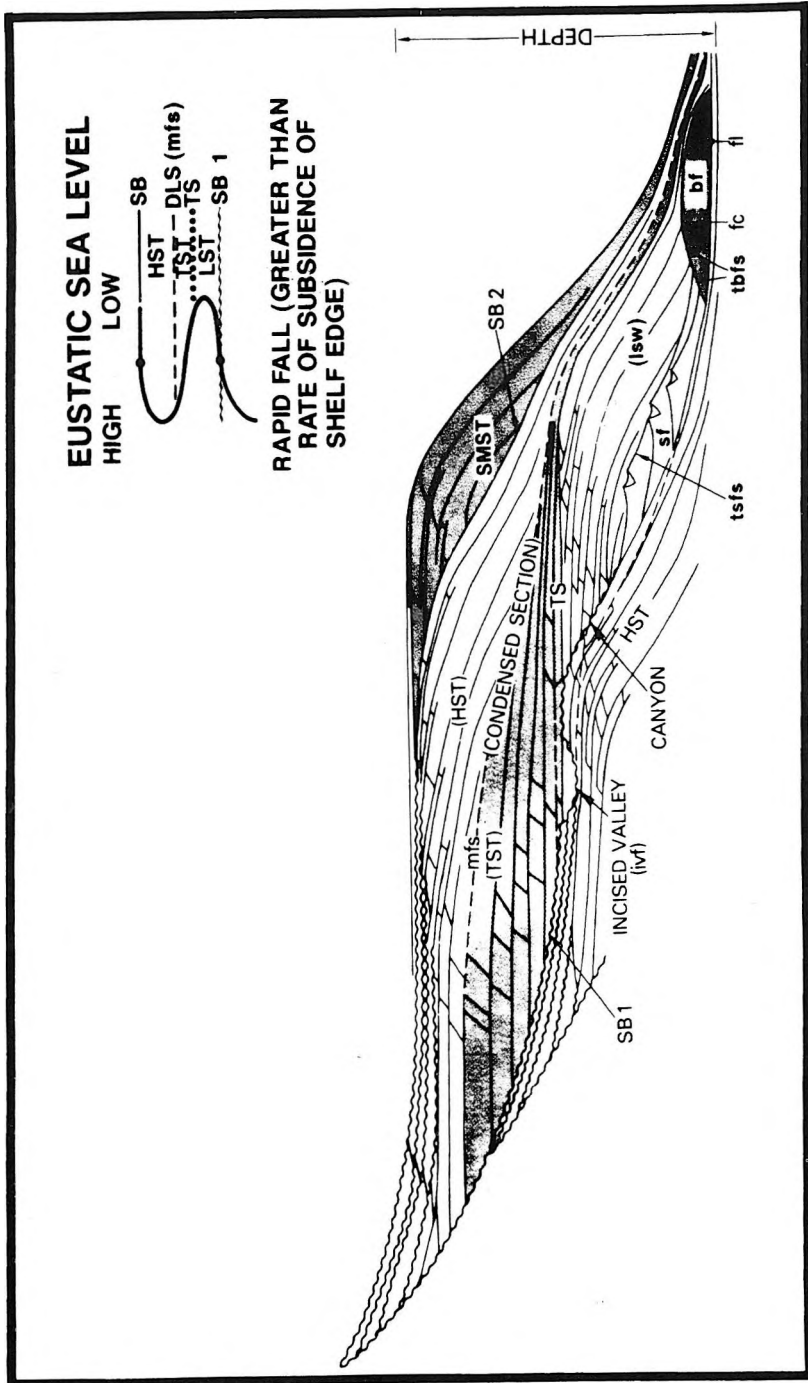
We compiled composite regional seismic sections, compressed in length, in order to see the Neogene depositional infill-history, i.e. how the sequences follow each other on a regional scale. The locations of these regional sections can be seen in *Fig. 3*. The sequence boundaries (see regional sections, *Figs. 4, 5, 6*) were identified on the basis of reflection terminations. The systems tracts were identified on the basis of seismic configuration and well log curve pattern.

Since we do not have enough reliable absolute age data in the Transdanubian region, we marked the sequence boundaries with numbers and also with their assumed ages in MA: I(15.5), II(13.8), III(12.5) (these are synrift), IV(10.5), V(8.2) and VI(6.3 MA) (these are postrift sequences).

We mainly concentrated on the postrift sequences. The line of the offlap break-points of IV(10.5), V(8.2) and VI(6.3) sequence boundaries, also called shelf margin, are indicated on the map (*Fig. 3*).

#### 5. Middle-Miocene sequences

The I(15.5), II(13.8), III(12.5) sequence boundaries (*Fig. 7*) belong to the synrift period of the basin evolution. These sequences were divided into systems tracts mainly on the basis of well logs (*Fig. 8*). The LST can be characterized by high resistivity, the TST by the tendency of upward decreasing resistivity, the maximum flooding surface by the most clayey stratum, and the HST by its tendency of upward increasing resistivity.



Vail, 1987

Fig. 1. Sequence stratigraphy diagrammatic section, with sketched sea level changes [VAIL 1987]  
 1. ábra. Szekvencia sztratigráfiai diagram és egy elvi vízszintingadozási görbe [VAIL 1987]



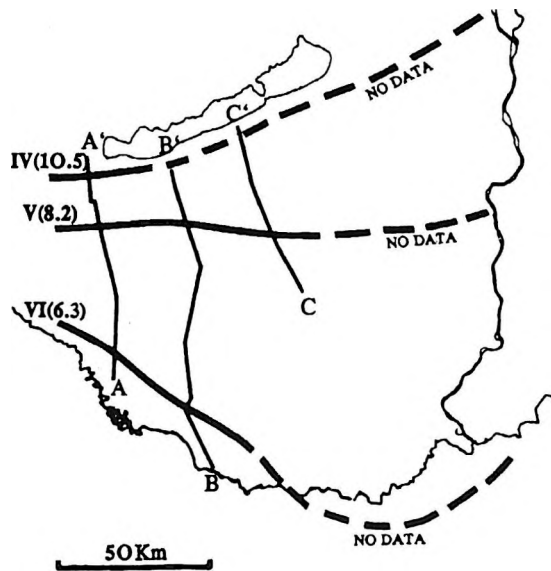


Fig. 3. Index map of South Transdanubia, showing the locations of regional seismic lines. The bold lines (e.g. 6.3) represent the lines of depositional shoreline break points with the assumed age of sequences [HAQ et al. 1987]

3. ábra. Dél-Dunántúl helyszínrajza, feltüntetve a regionális szeizmikus szelvények helyét. A vastag vonalak (pl. 6.3) a szekvenciák ellapolódási törés („offlap break-point”) helyét jelölik a feltételezett vízszintesési koral [HAQ et al. 1987]

## 6. Pannonian s.l. sequences

Three Pannonian s.l. sequence boundaries were identified: IV, V, VI, assumed to be due to 10.5, 8.2 and 6.3 MA sea-level falls (Fig. 4, 5, 6). The non-marine deposition is the result of prograding delta systems from the northern part of the basin. Because of the progradation from the basin margin to the deep basin, the older sequence on the basin margin deposited in a shallower environment, while the younger sequences reached the deeper parts of the basin.

The sequence between III(12.5) and IV(10.5) (Fig. 9) deposited in a shallow water environment, on a flat slope. In spite of this, erosional truncations are visible so the upper sequence boundary represents a significant erosion.

The sequence between IV(10.5) and V(8.2) boundaries (Fig. 10) deposited still in shallow but relatively deeper water, compared to the previous sequence. The shelf margin is very distinct, and the significant erosion is also generally typical of the V(8.2) sequence boundary. On the IV(10.5 MA) sequence boundary, at the bottom of this sequence there are onlap reflection terminations, which are assumed to represent turbidite sandstone pinch outs.

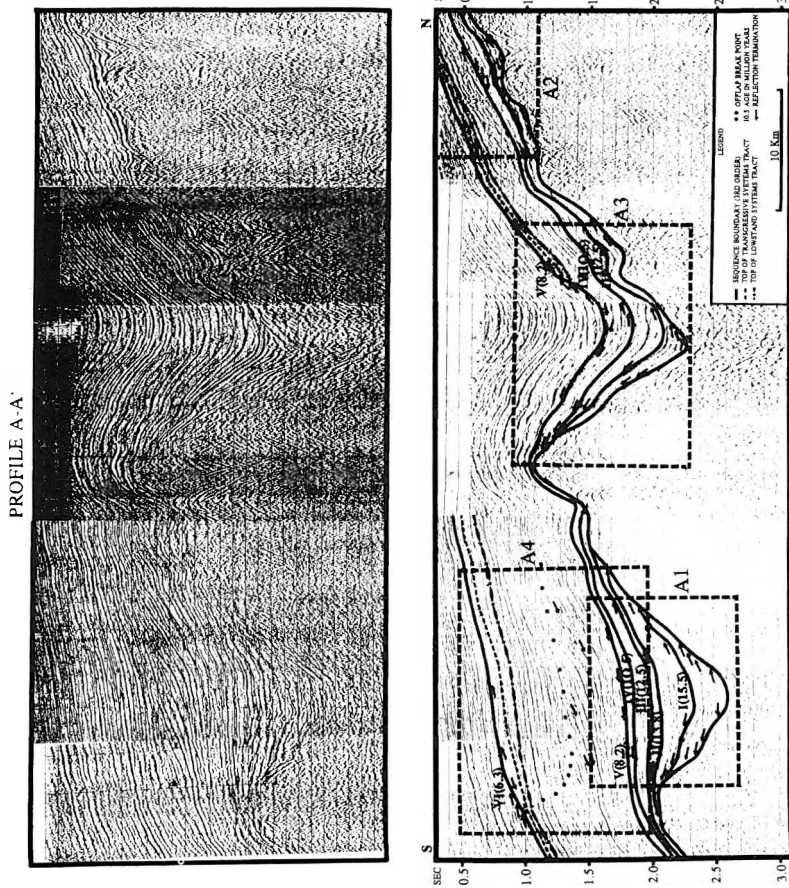


Fig. 4. A-A' regional seismic section and its interpretation: the third-order sequence boundaries, and the assumed ages of the sequence boundaries. The offlap break-points of the sequences are at the erosional truncations. This figure also shows that due to the morphology, during progradation deposition reached deeper and deeper part of the basin. After 6.3 MA depositional environment became shallow again because of the infilling of the basin

4. ábra. Az A-A' jelű regionális szeizmikus szelvény és értelmezése: a szekvenciahatárok a feltételezett korokkal. A szekvenciák ellapolódási törése az eróziós reflexióelvégződéseknél van. Az ábrán látható, hogy az üledékgyűjtő morfológiája miatt a progradáció során az üledéklerakódás a medence egyre mélyebb részére jutott. 6.3 MA után az üledéképződési környezet ismét sekély lett a medence feltöltődése miatt

## PROFILE B-B'

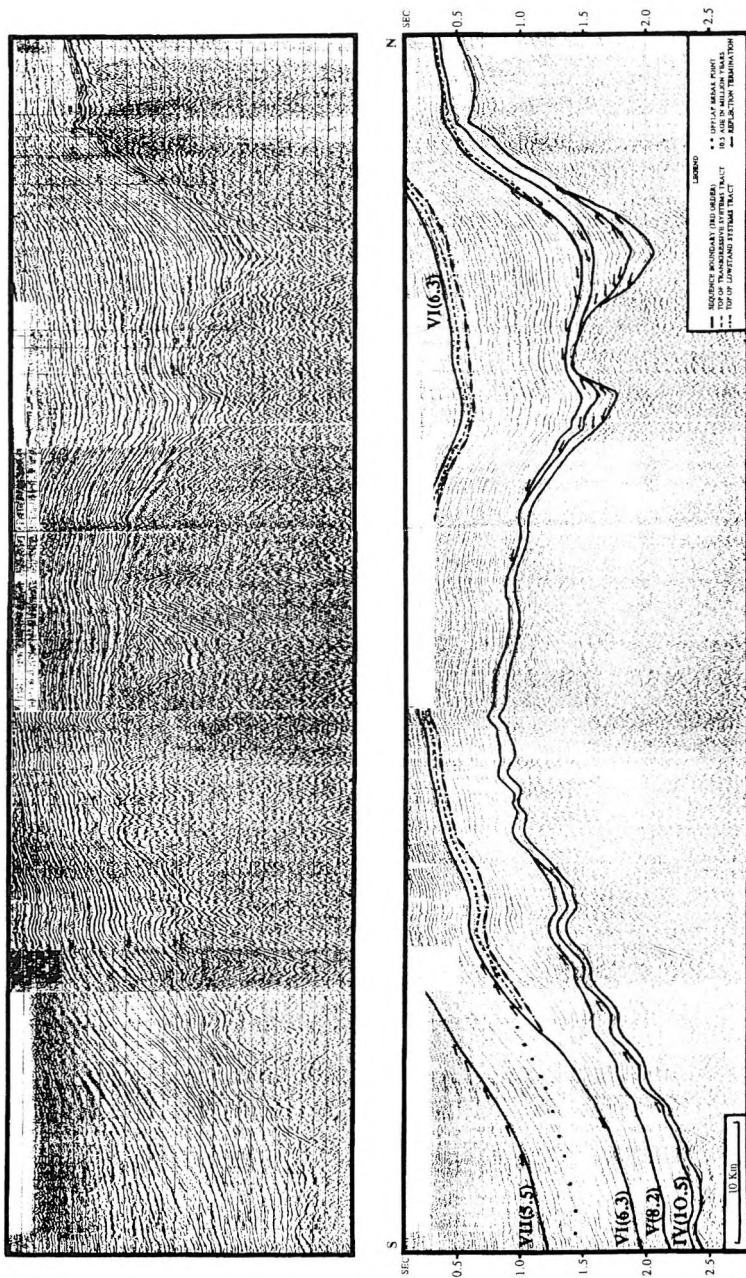


Fig. 5. B-B' regional section — thick lowstand prograding complex (LPW) in sequences V(8.2)-VI(6.3) and VI(6.3)-VII(5.5). The offlap break-points of the sequences are at the erosional truncations. Sequence boundary VII(5.5) can also be identified at the southern end of this section

5. ábra. A B-B' jelű regionális szelvény — vastag kisvízi progradáló öszlet (LPW) van az V(8.2)-VI(6.3) és a VI(6.3)-VII(5.5) szekvenciák között. A szekvenciák ellapolódási törése az eróziós reflexióelvégezéseknél van. A szelvény déli részén kijelölhető a VII(5.5) szekvenciahatár is

## PROFILE C-C'

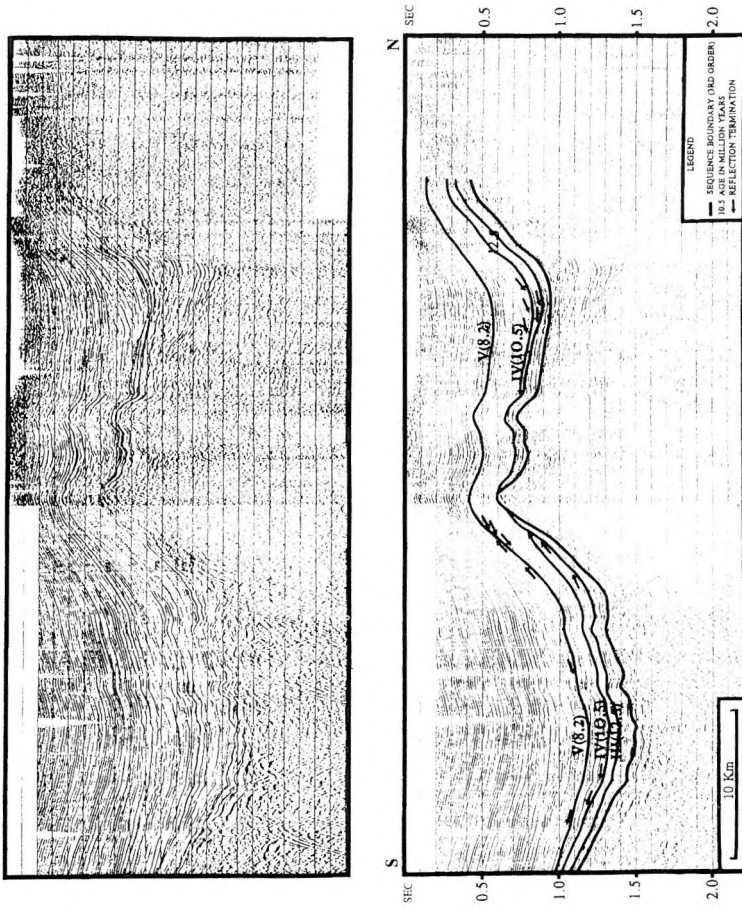


Fig. 6. C-C' regional section — shows the offlap-break-point of sequence V(8.2)–VI(6.3) at the erosional truncations. The lowstand prograding complex is relatively thick  
 6. ábra. A C-C' jelű regionális szelvény — látható az V(8.2)–VI(6.3) szekvencia ellapolódási törése az eróziós reflexióelvégződésnél. A kisvízi progradáció összetett itt is viszonylag vastag

## PROFILE A1

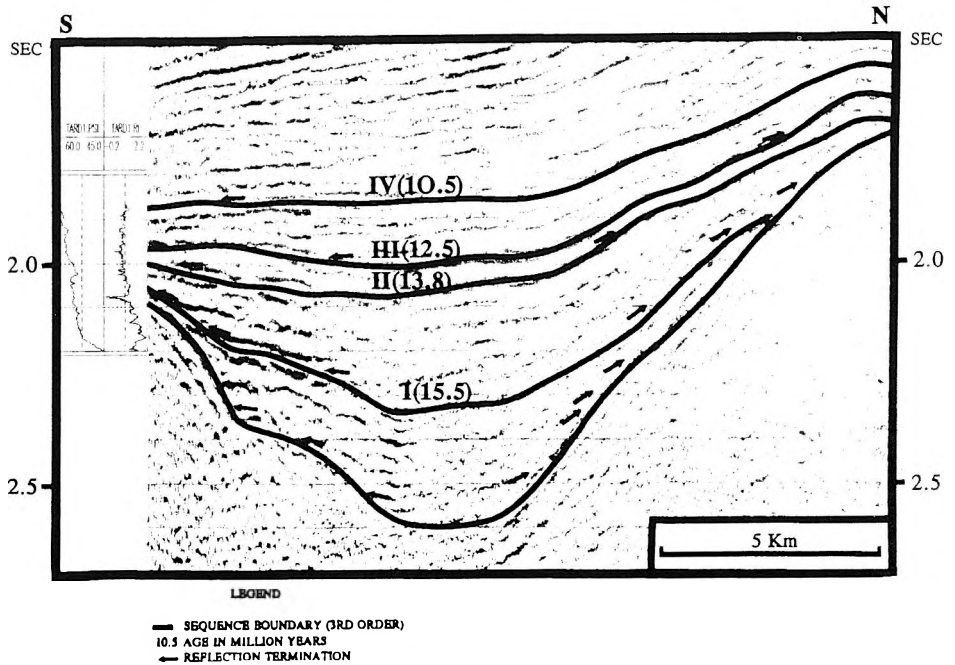
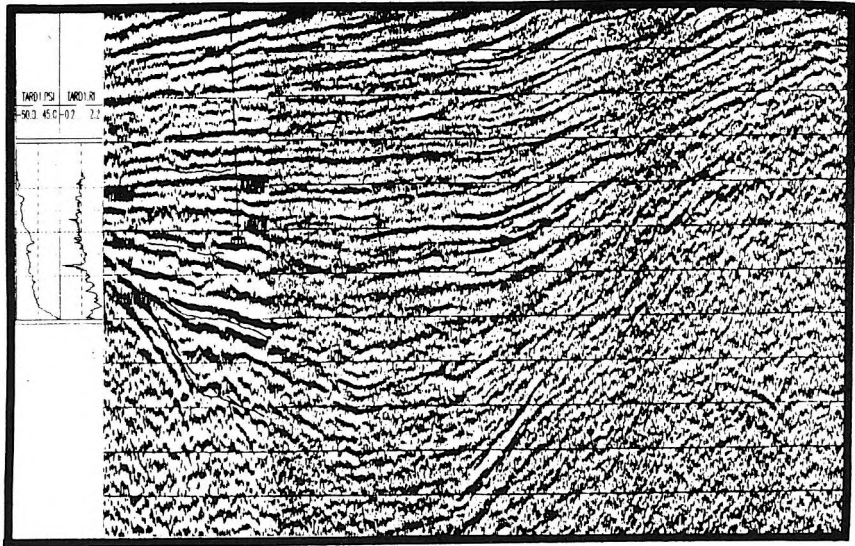


Fig. 7. Enlarged detail of Fig. 4., showing the synrift sequences. Interpretation is based on well-log (see Fig. 8)

7. ábra. Részlet a 4. ábrából, a medence képződéssel egyidejű szekvenciákról. Az értelmezés a karotázsgörbék alapján készült (ld. 8. ábra)

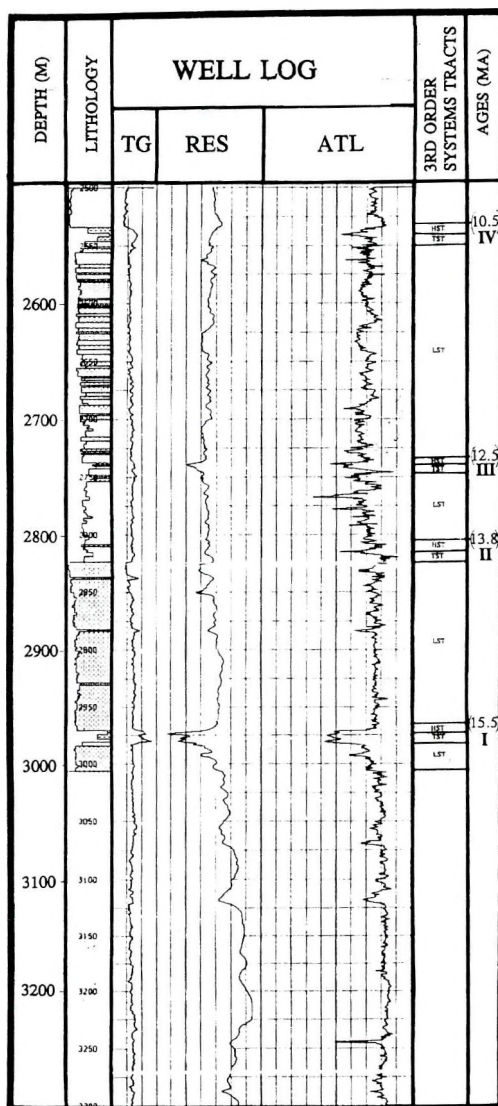
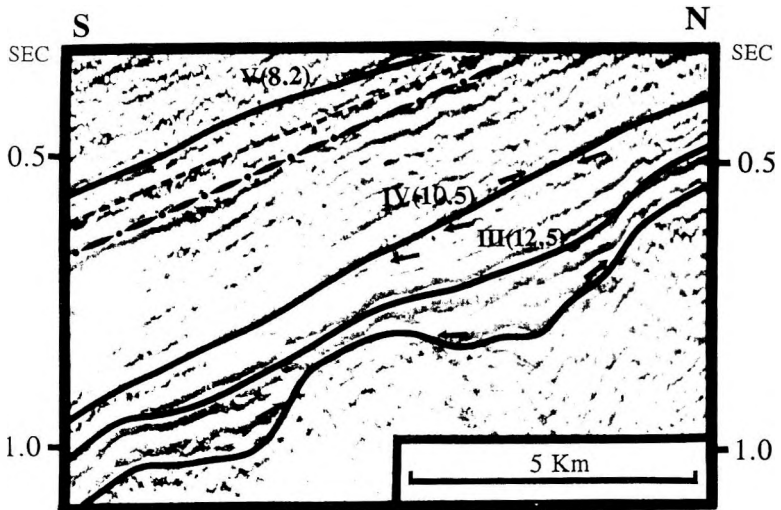
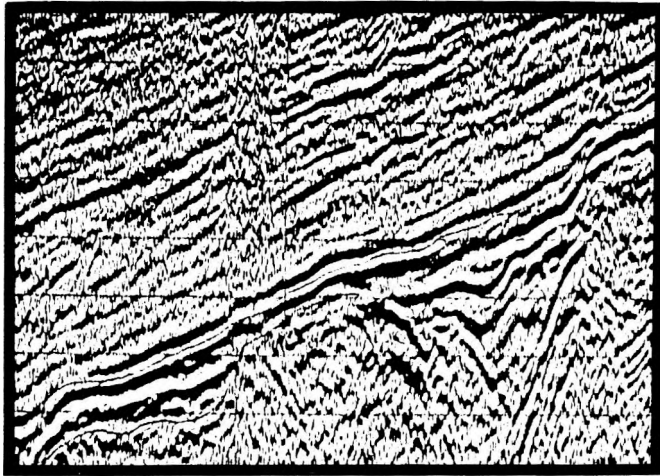


Fig. 8. Well-log sequence stratigraphic interpretation. The log pattern of LST is characterized by high resistivity and crescent shape, the log pattern of TST is an inverted Christmas tree shape, and that of HST is funnel shaped. Legend: LST— lowstand systems tract; TST— transgressive systems tract; HST—highstand systems tract; 10.5— Age of sequence boundary in million years [HAQ et al.1987]; IV— number of sequence boundary; TG—gamma ray; RES—resistivity; ATL—acoustic log

8. ábra. Karotázs szekvencia sztratigráfiai értelmezés. Az LST görbéje általában nagy ellenállással és kifli formával jellemzett, a TST felfele csökkenő kiterésű, „karácsonyfa” alakú görbe, a HST felfele durvuló „tölcsér” alakú görbe. LST— kisvízi rendszer egység; TST—transzgressziós rendszer egység; HST—magasvízi rendszeregység; 10.5—szekvenciahatár kora millió évben; IV— szekvenciahatár sorszáma; TG—termo gamma görbe; RES—ellenállás görbe;

## PROFILE A2



## LEGEND

- |         |                                    |      |                        |
|---------|------------------------------------|------|------------------------|
| —       | SEQUENCE BOUNDARY (3RD ORDER)      | .... | OFFLAP BREAK POINT     |
| - - -   | TOP OF TRANSGRESSIVE SYSTEMS TRACT | 10.5 | AGE IN MILLION YEARS   |
| - · - · | TOP OF LOWSTAND SYSTEMS TRACT      | ←    | REFLECTION TERMINATION |

*Fig. 9.* The sequence -IV(-10.5) prograded in relatively shallow water environment in a flat slope situation. The upper boundary of the sequence is characterized by very strong erosional truncation, although not very easily visible because of the flat slope

9. ábra. A -IV(-10.5) szekvencia viszonylag sekély vizi környezetben, lapos lejtőn rakódott le. A szekvencia felső határát nagy mértékű eróziós reflexióelvgződés jellemzi, bár ez a lapos lejtő helyzet miatt nem nagyon jól látható

## PROFILE A3

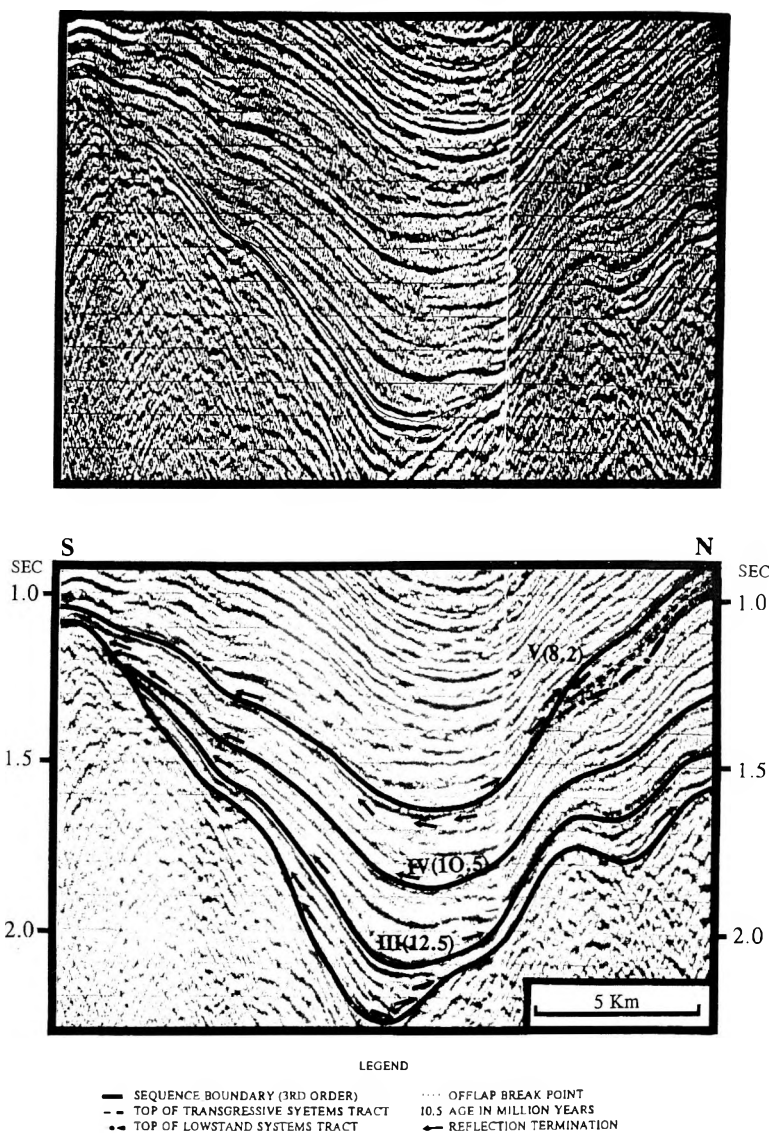


*Fig. 10.* The sequence of IV-V(10.5-8.2). The upper boundary is characterized by strong erosional truncation and spectacular shoreline break. The bottom boundary is characterized by onlap reflection terminations. Relatively thick lowstand prograding complex and thin transgressive and highstand systems tract are also characteristic

*10. ábra.* A IV-V(10.5-8.2) szekvencia felső határát erős reflexióelvégződés és látványos parti törés jellemzi. Az alsó szekvenciahatárt rálapolódó reflexióelvégződések jellemzik. A kisvízi rendszer-egység (LST) viszonylag vastag, a transzgressziós rendszer-egység (TST) és a magassvízi rendszer-egység (HST) viszonylag vékonyak

The sequence between V(8.2) and VI(6.3) boundaries (*Fig. 11*) deposited in relatively deeper water. Inside this third-order sequence, fourth-order sequences can be recognized (marked with arrows), which could also be divided into systems tracts. These fourth-order sequences can be considered the LST of the third order sequence — specifically lowstand prograding wedge (LPW). The offlap break-points of the prograding wedge are marked in the figure, the progradation is spectacular. The progradation goes into aggradation when the relative water-level rises. The distinct shelf margin belongs to the VI(6.3) sequence boundary. The oblique reflections of the prograding HST are marked in the figure. Since the HST prograded in a shallow water environment, the oblique reflections are relatively flat.

The next sequence built out with onlap reflection terminations above the VI(6.3 MA) sequence boundary. At a later period of basin fill, on the main part of the studied area, there was no LST above this sequence boundary, only alternating transgressive/highstand systems tracts (TST/HST). There is LST above VI(6.3) sequence boundary only in the southern part of the studied area (*Fig. 5*).

## 7. Discussion

The geometry of the interpreted sequences shows the same characteristics as VAIL's third-order sequences [1987]. According to the VAIL model, the sequence boundaries are due to sea level falls. POGÁCSÁS et al. [1988] correlated hiatuses with the global sea level curve of HAQ et al. [1987], suggesting that the water level of the Pannonian Lake fluctuated in the same phase as did the global sea level. Accepting the results of POGÁCSÁS et al. [1988] based on correlation of magnetostratigraphic data, the age of the interpreted third-order sequences correlates with the global sea level curve of HAQ et al. [1987] (*Fig 2.*), so the sequence boundaries could be dated with magnetostratigraphic data taken into consideration (*Fig. 12*). The geometry and stratal pattern of the sequences and systems tracts show the same characteristics in the Transdanubian region and in the Great Plain. Assuming the same sequence boundary ages, *Fig. 13* shows the sequence stratigraphic model of the Pannonian Basin. Since the sequence boundaries are due to sea level falls, in the case of the Pannonian Basin they are due to lake-level falls. According to the magnetostratigraphic correlations of POGÁCSÁS et al. [1988], the water level of the Pannonian Lake and its fluctuation were most probably related to the global sea level changes. The reason for this is not clear: it might be proto-Danube, climatic changes or permanent sea-links through long straits [TARI et al. 1992].

## PROFILE A4

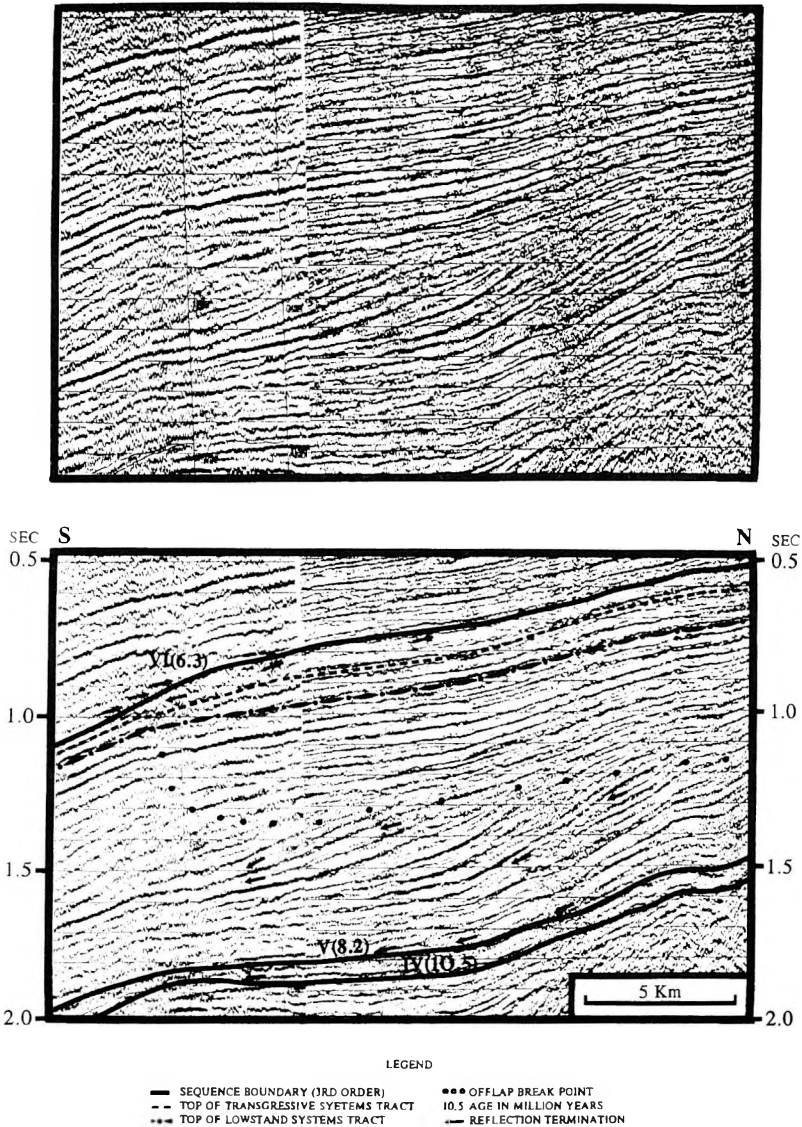


*Fig. 11.* The sequence of V-VI (8.2-6.3) is characterized by extremely thick lowstand prograding complex. The internal geometry changes from progradation into aggradation at the later period. The figure also shows the progradation of HST. After sequence boundary VI(6.3) due to the infill of the basin, the depositional environment became shallower, there are only neritic facies

*11. ábra.* A V-VI (8.2-6.3) szekvenciát különösen vastag kisvízi kiépülő összetet (LPW) jellemzi. A kiépülés felfelé épülésbe megy át. Az ábrán látszik a magasvízi rendszeregység (HST) kiépülése is. A VI (6.3) szekvenciahatár után a feltöltődés miatt az üledékfelhalmozódási környezet sekélyebb, nincs medencefácies, csak neritikus fáciések

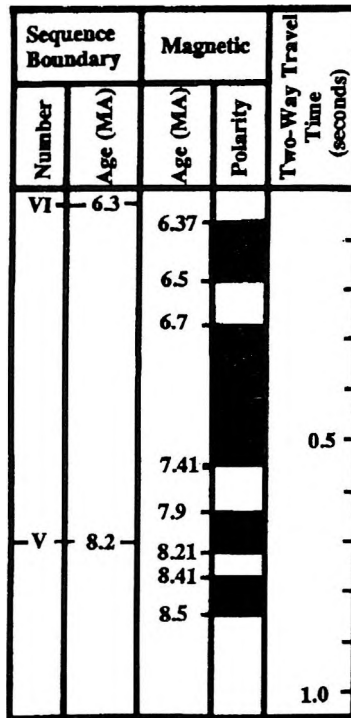


Fig. 12. Correlated seismic sequence boundaries and magnetic polarity zones of borehole Iharosberény-I, in two way travel time. V—Number of sequence boundary [HAQ et al.1987]; 8.2— Age of sequence boundary [HAQ et al.1987]; 8.41— magnetic age

12. ábra. Az Iharosberény-I fúrás mágneses polaritás zónái és a korrelált szeizmikus szekvenciahatárok szeizmikus idő léptékben. V— a szekvenciahatár sorszám; 8.2— a szekvenciahatár kora [HAQ et al. 1987]; 8.41— mágneses koradat

## 8. Conclusion

1. The sequences can be divided into systems tracts (LST, TST, HST) with the integrated interpretation of seismic sections and well logs.
2. The common characteristics of the described sequences are the thick lowstand prograding complex and relatively thin transgressive and high-stand deposits.
3. From our investigations it is probable also in the South Transdanubian region that the water level of the Pannonian Lake reflected the global sea level changes.
4. The interpreted sequences show the same geometry and stratal pattern as VAIL's [1987] third-order marine sequences.

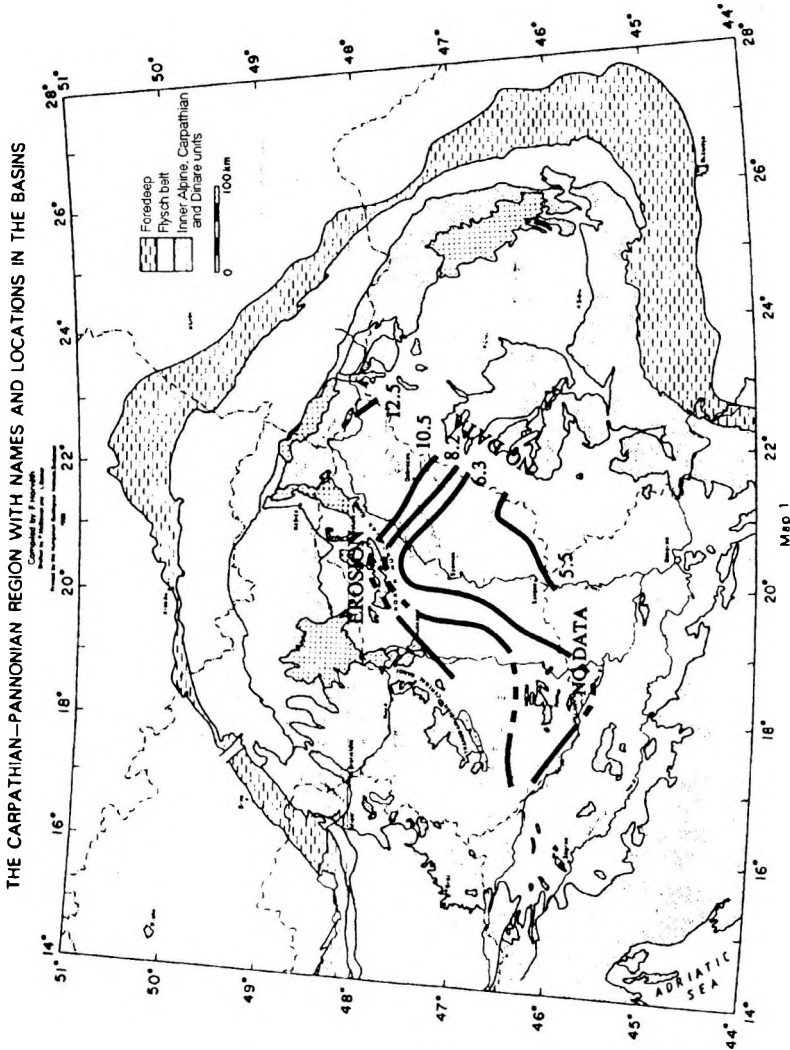


Fig. 13. Postrift infill of the Pannonian Basin involved the advance of deltas from the northern basin margin. The bold lines (e.g. 6.3) represent the lines of offlap break points with the assumed ages of the HQ et al. [1987] curve

13. ábra. A Pannon medence feltöltődése az északi medenceperem felől kiépülő deltarendszer eredménye. A vastag vonalak (pl. 6.3) a szekvenciák elapolódási törésének vonalát jelzik, a feltételezett vízintézési korokkal a HQ et al. [1987] görbe alapján.

## Acknowledgement

The authors are grateful to the leaders of MOL Rt. GKE — especially to MOLNÁR Károly — for permission to publish this paper.

## REFERENCES

- BALLY A. W., SNELSON S. 1980: Realms of subsidence. *In*: A. D. MIALI (ed.), Facts and principles of world petroleum occurrence. *Can. Soc. Petrol. Geol. Mem.* **6**, pp. 9-94
- BERKES Z., POGÁCSÁS Gy., SZANYI B. 1983: Seismic stratigraphic interpretation of the Neogene sediments in the Derecske depression of Eastern Hungary. *Proceedings of 28th International Geophysical Symposium, Balatonszemes* pp. 158-172
- CSONTOS L., NAGYMAROSY A., KOVAČ M., HORVÁTH F. 1992: Tertiary evolution of the intra-Carpathian area: a model. *Tectonophysics*, **208**, pp. 221-241
- HAQ B. U., HARDENBOL J., VAIL P. R. 1987: Chronology of fluctuating sea levels since the Triassic (250 million years ago to present). *Science*, **235**, pp. 1156-1167
- HORVÁTH F., BERCKHEMER H., STEGENA L. 1981: Models of Mediterranean back-arc basin formation. *Philos. Trans. R. Soc. London Ser. A*, **300**, pp. 383-402
- HORVÁTH F., DÖVÉNYI P., SZALAY Á., ROYDEN L. H. 1988: Subsidence, thermal and maturation history of the Great Hungarian Plain. *AAPG Mem.*, **45**, pp. 355-372
- KÁZMÉR M. 1984: The Bakony Mountains' horizontal movement in Paleogene. (in Hungarian) *Ált. Földt. Szemle*, **20**, pp. 53-101
- KÉSMÁRKY I., POGÁCSÁS Gy., SZANYI B. 1981: Seismic stratigraphic interpretation in Neogene Quaternary depressions of Eastern Hungary. *Proceedings of 26th International Geophysical Symposium, Leipzig*. pp. 130-140
- LANTOS M., HÁMOR T., POGÁCSÁS Gy. 1990: Magnetostratigraphic and seismostratigraphic correlations of Late Miocene and Pliocene (Pannonian s.l.) deposits of Hungary. IX. Congress R.C.M.N.S. (Barcelona, November 19-24, 1990) *Global Events and Neogene Evolution of the Mediterranean*. Abs. pp. 205-206
- MATTICK R. E., PHILLIPS R. L., RUMPLER J. 1988: Seismic stratigraphy and depositional framework of sedimentary rocks in the Pannonian Basin in Southeastern Hungary. *AAPG Mem.* **45**, pp. 117-146
- POGÁCSÁS Gy. 1984: Results of seismic stratigraphy in Hungary. *Acta Geol. Hung.* **27**, pp. 91-108
- POGÁCSÁS Gy., LAKATOS L., RÉVÉSZ I., UJSZÁSZI K., VAKARCS G., VÁRKONYI L., VÁRNAI P. 1988: Seismic facies, electro facies and Neogene sequence chronology of the Pannonian Basin. *Acta Geol. Hung.*, **31**, pp. 175-207
- POGÁCSÁS Gy., SEIFERT P. 1991: Vergleich der neogenen Meeresspiegelschwankungen im Wiener und im Pannonischen Becken. *Jubiläumsschrift 20 Jahre Geologische Zusammenarbeit Österreich — Ungarn*, pp. 93-100
- TARI G., HORVÁTH F., RUMPLER J. 1992: Styles of extension in the Pannonian Basin. *Tectonophysics*, **208**, pp. 203-219
- TARI G., BÁLDI T., BÁLDI-BEKE M.: Paleogene retroarc flexural basin beneath the Neogene Pannonian basin: a geodynamic model. *Tectonophysics*, in press
- VAIL P. R. 1987: Seismic stratigraphy interpretation procedure. *AAPG Studies in Geology* #27 Vol. 1. pp. 1-10
- VAIL P. R., AUDEMARD F., BOWMAN S. A., EISNER P. N., PEREZ-CRUZ C. 1991: The Stratigraphic Signatures of Tectonics, Eustasy and Sedimentation — an Overview. *In*: *Cycles and Events in Stratigraphy*. Springer-Verlag, Berlin pp. 617-659

- VAKARCS G., VÁRNAI P. 1991: The seismostratigraphic model of the Derecske trough area. (In Hungarian with English abstract.) *Magyar Geofizika* 32, pp. 38–50
- VAKARCS G., VAIL P. R., TARI G., POGÁCSÁS Gy., MATTICK R. E., SZABÓ A., BOWMAN S.: Third-order Miocene-Pliocene depositional sequences in the prograding delta complex of the Pannonian Basin. *Tectonophysics*, in press
- VAN WAGONER J. C., MITCHUM R. M., POSAMENTIER H.W., VAIL P. R. 1987: Key definitions of sequence stratigraphy. *AAPG Studies in Geology* #27 Vol. 1, pp. 11–15

## SZEKVENCIASZTRATIGRÁFIAI VIZSGÁLATOK A DÉL-DUNÁNTÚLON

UJSZÁSZI Katalain és VAKARCS Gábor

Magyarország dél-dunántúli területének szeizmikus szekvencia sztratigráfiai értelmezésével foglalkozunk, bemutatjuk ennek a területnek az első szekvencia sztratigráfiai modelljét.

Vizsgálatunk során a középső-miocén — pannon s.l. rétegsorral foglalkoztunk. A középső-miocén végétől a Pannon medence izolált volt a világtengertől. Az ekkor lerakódott nemtengeri rétegsor is üledékes szekvenciákra bontható. Értelmezésünk során három színrift és három posztrift harmadrendű szekvenciát mutattunk ki.

A szekvenciákat felépítő rendszer-egységek szeizmikus reflexiós képének és üledékes fáciesének elemzése alapján a Pannon medence lakusztikus szekvenciái jó egyezést mutatnak a tengeri törmeléken üledékes szekvenciák jellemzőivel. Ezek a lakusztikus szekvenciák feltehetőleg a Pannon beltő jelentős vízszinteséseivel függnek össze, és harmadrendű szekvenciáknak értelmezzük őket. A Pannon-tó vízszintje és változásai feltehetően összefüggésben voltak a világtengerrel.



## REFLECTION SEISMIC SURVEYS FOR OIL AND GAS EXPLORATION IN NORTH-EAST GERMANY

H. GAERTNER<sup>\*</sup>, K. H. FEBER (†), W. KÜSTERMANN<sup>\*</sup>, S. PRÖHL<sup>\*</sup>,  
H. WOLFF<sup>\*</sup>, K. WRUCK<sup>\*\*</sup>

The paper gives an overview on the reflection seismic surveys executed by Geophysik GmbH in north-east Germany within the last few years. The main exploration targets were the Zechstein and Rotliegendes formations. The usually very complex seismogeological conditions required special techniques for data acquisition as well as processing and interpretation, which were adjusted to the given exploration target. Rotliegendes exploration was done at the marginal zone of the basin by tracing the reflection of the Zechstein base with 2-D and 3-D surveys. It was possible to detect and trace reflections from the Rotliegendes itself in spite of the poor petrophysical differentiation, great depth, and intensive level of multiple waves. Under certain conditions a seismostratigraphic interpretation was possible here as well. In Zechstein exploration some specially developed high-resolution seismic methods were used. In comparison with conventional seismic surveys their application brought about a much more detailed image of the structure. Furthermore, based on a wave-picture analysis it became possible to obtain information on the facial character of the Zechstein and to detect areas of increased porosity.

**Keywords:** reflection, seismic surveys, Germany, oil and gas fields

### 1. Exploration targets

Geophysik GmbH started reflection seismic surveys to investigate the deeper underground of north-east Germany in the early fifties. The transition from analog to digital recording in 1968 and the simultaneous introduction of the CDP method yielded a remarkable increase in data quality and information content. But this was not sufficient to solve the complex geological problems in that region. In addition, a great deal of research work was necessary to improve and adapt the field, processing and interpretation methods.

\* Geophysik GGD mbH, Bautzner Str. 67, 04347 Leipzig

\*\* formerly Geophysik GmbH, now with Erdöl-Erdgas GmbH, 39245 Gommern

In the early sixties the main targets of oil and gas exploration were formations of the Zechstein and Rotliegendes since the Mesozoic formations had proved devoid of hydrocarbons. The Zechstein barrier of the basin margin, being of greatest interest was, for years, intensively surveyed on a very dense line grid.

The seismic measurements over the basin margin of the Rotliegendes also began in the sixties and led to a significant gas discovery in 1968 near Peckensen-Salzwedel, subsequently it led to the development of a major deposit. The actual target of investigations was the reflective horizon  $Z_1$  (see e. g. Fig. 2) at the boundary between the salt of the Leine series and the anhydrite of the Stassfurt series; this horizon proved to be a reliable indicator of both the surface and the structure of the Rotliegendes sediments.

In the inner parts of the basin, which had previously not been considered promising, a lot of seismic reconnaissance lines were shot in the mid-seventies and later. Despite very unfavourable seismo-geological conditions, an overview of the regional structure, thickness relations, fault grid and facies interlocking could be obtained.

The layout of all digitally surveyed seismic lines is shown in *Fig. 1*.

## 2. Development of field methods for digital seismic surveys

Since the introduction in 1968 of digital data acquisition, the field technique has continuously been improved — taking into account the growing complexity of the geological setting. The field parameters applied in this period are listed in *Table 1*. The main trends have been the increasing coverage and receiver intervals and, at the beginning, also the increase of charge as well as that of the proportion of pattern shooting, the latter of which was later reduced again. In the years 1988–90 the four seismic parties involved in the work achieved an annual productivity of 3000 line kilometres. One of these parties was equipped with vibrators and a 240-channel telemetry system, the other three were equipped with two 96-channel standard systems of our own design for simultaneous shot-generated recording.

Parameters	Pre-Zechstein exploration	Exploration of the Rotliegendes surface	Zechstein exploration
CDP-coverage	48-96	24-48	12-24
Geophone group interval [m]	40-50	40-50	50
$X_{max}$ [m]	3800-4700	1900-2450	2375
Shot-point interval [m]	40-50	40-50	50-100
Energy generation			
● Explosives			
- Charge group x weight [kg]	1 × 5	1-3 × 5	1-5, sometimes 3 × 2-3
- Base [m]	-	0-30	20-30
- Depth of charge below weathering layer [m]	10-15	10-15	10-15
● Airguns	-		
- Number of sources		4	
- Base [m]		28	
- Vertical stack		16-24 fold	
● Vibroseis			
- Number of sources	4	4	
- Base [m]	45	45	
- Vertical stack	18 fold	20 fold	
- Sweep frequency	12-64	14-88	
Number of geophones per group	12-24	24	12
Grouping area (x · y [m <sup>2</sup> ]) 33x	44-66 × 0-10, 33 × 0	40-55 × 10, 24 × 0 (sometimes 40 × 24)	44 × 0-10, 33 × 0
Geophone type (Natural frequency [Hz])	10/15	10/15	10/15
Station			
● Channels	96-200	48-192	48-96
● Type	SD16, SN328	SD12, SD16, SN328	SD12, SD16
Special surface		3D	high-resolution seismics

Table 1. Field parameters of conventional seismic survey  
 I. táblázat. A hagyományos szeizmikus kutatás terepi paraméterei

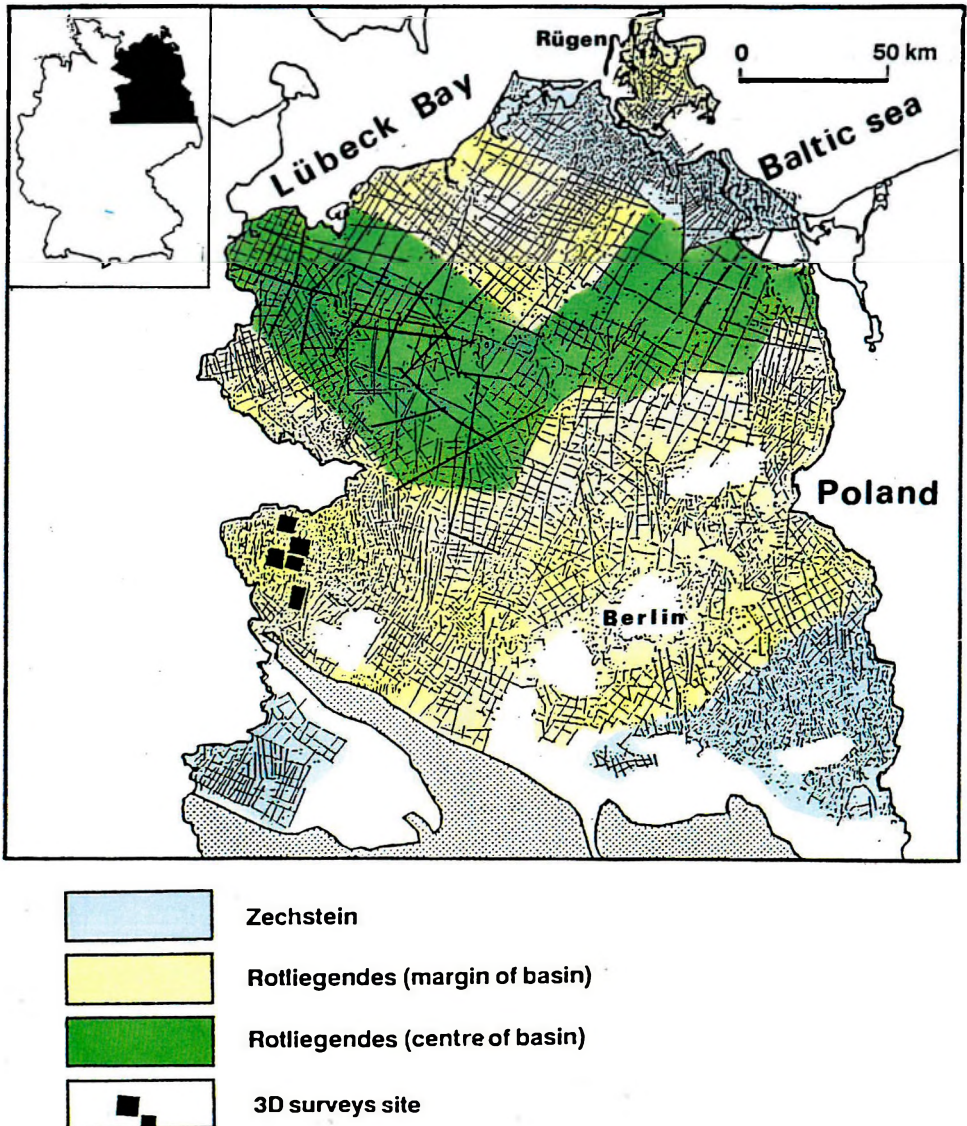


Fig. 1. Line location map of digital seismic surveys in North-East Germany  
 1. ábra. Északkelet-Németország digitális szeizmikus kutatásainak szelvényhálózata

In order to investigate the Zechstein a procedure package for high-resolution seismic surveys was developed [GAERTNER, SCHEIBE, 1987 and 1991], the main feature of which is the use of 60 Hz geophones (see *Table II*).

Geophones	L-40 A-1 (60 Hz)
Geophone grouping	6 fold (10 m base)
Sample rate	2 ms
Geophone group interval $x$	$0.5 \cdot x^{1)}$
Observation length $X_{\max}$	$(0.5 \dots 0.7) \cdot X_{\max}^{1)}$
Coverage CMP	$2 \cdot \text{CMP}^{1)}$
Charge depth $h$	$h^{1)} - (8 \dots 12) \text{ m}$
Charge weight $Q$	$(0.1 \dots 0.3) \cdot Q^{1)}$
<sup>1)</sup> Corresponding size in conventional seismic Zechstein exploration	

*Table II.* Field parameters of high resolution seismic surveys for Zechstein exploration  
 II. táblázat. A zechstein kutatásában alkalmazott nagyfelbontású szeizmikus kutatások terepi paramétereit

The intention is, through the use of these receivers, to cancel intense low-frequency components of the seismic wave-field which may suppress the weak high-frequency components. The base of the geophone arrays is drastically reduced to restrict as much as possible the filter effect of this interference system on the high-frequency components. The variation of the remaining field parameters corresponds to the general trend in exploration seismics towards a more detailed and reliable assessment of the underground. The decrease of charge depths and the total renunciation of shot patterns resulted in practically no increase in costs even with the closer shotpoint intervals.

On selected reconnaissance lines of a total volume of 1700 km the recording times were prolonged to 12 s or 15 s [WRUCK et al. 1987]. A considerable proportion of pre-Zechstein lines was surveyed in the parallel profiling technique. This method is based on 2 parallel arranged lines at a distance of 500 to 1200 m. These lines are mutually used as shot or receiver point lines. Three CMP-lines are the result. In the vicinity of essential boreholes special areal surveys were executed which provided closer, more detailed information as well as a much higher multiplicity — of up to 240-fold [PILLING et al. 1984].

Since 1986 several 3D prospects have been surveyed (Fig. 1) including their processing and interpretation. The field measurements were executed with a cross-line pattern comprising 4-5 receiver lines and one intersecting shot-line per block with either shot or vibrator generation. The recording system was the telemetry station SN368.

### 3. Examples from the Rotliegendes exploration

#### *Rotliegendes exploration by tracing of the Rotliegendes surface (horizon $Z_1$ )*

At the basin margin this exploration was accomplished successfully with both 2-D and 3-D surveys.

Figures 2 and 3 show the result of the 2-D seismic contouring of a gas deposit in the range of a regional fault zone. The first processing in the seventies

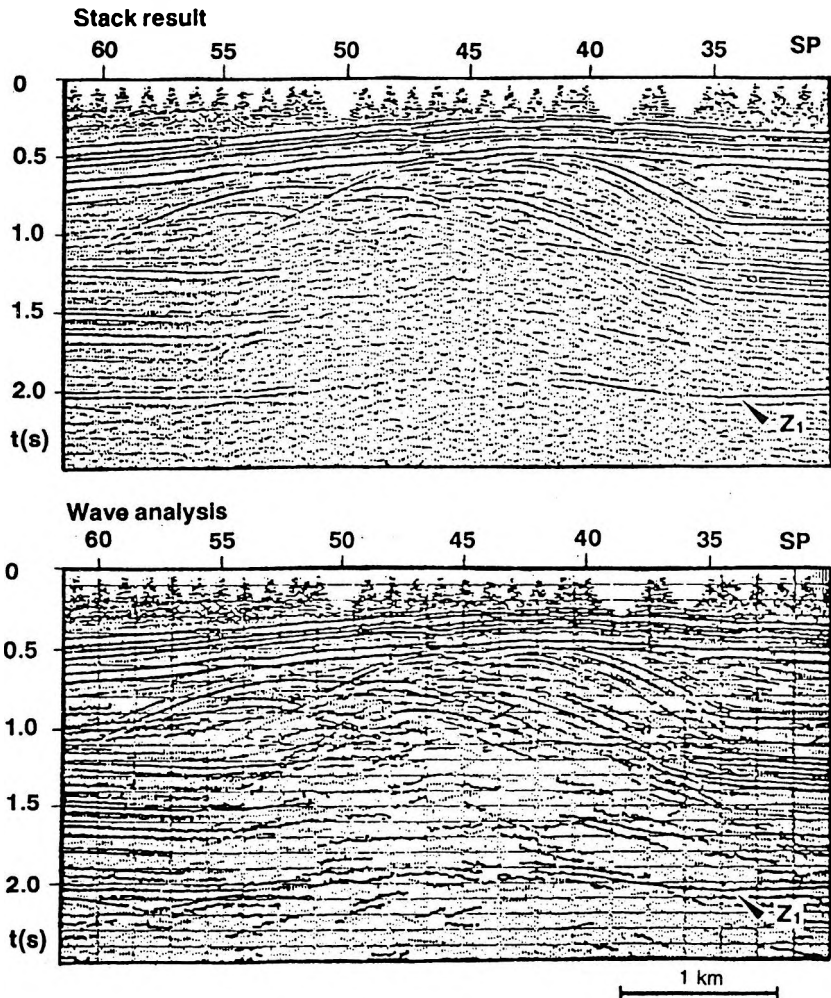


Fig. 2. Registration of the Rotliegendes surface (horizon  $Z_1$ ) under suprasaliniferous fault zone (time section)

2. ábra. A rotliegendes felszínének ( $Z_1$ ) észlelése a nagy sótartalmú vezetőzóna alatt (időszelvény)

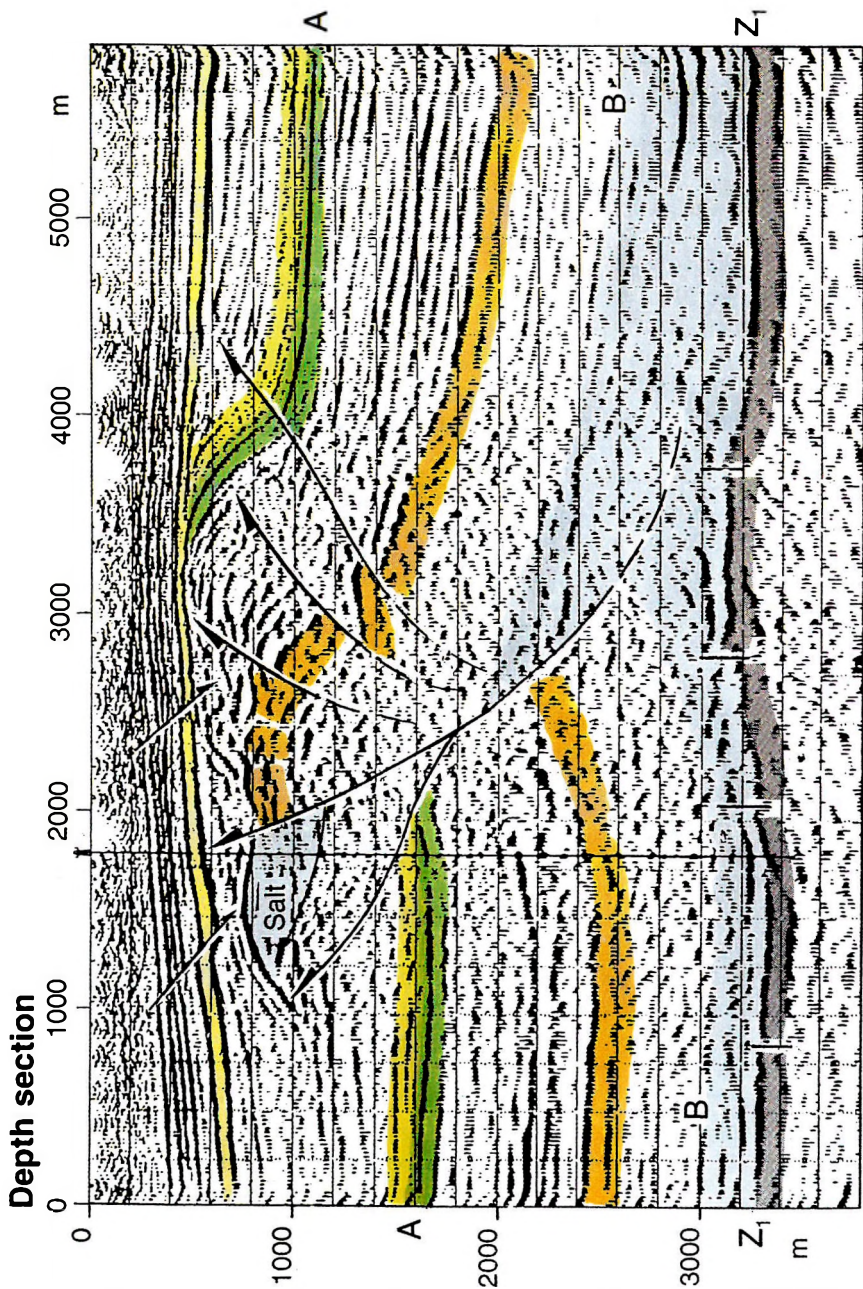


Fig. 3. Registration of the Rotliegendes surface (horizon  $Z_1$ ) under suprasaliniferous fault zone (depth section)

3. ábra. A rotliegendes felszínének ( $Z_1$ ) észlelése nagy sótartalmú vetőzóna alatt (mélységszelvény)

led to a 4 km broad gap in  $Z_1$ . By reprocessing with improved corrections it was possible to close this gap (Fig. 2, upper part). With the aid of a special process, the so-called wave analysis (Fig. 2, lower part) weak reflections were enhanced [see also BUDIG et al. 1977]. The presented result (Fig. 3) was obtained by finite difference time migration [SCHIKOWSKY 1984] providing a reliable reconstruction of dips up to  $50^\circ$  and also comprising time depth stretching. Compared with the previous interpretation result a much more detailed image of the faulted section can be seen. It seems that in the overburden a higher block was thrust from the right onto a lower block on the left, where the Zechstein salt served as a gliding track. A comparably small salt body, proved by drilling, is revealed by a remarkable caprock reflection at a depth of 800 to 1000 m as seen between shotpoints 50 and 55. The vertex faults extend up to the latest strata.

Exact static and dynamic corrections led — also in 3-D measurements — to optimal stacking results. 3-D migration carried out by successive 2-D migration of inlines and crosslines proved to be essential for the interpretation. Its application yielded improved reflection quality, the block boundaries appear more clearly, and the horizontal resolution is generally enhanced.

The strict definition of faults and the high information density allow a structural interpretation in such detail which cannot be obtained with 2-D measurements. The interpretation of the migrated 3-D data was interactively implemented with a COMSEIS workstation.

### *Detection of interfaces within the Rotliegendes*

Since the horizon  $Z_1$  is only usable for the exploration of the upper Rotliegendes at the basin margin, the necessity arises to detect and trace particular interfaces for the middle and lower Rotliegendes. The preconditions for that goal are unfavourable: weak and laterally varying petrophysical differentiation, the great depths and strong multiples from the overburden.

Each individual seismic line may produce a variety of plausible models. If ties to boreholes do not exist an acceptable evaluation of these models is difficult.

The above mentioned parallel profiling, as was employed in reconnaissance surveys of exposed regions, provided the basis for several interpretation procedures which yield even more reliable results.

In Fig. 4 (upper part) the result of wave analysis for a time section is presented. This section corresponds to a single line of a multiple profiling and does not allow an accurate assessment on the considered horizon, or on the faults and thickness conditions in the pre-Zechstein. Wave analysis results and the corresponding depth section (Fig. 4, middle part) may be interpreted differently. The lower part of Fig. 4 reveals that the summed section produced from 3 adjoining lines (500 m interval) provides a nearly unambiguous geological model. Based on this approach a regionally differentiated contribution to the structural interpretation of seismic data from the Rotliegendes could be achieved.

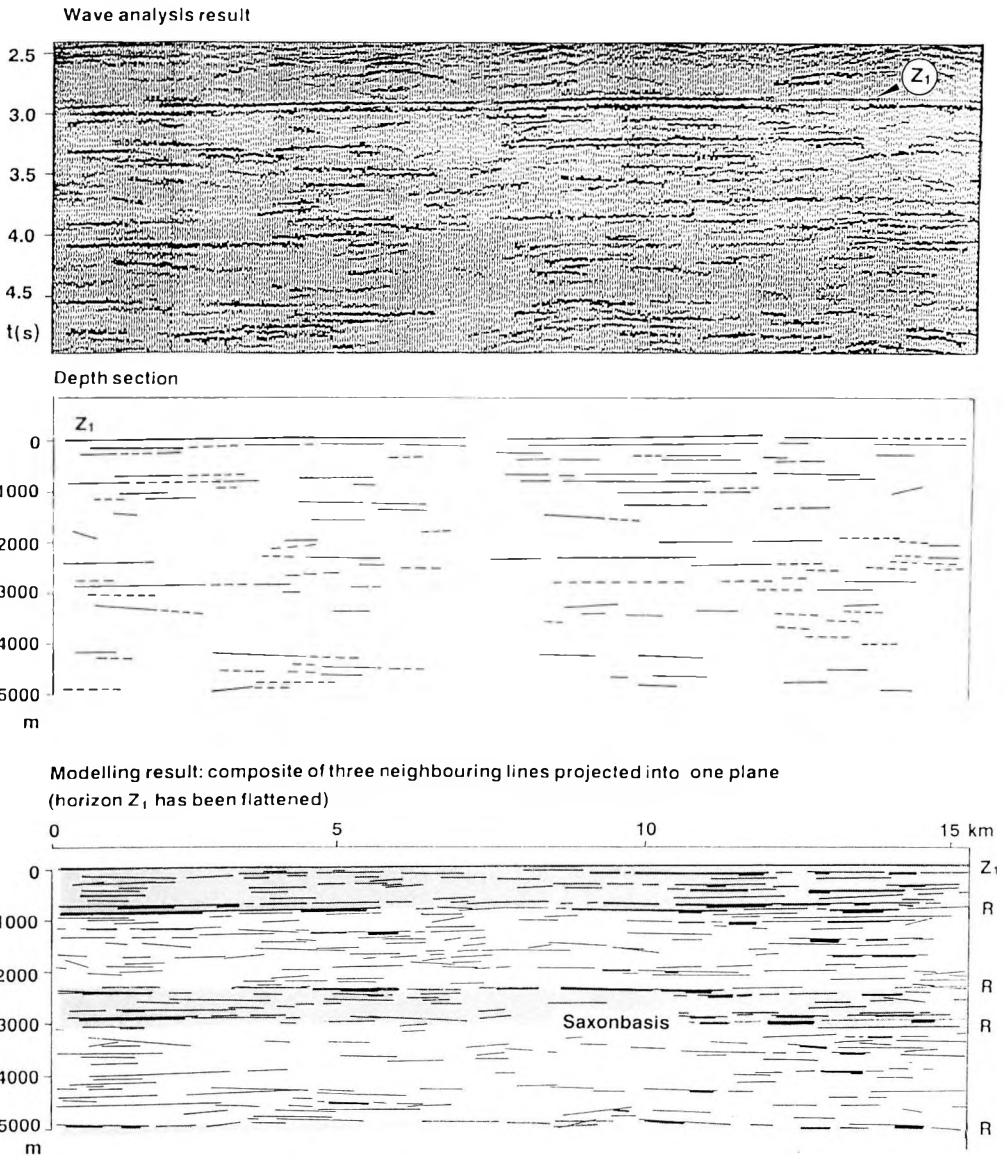


Fig. 4. Central line from the North-German-Polish basin — pre-Zechstein interpretation  
 4. ábra. Az északnémet-lengyel medence központi szelvénye — prezechstein értelmezés

### *Seismostratigraphic interpretation*

Besides structural interpretation of the Rotliegendes data we also tried to apply procedures of seismic stratigraphy for that exploration goal, despite the fact that the preconditions are very poor due to the insufficient S/N-ratio. The components of seismostratigraphic work are: the acquisition of all essential data from wells, the acquisition of additional information from time sections, and the integration of all obtained results to a geological model. This approach has been applied successfully in several regions.

The petrophysical parameters obtained from wells are the basis for the seismo-acoustic 1-D and 2-D modelling. For each well the geological and petrophysical input data, vertical seismic profiling and synthetic traces are compiled in a manner presented in *Fig. 5*. It can be shown by examples that with the interpretation of borehole data, modelling results, conventional seismic interpretation data, analysis of reflection character and of dynamic parameters it seems possible to achieve a seismostratigraphic subdivision of the Rotliegendes (*Fig. 6*). The highly simplified sequences presented in this figure, correspond to different lithological units.

## **4. Zechstein exploration with high-resolution seismic surveys**

### *Examples from areas with different surface conditions*

Until the introduction of high-resolution seismics the exploration of the lower Zechstein was based on the correlation of the key horizons  $X_2/X_3$  (upper and lower boundary of the Leine anhydrite),  $Z_1$  (upper boundary of Stassfurt anhydrite) and  $Z_3$  (lower boundary of Werra anhydrite). The higher resolution was required in order to better resolve the occurring interference intervals of these reflections ( $Z_1$  and  $Z_3$  in the foreland barrier,  $X_2/X_3$  and  $Z_1$  on the platform), and to record possible reflections from the reservoir rock (Stassfurt carbonate). With reservoir thicknesses between 40 and 80 m, the resolving power had to be improved by 1.5 to 2 against the conventional seismic results (see *Fig. 7*).

The first HR-seismic measurements carried out were experimental, but under favourable surface conditions in the range of the northern margin of the Zechstein basin. *Fig. 8* reveals that the required enhancement of the resolving power and a sufficient S/N-ratio could be achieved. The charge weights on this line were 0.3 kg.

At the southern margin of the Zechstein basin the surface conditions were less favourable. For that reason we applied a greater degree of coverage and we increased the charge weights to 1 kg. The results under simple surface conditions were excellent (*Fig. 9*). However, moraine covered areas, with

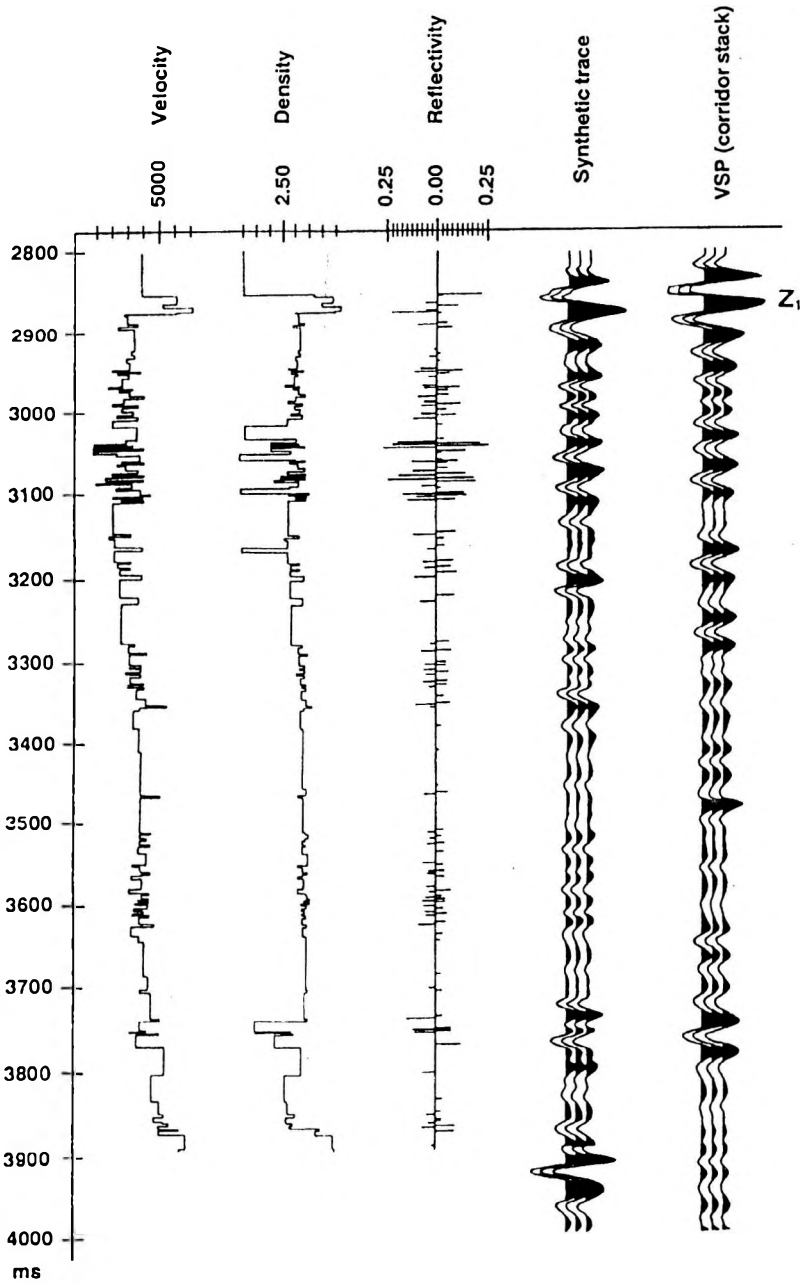


Fig. 5. Seismic modelling and corridor stack after VSP for a pre-Zechstein well  
 5. ábra. Szeizmikus modellezés és „corridor”-összegzés VSP után egy prezechstein fúrásban

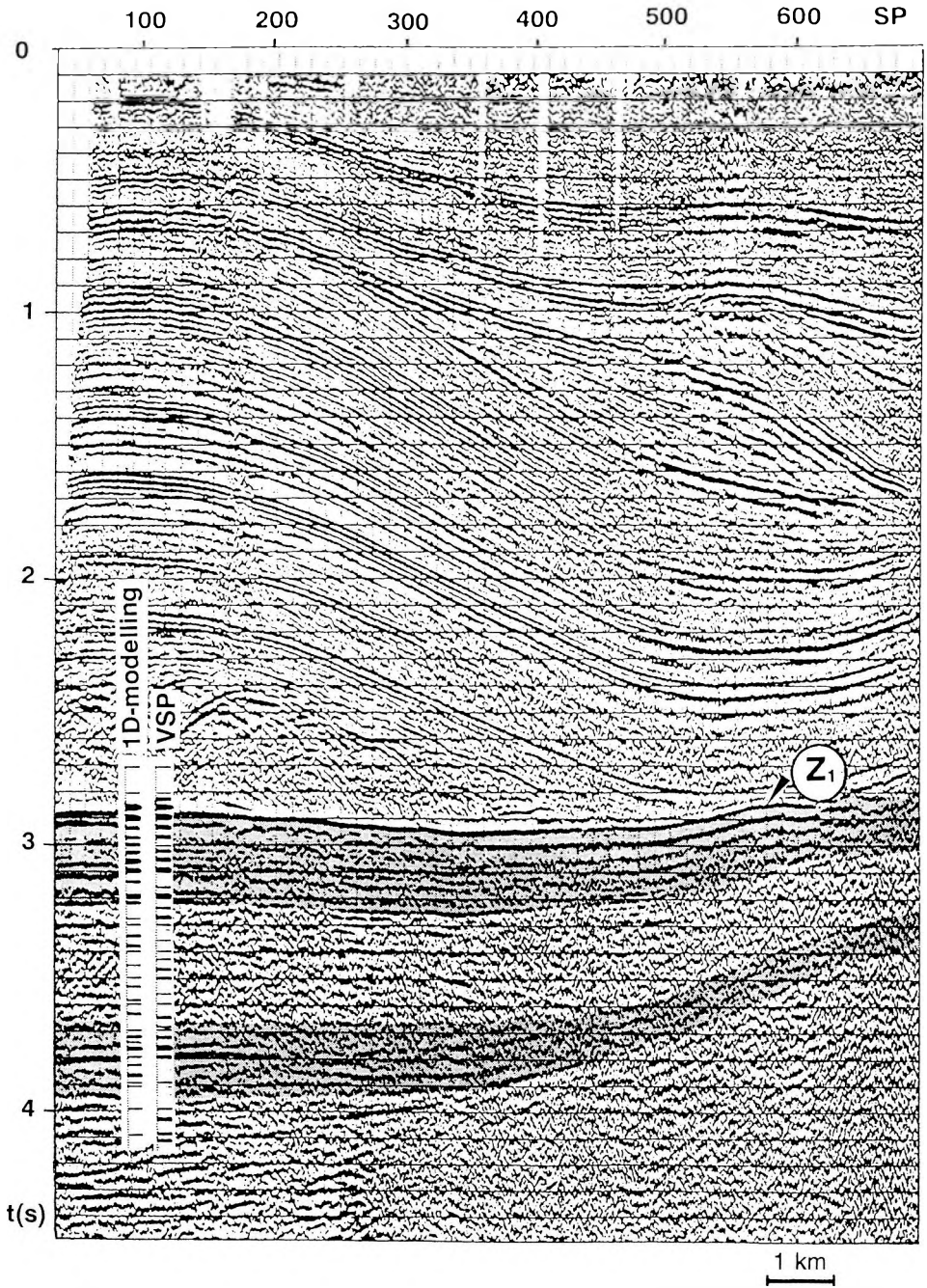


Fig. 6. Seismostratigraphic subdivision of the Rotliegendes on a regional seismic line (part of it)  
 6. ábra. A rotliegendes szeizmosztratigráfiai felosztása egy regionális szeizmikus vonalon (részlet)

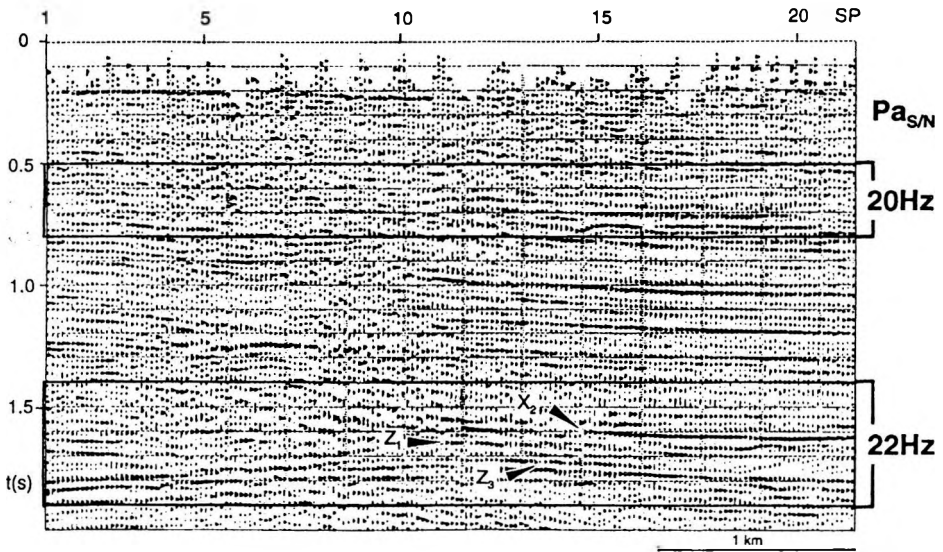


Fig. 7. Zechstein exploration with conventional seismic surveys (Favourable surface conditions, CDP 1200 %)

7. ábra. Zechstein kutatás hagyományos szeizmikus méréssel, kiváló felszíni körülmények, CDP 1200 %

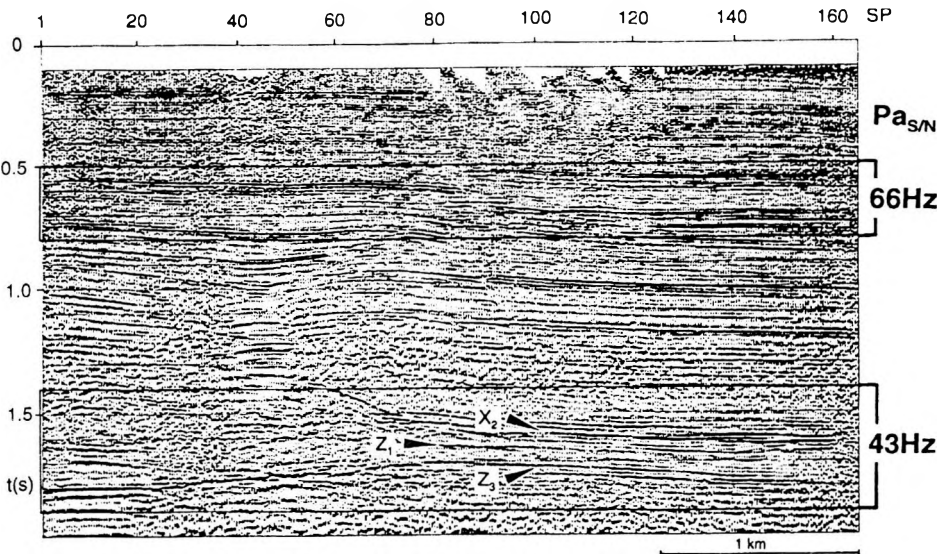


Fig. 8. Zechstein exploration with high-resolution seismic surveys (Favourable surface conditions V, CDP 2400 %)

8. ábra. Zechstein kutatás nagyfelbontású szeizmikus méréssel, kiváló felszíni körülmények, CDP 2400 %

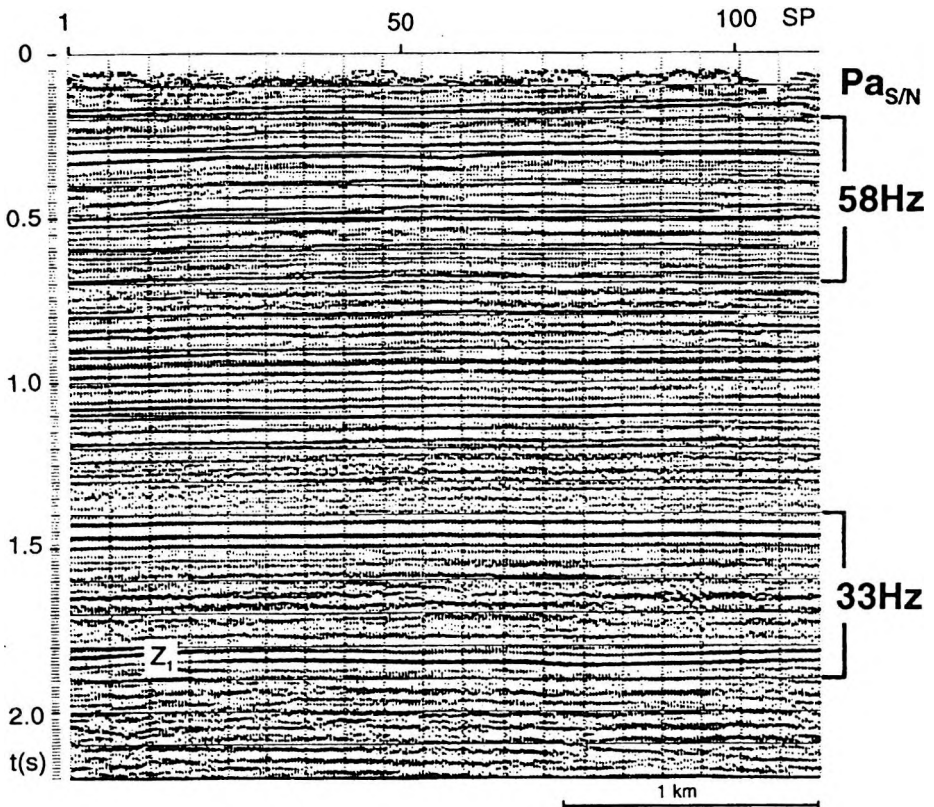


Fig. 9. Zechstein exploration with high-resolution seismic surveys (Simple surface conditions, CDP 4800 %)

9. ábra. Zechstein kutatás nagyfelbontású szeizmikus méréssel, egyszerű felszíni körülmények, CDP 4800 %

low-velocity layers of 40 to 50 m, were more difficult. In conventional seismic surveys a 3-fold pattern of shooting is applied. Using a 96-fold coverage and reduced shot and receiver point intervals of 13 m we achieved interpretable results with high resolution down to the Zechstein after iterative correction of statics (compare *Figs. 10 and 11*).

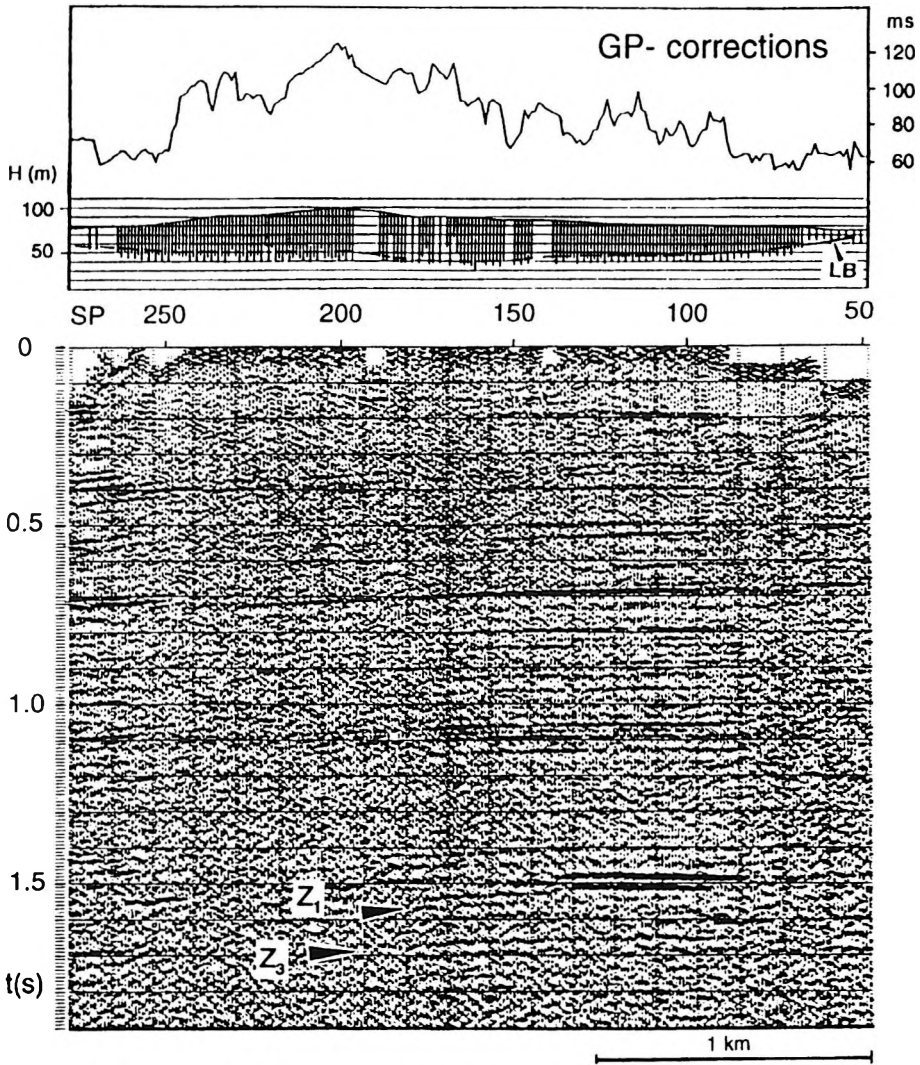


Fig. 10. Zechstein exploration with high-resolution seismic surveys (Complex surface conditions, CDP 9600 %, with field statics)

10. ábra. Zechstein kutatás nagyfelbontású szeizmikus méréssel, bonyolult felszíni körülmények, CDP 9600 %, terepi statikus korrekció

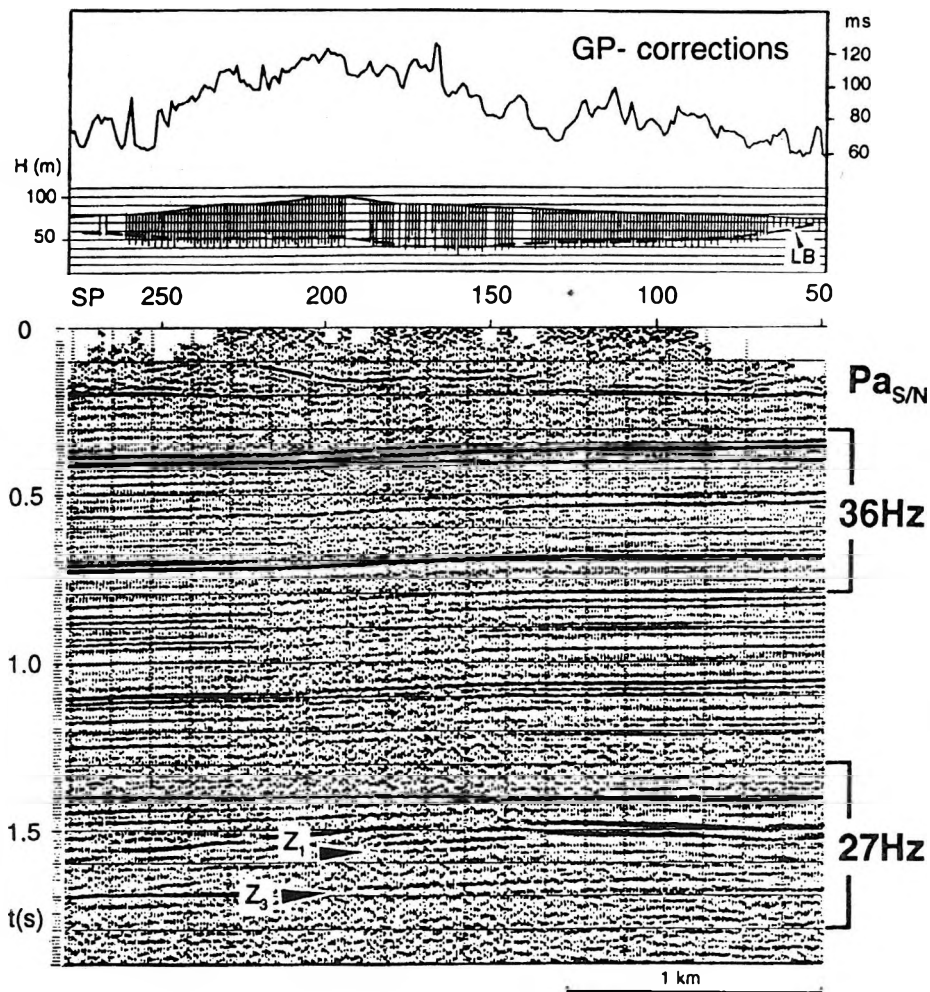


Fig. 11. Zechstein exploration with high-resolution seismic surveys (Complex surface conditions, CDP 9600 %, after iterative corrections of statics)

11. ábra. Zechstein kutatás nagyfelbontású szeizmikus mérésel, bonyolult felszíni körülmények, CDP 9600 %, iteratív statikus korrekció

*Trial of a litho-facial interpretation*

One cause of the drilling of dry boreholes in the search for Stassfurt carbonate deposits in the barrier range is, that they were located on vertexes of horizon  $Z_1$  or thickness anomalies of the layer package  $Z_1...Z_3$ . In the meantime it was found that the carbonate barrier is shifted against the Stassfurt anhydrite barrier expressed by  $Z_1$  [VOIGT 1990]. Moreover, the Stassfurt carbonate has different reservoir properties. Fig. 12, a and b illustrate that HR-seismics provides a much more detailed image of the thickness conditions in the lower Zechstein and on the flank of the barrier. But this does not solve the problem of the optimal location of wells. Hence, it was the goal of HR-seismic interpretation to obtain an assessment of the reservoir properties of the Stassfurt carbonate on the platform and on its margin.

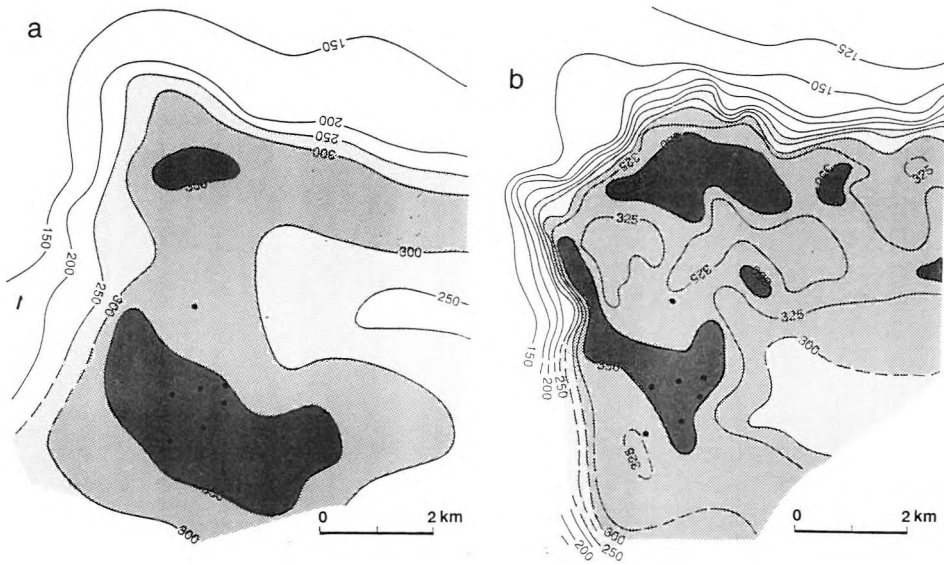


Fig. 12. Isopach map  $Z_1 - Z_3$

a.) Conventional seismic surveys; b.) High-resolution seismic surveys

12. ábra. Izovastagság térkép  $Z_1 - Z_3$  intervallumokról

a) Hagyományos szeizmikus kutatás; b) Nagyfelbontású szeizmikus kutatás

Analysis of the petrophysical parameters of lower Zechstein strata from 25 wells and the consecutive seismic modelling [BAUER, GAERTNER, 1990] provided the basis for a detailed wave picture interpretation between the hitherto used key horizons  $Z_1$  and  $Z_3$ .

Three different formation types of the Stassfurt carbonate were found which also differed clearly in the seismic wave picture at sufficient resolution and S/N-ratio (Fig. 13):

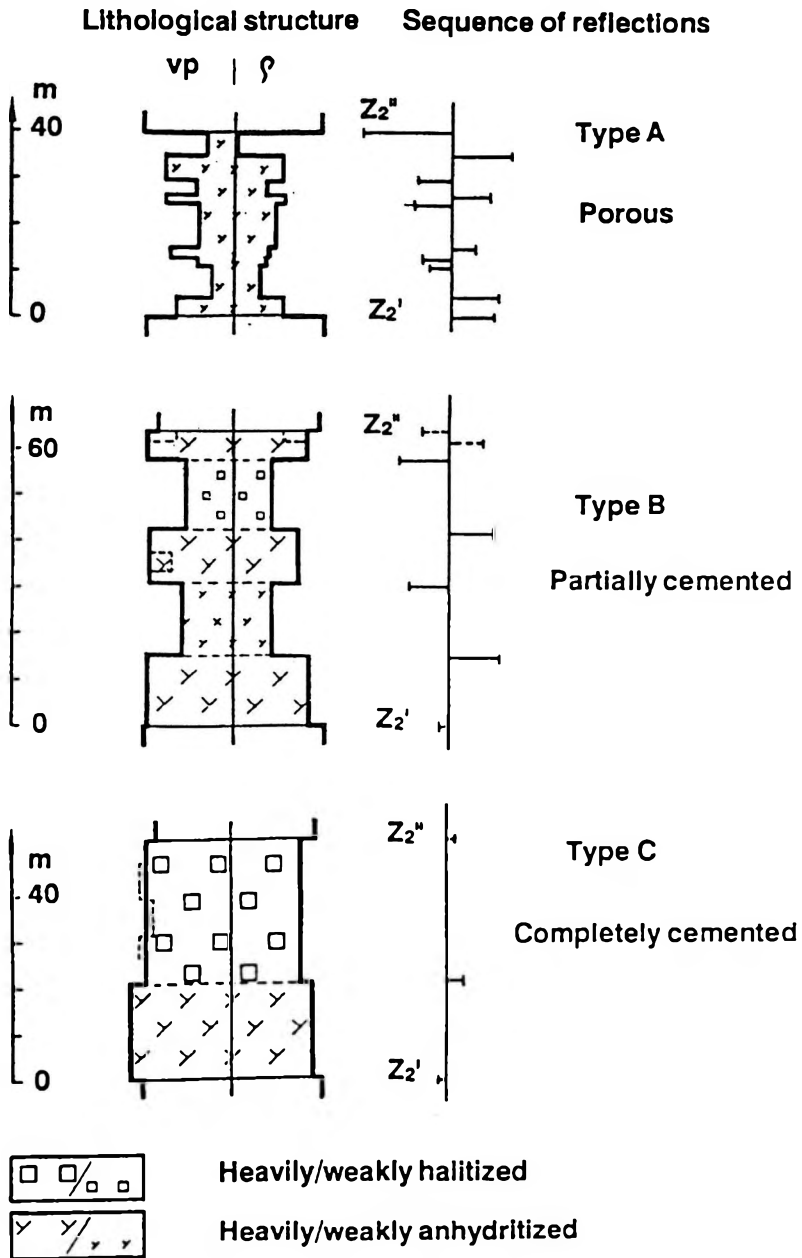


Fig. 13. Forms of Stassfurt formation carbonates  
 13. ábra. A stassfurt-formáció karbonátjainak típusai

*Type A:* Completely porous with clear reflectivity at the upper and lower boundaries.

*Type B:* Partially cemented with alternating porous and cemented layers and a dense series of reflection coefficients yielding an interference signal.

*Type C:* Totally cemented with very weak reflectivity and frequently reversed signs at the lower boundary against type A.

*Type Ü:* Range of transition

We performed seismic modelling on all these lithological types (Fig. 14) and in doing so gained an invaluable better understanding of the wave picture to be expected from different reservoir types.

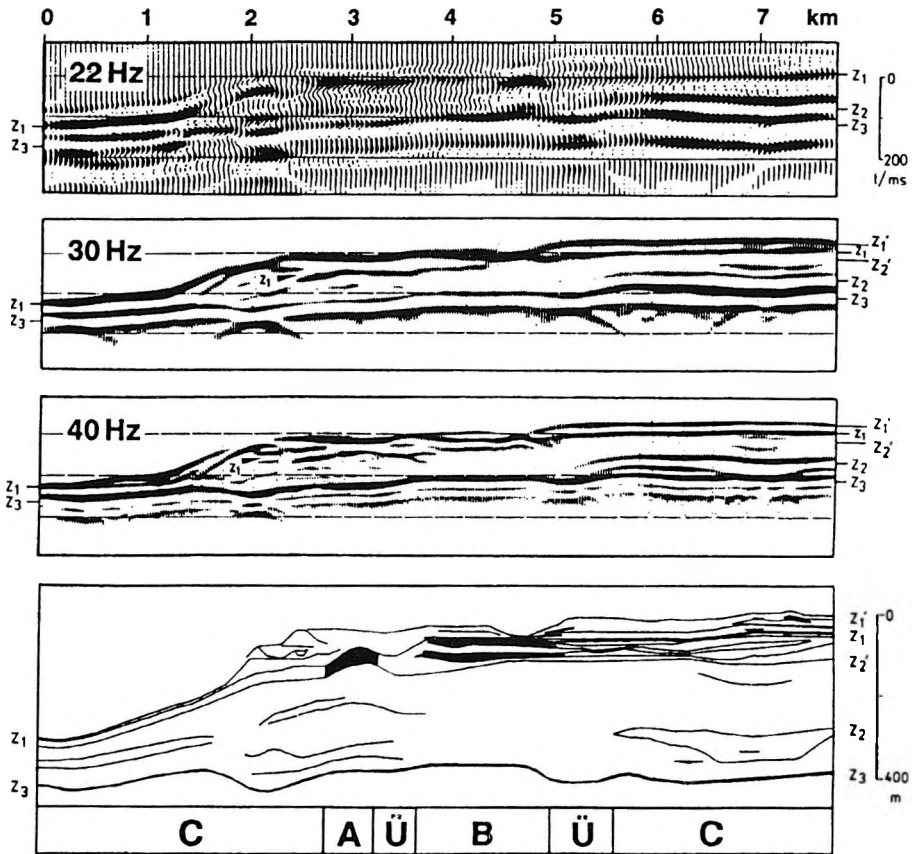


Fig. 14. Model of the lower Zechstein with synthetic time sections  
 14. ábra. Az alsó zechstein modellje szintetikus időszelvényekkel

Based on this new understanding we can derive that prominent amplitude maxima below  $Z_1$  in the stack result can be interpreted as parts of the porous Stassfurt carbonate (Fig. 15, horizon  $Z_2'$ ). It also follows from the modelling

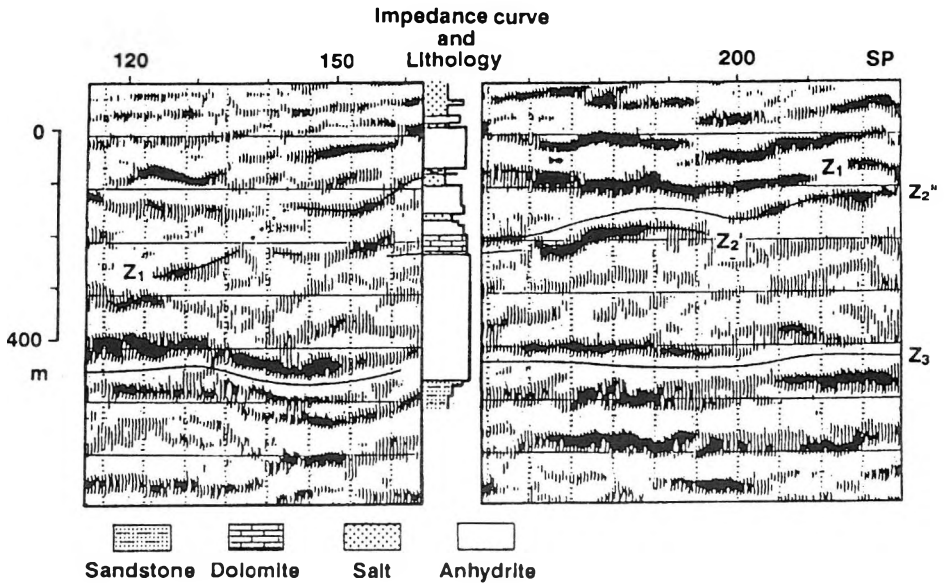


Fig. 15. Wave picture interpretation within the lower Zechstein  
15. ábra. Hullámkép értelmezés az alsó zechsteinen belül

that with the tracing of reflections from the lower boundary of the Stassfurt carbonate, we must expect changes of polarity. We attempted to detect and map the above mentioned 3 reservoir types from the wave picture. As a result of this interpretation the apparent porosity is shown in Fig. 16a. Despite of the mentioned change of polarity and the almost complete lack of a clear reflection from the lower boundary of the Stassfurt carbonate, a map of the probable carbonate thickness was compiled (Fig. 16b), which is additionally supported by drilling results. These maps can be considered as the first trial of a direct seismic data based prognosis of reservoir formation in the Zechstein on east German territory.

Results with still clearer indications in the seismic wave picture of the same character with regard to the Stassfurt carbonate in north western Germany have been published in the meantime [BUDNY 1991].

We wish to thank Erdöl-Erdgas Gommern GmbH (who commissioned the surveys) for permission to publish the results.

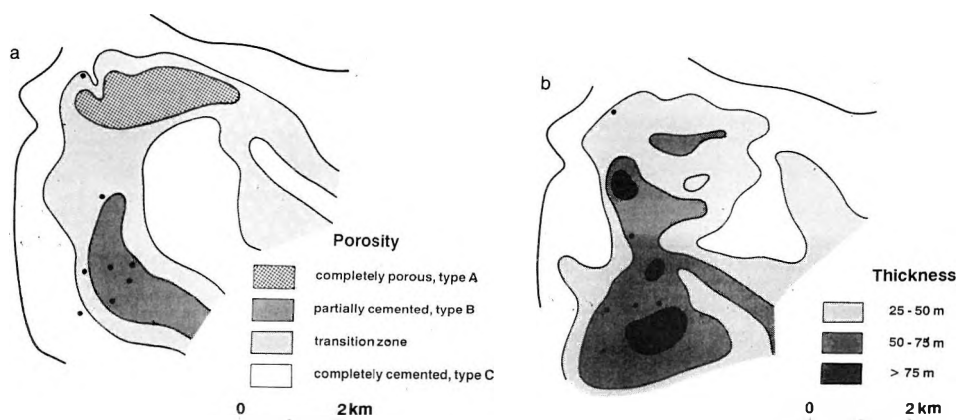


Fig. 16. Porosity (a) and isopach (b) map of the Stassfurt carbonate  
 16. ábra. Porozitás (a) és izovagtság (b) térkép a Stassfurti karbonátokról

#### REFERENCES

- BAUER M., GAERTNER H. 1990: Lithologische Wellenbildinterpretation im basalen Zechstein Südost-Brandenburgs. Paper presented at a meeting of the Ges. f. Geol. Wiss., Fachverband Geologie, Zinnowitz
- BUDIG W., FABIANEK P., MEYER W., STANDKE U. 1977: Automated techniques for seismic wave analysis and experiences from their application. 31st Internat. Geophys. Symp. Budapest (1976), Proc. I, pp. 187-202
- BUDNY M. 1991: Seismic reservoir interpretation of deep Permian carbonates and sandstones (NW German gas province). First Break 9, 2, pp. 55-64
- GAERTNER H., SCHEIBE R.-D. 1987: First results of high-resolution seismics (HRS) applied to the exploration of the Zechstein in the GDR. 32nd Internat. Geophys. Symp. Dresden, Proc. I, pp. 55-73
- GAERTNER H., SCHEIBE R.-D. 1991: Erhöhung des Auflösungsvermögens seismischer Zeitschnitte durch verschiedene Filterverfahren. Geophysik und Geologie; Geophys. Veröff. Univ. Leipzig 4, 2, pp. 17-23
- PILLING R., THOMAS B., WRUCK K. 1984: Applications of areal seismic measurements. 29th Internat. Geophys. Symp. Varna, Proc. I, pp. 199-209
- SCHIKOWSKY P. 1984: Finite-difference migration — an effective means for the interpretation of reflection seismic data. 29th Internat. Geophys. Symp. Varna, Proc. I, pp. 13-25
- VOIGT E. 1990: Speichergeologische und hohlraumgenetische Trends im Staßfurtkarbonat. Paper presented at a meeting of the Ges. f. Geol. Wiss., Fachverband Geologie, Zinnowitz
- WRUCK K., HORST W., HOFFMANN H. 1987: Deep reflection seismic pilot surveys in the GDR — methodics and geological interpretation. 32nd Internat. Geophys. Symp. Dresden, Proc. I, pp. 288-303

## OLAJ ÉS GÁZ KUTATÓ REFLEXIÓS SZEIZMIKUS MÉRÉSEK ÉSZAKKELET-NÉMETORSZÁGBAN

H. GAERTNER, K. H. FEßER, W. KÜSTERMANN, S. PRÖHL, H. WOLFF,  
K. WRUCK

Áttekintést ad a Geophysik GmbH által Északkelet-Németországban az utóbbi néhány évben folytatott reflexiós szeizmikus kutatásról. A kutatás legfőbb tárgyai a zechstein és rotliegendes formációk voltak. A rendszerint nagyon bonyolult szeizmogeológiai feltételek mind az adatgyűjtésben, mind a feldolgozásban és értelmezésben speciális eljárásokat igényeltek, melyeket az adott kutatási célhoz igazítottak.

A rotliegendes formációt a medence margiális zónájában, a zechstein aljzatról érkező reflexiók nyomkövetésével kutatták két- és három-dimenziós mérésekkel. Magából a rotliegendesből is sikerült észlelni és nyomkövetni a reflexiókat a kismértékű közetfizikai elkülönülés, a nagy mélység és a többszörös hullámok intenzív megjelenése ellenére. Bizonyos esetekben szeizmografiai kiértékelésre is lehetőség volt. A zechstein kutatásában néhány speciális nagyfelbontású szeizmikus módszert alkalmaztak. A hagyományos szeizmikus kutatással összehasonlítva ezek sokkal részletesebb szerkezeti kép kialakítását tették lehetővé. Továbbá, a hullámképanalízissel lehetőség nyílt arra, hogy a zechstein fáciesjellegéről is információkat kapjanak, és észleljék a megnövekedett porózitású területeket.

## SEISMIC SIGNAL ANALYSIS IN PARTIALLY FLUID SATURATED MEDIA

Adel A. A. OTHMAN\*

A geologic model is proposed for studying the effects of fluid saturation on seismic velocity and, consequently, on seismic amplitudes. Partial gas-saturation as well as partial oil-saturation are introduced. Synthetic seismograms were calculated to show the desired effects. Attenuation effects were introduced and calculated.

Computations revealed that higher concentration values of water in pores decreases the amplitude of seismic waves. Also, low gas saturation mixed with water causes relatively large decrease of relative amplitude — and that is greater than that caused by introducing oil in pores.

**Keywords:** seismic velocity, water saturation

### 1. Introduction

The interstitial water in rocks and solids has little or no effect on density, magnetism, and radioactivity, but it does cause considerable changes in elastic moduli and electrical conductivity — as is known from the literature. Many studies have been carried out to show the effect of water saturation on propagated seismic waves. Particular attention was paid to studying the seismic waves from simultaneous inversion of velocity and attenuation data to obtain improved earth models [RANDELL 1976]; the study of 'bright spots' in hydrocarbon exploration was also considered by SHERIFF [1975]. However, to make full use of seismic data, it is essential to interpret the effects of water saturation on the physical properties of rock.

\* University of Qatar, Geology Dept., P.O.Box 2713, Doha, Qatar  
Permanent address: Al-Azhar University, Faculty of Sciences, Geology Department, Nasr-city, Cairo, Egypt  
Manuscript received (revised version): 25, June 1993

DESAI and MOORE [1967] have reported laboratory measurements of compressional wave velocity in Berea sandstone. They used a time average equation [WYLLIE et al. 1962] and observed a decrease in the matrix travel time. The influence of pore fluids on seismic waves has been reported by several investigators, e.g. NUR, SIMMONS 1969, NUR 1973, ELLIOT, WILLEY 1975, DOMENICO 1974. Among recent works in this area are those of OGUSHWITZ [1985], and DUNN [1986]. HALPERN and CHRISTIAN [1986] studied numerically the contact between a disk and the fluid-saturated half-space. PHILLIP-PACOPOULOS [1987 and 1989] discussed the propagation of Rayleigh waves in fully saturated uniform half-spaces.

The impedance contrast between gas and rock is so high that the dominant effect would be *P*-wave reflection or refraction with relatively little *S*-wave generation [LERCHE, PETROY 1986]. The present work investigates the compressional wave propagation in rocks, as an aid in seismic exploration, and the action of water saturation under different conditions of porosity and attenuation on seismic amplitudes applying the synthetic seismogram technique.

## 2. Propagation of elastic waves in partially fluid-saturated rocks

The seismic wave motion equation can be discussed in terms of the concept of normal incidence reflection in the saturated case. The wave equation for the acoustic wave form is as follows:

$$\rho (\partial^2 \vec{u} / \partial t^2) = (\lambda + \mu) \nabla^2 \theta + \mu \nabla^2 \vec{u} \quad (1)$$

with

$$\theta = \nabla \cdot \vec{u}$$

and

$$\nabla^2 \vec{u} = \nabla (\nabla \cdot \vec{u}) - \nabla \times (\nabla \times \vec{u}) \quad (2)$$

Then

$$\rho (\partial^2 \vec{u} / \partial t^2) = (\lambda + \mu) \nabla (\nabla \cdot \vec{u}) + \mu \nabla^2 \vec{u} \quad (3)$$

$$\rho (\partial^2 \vec{u} / \partial t^2) = (\lambda + 2\mu) \nabla (\nabla \cdot \vec{u}) - \mu \nabla \times \nabla \times \vec{u} \quad (4)$$

In the above equations,  $\rho$  is the density of the rock,  $\vec{u}$  is the particle *displacement vector*,  $t$  is the time,  $\lambda$  and  $\mu$  are Lamé's constants. Biot's theory predicts three kinds of body waves, two dilatational and one shear [BIOT 1956 a, b]. One of the dilatational waves, which is called the first kind, and the shear wave are similar to waves found in ordinary elastic media. The second kind of compressional wave is highly attenuated, in the nature of a diffusion process

[STOLL 1974]. For geophysical studies in fluid saturated sediments waves of the first kind are of principal interest. In the present study  $P$ -waves of the first kind propagated in porous media will be discussed by introducing  $u$  as the irrotational vector (i.e.  $\nabla \times u = 0$ ), thus :

$$\nabla(\nabla \cdot \vec{u}) = \nabla \cdot \nabla \vec{u} \quad (5)$$

and by introducing the partially saturated condition by applying the time average equation, the wave will take the form:

$$\partial^2 \vec{u} / \partial t^2 = [\Phi / V_f + (1 - \Phi) / V_m]^{-2} \nabla^2 \vec{u} \quad (6)$$

where  $\Phi$  is the fractional porosity,  $V_m$  the matrix velocity, and  $V_f$  the fluid velocity. A solution of the wave equation in the  $x$ -direction may be presented as follows:

$$u = u_0 \exp \{ ik (x - V_f V_m t [\Phi (V_m - V_f) + V_f]^{-1}) \} \quad (7)$$

where  $u_0$  is a constant,  $i = (-1)^{1/2}$ ,  $k$  is the wave number, and  $x$  represents the distance. But in gas-saturated media, the modified time average equation [MARSCHALL 1984], may change the form of equation (7) into:

$$u = u_0 \exp \{ ik (x - BV_g V_m V_w t [\Phi V_m (BV_g S_w + V_w - V_w S_w) + BV_g V_w (1 - \Phi)]^{-1}) \} \quad (8)$$

where  $S_w$  is water saturation,  $V_w$  is the velocity of a propagated wave in the water,  $V_g$  is velocity of a wave in gas, and  $B$  is equal to  $\log (C_g / C_m)$ .  $C_g$  is the gas compressibility, and  $C_m$  is the matrix compressibility in dyne/cm<sup>2</sup>. The subscripts  $f$  and  $m$  refer to fluid (oil, gas and water), and matrix (the mineral grains of the rock frame), respectively.

Many mathematical operations will be made to establish a synthetic seismogram applying the reflectivity technique to follow changes of the seismic amplitudes due to changes in degree of water saturation. A geological model is therefore designed (Fig. 1). In this figure a three layer model is illustrated; there is non-porous shale at the top and bottom of the model; limestone, sandstone or dolomite is the composite of the middle layer. The suggested seismic velocities applied in the designed model are as follows: for limestones 6400 m/sec, for dolomite 7000 m/sec, and for sandstone 5500 m/sec. Finally, for the shale the seismic velocity is taken to be 4500 m/sec. The abbreviations *SH*, *LS*, *DOL*, and *SS* denote shale, limestone, dolomite, and sandstone; respectively. These symbols will be used hereafter as well as in the figures. Another group of abbreviations are applied in the present work, viz. *G* which means gas, *O* means oil, and *W* denotes water. The abbreviation *SW* appears in every figure near the upper trace; it denotes the applied source wavelet.

A ray striking the upper interface between layer 1 and layer 2 is partly reflected from the top of layer 2 and partly travels to the base of layer 2, here the ray is then reflected and transmitted through layer 1. By changing the physical parameters in layer 2, many variations arose.

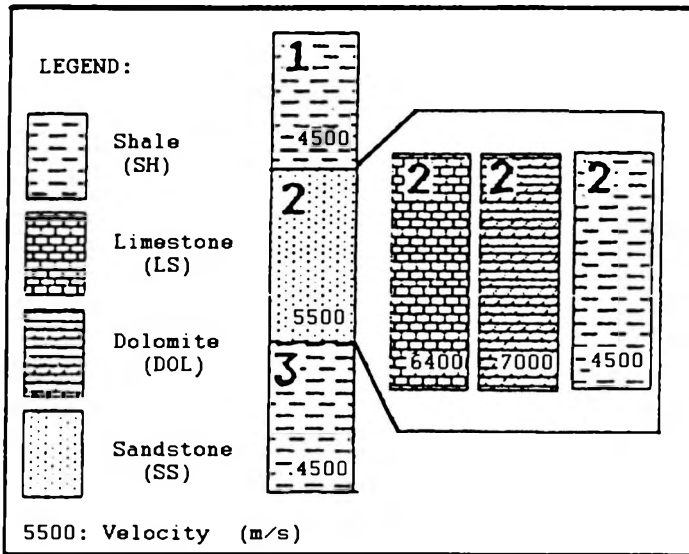


Fig. 1. Geologic model used to compute the synthetic seismograms in the present work  
 1. ábra. A szintetikus szeizmogramok kiszámításához felállított földtani modell

### 3. Elastic wave velocities under partially saturated conditions

Generally, the calculated porosity values of the studied three rocks are the average values from the selected porosity ranges. For dolomite, the porosity range is 5% to 15%; for limestone it is from 10% to 20%; in the case of sandstone, the range is selected as 15% to 35%. Therefore, the calculations of velocity in Fig. 2 were carried out at porosities of 10% for dolomite, 15% for limestone, and 25% for sandstone.

The velocity of seismic waves is strongly dependent on pore fluid content. The degree of wave interactions with fluids is determined by the shape of the pores within the solid matrix of mineral grains. In the low frequency limit, pore fluids influence the velocity through compressibility. The dependence of velocity on fluid porosities can serve for a diagenesis of material structure in situ as well as in the laboratory. Theoretical and experimental correlations between longitudinal wave velocities, rock type, and fluid content have been made at different localities in the shallow crust.

The goal in oil and gas exploration is to distinguish between gas, oil, and water in situ, as well as to infer their relative concentrations, rock type, porosity, and permeability. Water saturation as inspected from the time average equation

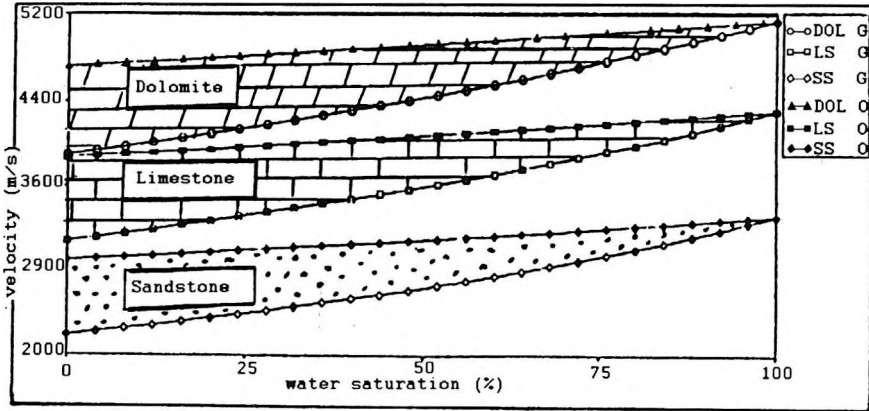


Fig. 2. Effects of water saturation on the acoustic velocities in both partial gas- and oil-saturated cases for dolomite, limestone and sandstone. G—gas, O—oil

2. ábra. A víztelítettség hatása az akusztikus sebességekre, parciálisan gázzal ill. olajjal telített dolomitoknál, mészkőnél és homokkőnél. G — gáz, O — olaj

or from the modified one, has effects on seismic velocity. These effects are calculated for both gas and oil-filling pores mixed with water.

Figure 2 illustrates velocity as a function of water saturation for the modelled three rocks. The velocity of the hydrocarbon-filled portions of a reservoir is low relative to the water saturated condition as shown in the figure. Velocities show higher values in oil-saturated rocks than those of gas saturated ones. Generally speaking, the velocity values in partially saturated dolomite are greater than those calculated in the other two rocks. Also, the velocity is slightly affected by water saturation in sandstone.

As shown in Fig. 2, seismic velocity increases as saturation of the pore volume with water increases in the rock. The differences between the values of velocities in both gas- and oil-saturated cases decrease with increasing water saturation percentage. It is equal to zero at fully water saturated state.

The seismic velocity in the matrix of a rock as written in Fig. 1 is highly affected by the porosity values and type of pore filling liquid. These calculations agreed with those of ELLIOT and WILLEY [1975], which indicate that the velocity of a liquid saturated rock can vary from that in the same rock containing a partial saturation of a free gaseous phase.

#### 4. Analysis of waveforms aided by synthetic seismograms

In seismic measurements, for a given lithologic contrast, the reflection coefficient (RC) depends on the angle of incidence, and on the types of incident and reflected wave. The resultant convolution of the reflectivity function  $R(t)$

and source signature  $W(t)$  represents the synthetic seismogram  $S(t)$ , which may be expressed in mathematical formulation as:

$$\begin{aligned} S(t) &= \int W(\tau) R(t-\tau) d\tau \\ &= W(t) * R(t) \end{aligned} \quad (9)$$

If noise  $N(t)$  is considered, equation (9) can be rewritten as follows:

$$S(t) = W(t) * R(t) + N(t) \quad (10)$$

The noise includes multiple reflections, the combined effect of all instruments, pulse geophone coupling, and others.

A geological model was proposed to calculate synthetic seismograms (Fig. 1). As is known, models are only approximations to reality whereas mathematical relations are precise but they do not correspond to reality under all conditions. Any model is useful because it provides a framework for the description of deviations from ideality and may lead to a better model. The suggested model is transversely isotropic, and the source pulse propagates as a plane wave, thus striking the layers at normal incidence. In the studied model, all types of noise are excluded.

The source signature waveform is time-invariant; thus its shape and amplitude are constant and do not change with travel time. Synthetic reflection traces have been calculated to evaluate reflection amplitude variations in terms of corresponding changes of water saturation at definite porosity value.

These computations have been carried out for dolomite, limestone and sandstone, in layer 2 encased within non-porous shale (Fig. 1). For every rock, the pores are assumed to be filled with either gas or oil in addition to water at different degrees of concentration. The porosity values vary in the selected range for every rock.

In Figs. 3 to 8, dolomite was chosen to emphasize the effect of fluid content. In the porosity range (5–15%), two mixed saturated cases were studied. Gas and/or oil are mixed with water. A series of synthetic traces are plotted in Fig. 3 for a porosity value of 5% and a wide range of water saturation. The limiting conditions of zero gas saturation ( $S_w = 100\%$ ), and full gas saturation ( $S_w = 0\%$ ), show no polarity reversals, and they show a decrease of the travel time of the second event which is reflected from the base of layer 2. For a mixed saturated case, polarity reversals appear where the porosity value was increased to 10%, as seen in the window of Fig. 4. A greater travel time is observed at the 5% porosity value. In Fig. 5, a reversal of polarity is observed throughout the saturation range and there is also an increase in travel time. The reversals are considered with respect to the case of porosity equal to zero and are plotted at the upper side of the figure. The zero porosity trace will be plotted in all the following calculated seismograms for comparison. Oil-water mixtures are introduced in the pores of dolomite. Synthetic seismograms have been calculated and plotted as shown in Fig. 6 to 8. Polarity reversals are observed at high porosity values (i.e. porosity = 15%). Travel times are increased by increasing porosity in the whole water saturation range.

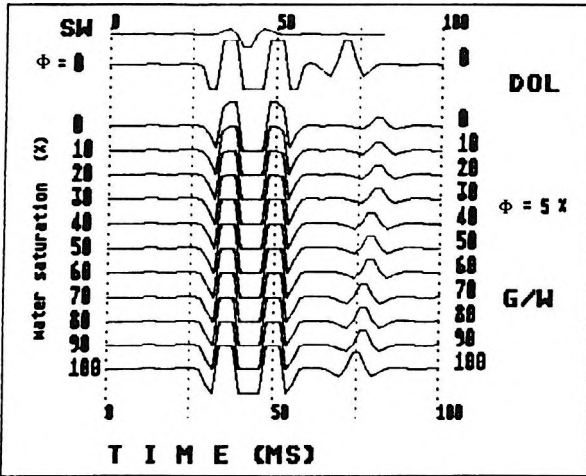


Fig. 3. Synthetic seismograms computed for partially gas-saturated dolomite, for different  $S_w$  values (0-100%), at porosity of 5%

3. ábra. Részben gázzal telített dolomitokra számított szintetikus szeizmogramok, különböző  $S_w$  értékekre (0-100%), 5% porozitás mellett

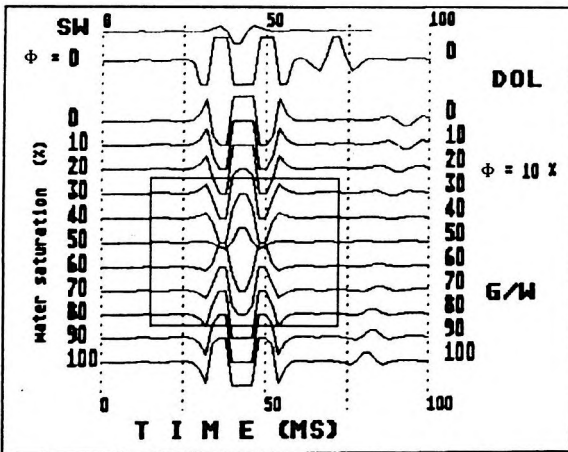


Fig. 4. As for Fig. 3 but for porosity of 10%

4. ábra. Mint a 3. ábra, de 10% porozitás esetén

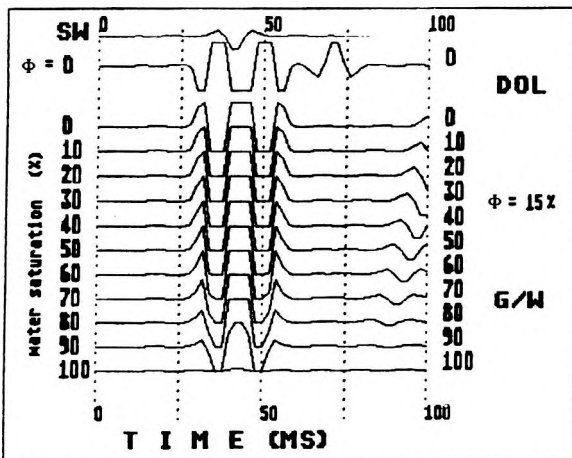


Fig. 5. As for Fig. 3 but for porosity of 15%

5. ábra. Mint a 3. ábra, de 15% porozitás esetén

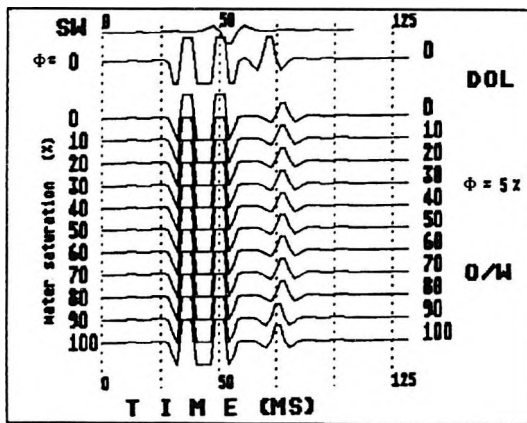


Fig. 6. Synthetic seismograms computed to partially oil-saturated dolomite, for different  $S_w$  values (0-100%), at porosity of 5%  
6. ábra. Részben olajjal telített dolomitokra számított szintetikus szeizmogramok, különböző  $S_w$  értékekre (0-100%), 5% porozitás mellett

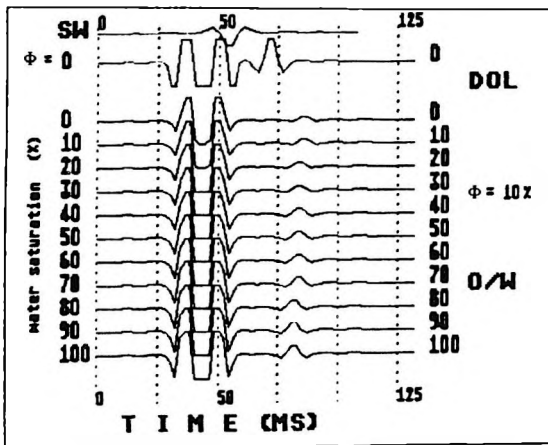


Fig. 7. As for Fig. 6 but for porosity of 10%  
7. ábra. Mint a 6. ábra, de 10% porozitás esetén

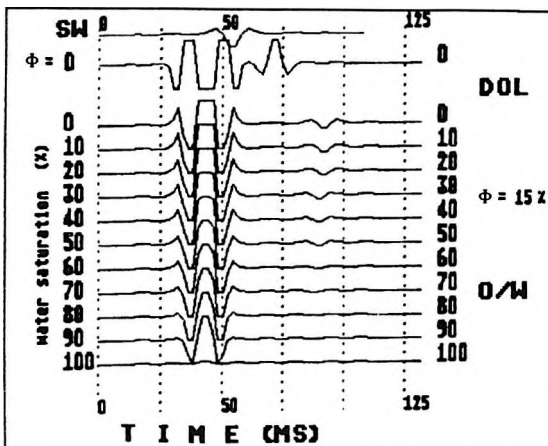


Fig. 8. As for Fig. 6 but for porosity of 15%  
8. ábra. Mint a 6. ábra, de 15% porozitás esetén

The relative amplitudes of seismic events to the incident ones were calculated for both gas and oil mixed with water, and are shown in semi-log scale in Fig. 9. Relative amplitude changes are small at low water saturation percentage. Polarity reversals appear at higher porosities. Also, a low gas saturation in partially water saturated dolomite causes a relatively large decrease of relative amplitudes, but a low oil saturation causes a larger decrease of relative amplitudes than that of the gas saturation one.

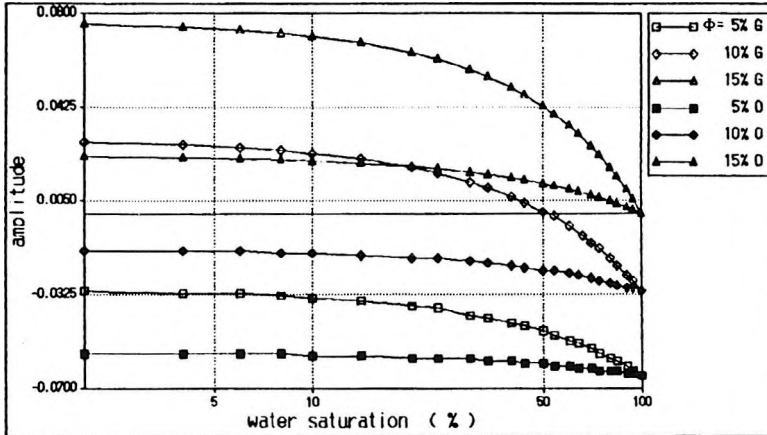


Fig. 9. Seismic amplitude and water saturation for different porosities at 5%, 10%, and 15% in dolomite. G—gas; O—oil

9. ábra. Szeizmikus amplitúdó és vízelíttség különböző porozitásértékek (5, 10 és 15 %) esetén dolomitban. G — gáz, O — olaj

With regard to limestone, a series of synthetic seismograms were plotted with fully gas- or oil-saturated limestone ( $S_w=0\%$ ), and ended with fully water-saturated limestone ( $S_w=100\%$ ). Three figures (Fig. 10, 11, and 12), show the changes of seismic amplitudes against changes of water saturations

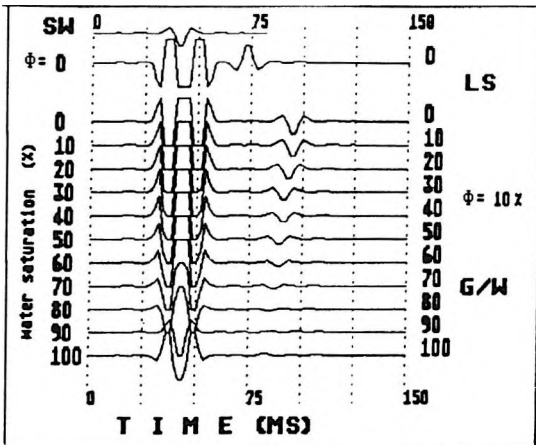


Fig. 10. Seismic amplitudes in partially gas-saturated limestone over wide range of  $S_w$  values, for porosity of 10%  
 10. ábra. Szeizmikus amplitúdók részlegesen gázzal telített mészkőben, az  $S_w$  széles skálájára, 10 % porozitás esetén

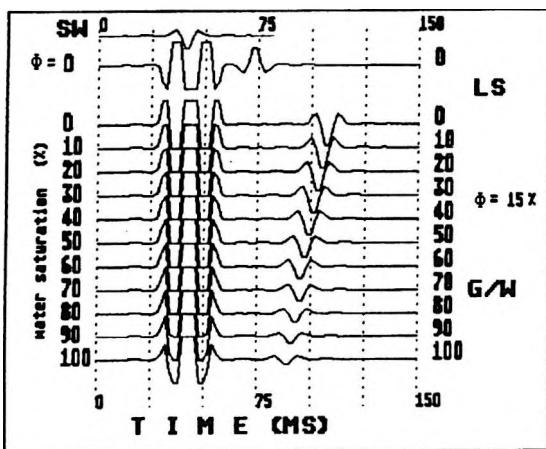


Fig. 11. As for Fig. 10 but for porosity of 15%  
11. ábra. Mint a 10. ábra, de 15% porozitás esetén

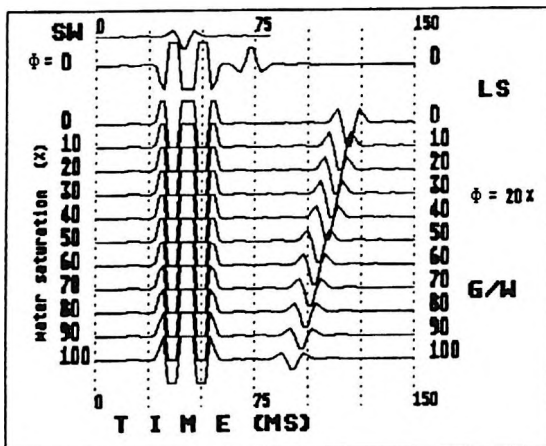


Fig. 12. As for Fig. 10 but for porosity of 20%  
12. ábra. Mint a 10. ábra, de 20% porozitás esetén

at porosities equal to 10%, 15%, and 20%. It is obvious that the travel time of the second event was increased by increasing porosity values, and decreased by increasing water saturations. There are polarity reversals throughout the selected porosity range, which could be observed by comparing the plotted seismograms with the topmost one of every drawing when porosity equals zero (i.e. massive medium). The same pattern was obtained with small gas contents at low porosity as well, see Fig. 10. The polarity reversals appeared at  $S_w=90\%$  in the case of oil-saturated limestones, they also appeared in the case of gas-saturated ones at a lower degree of water saturation (i. e.  $S_w=60\%$ ), as presented in Figs. 10 to 15.

Relative amplitudes of the studied limestone and water saturation are plotted in Fig. 16. As shown, small quantities of gas in pores decrease the amplitude faster than the equivalent values of oil. Low porosity shows low relative amplitudes.

In sandstones, the polarity reversals are recorded and the arrival times of the second event increase by increasing porosity values. The second event in sandstone, as shown in Figs. 17 to 22, is reached later than that in dolomite or

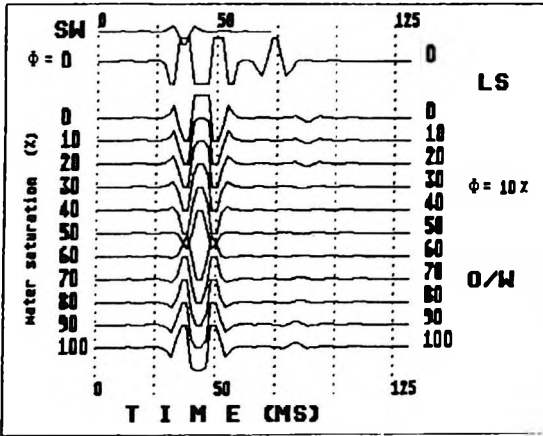


Fig. 13. Seismic amplitudes in partially oil-saturated limestone over wide range of  $S_w$  values, for porosity of 10%

13. ábra. Szeizmikus amplitúdók olajjal részlegesen telített mészkőben, az  $S_w$  széles skálájára, 10 % porozitás esetén

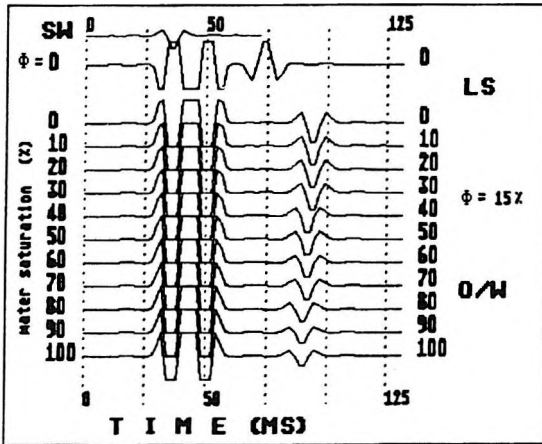


Fig. 14. As for Fig. 13 but for porosity of 15%

14. ábra. Mint a 13. ábra, de 15 % porozitás esetén

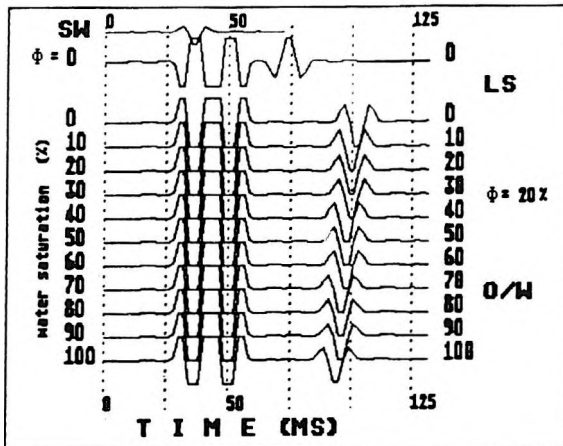


Fig. 15. As for Fig. 13 but for porosity of 20%

15. ábra. Mint a 13. ábra, de 20 % porozitás esetén

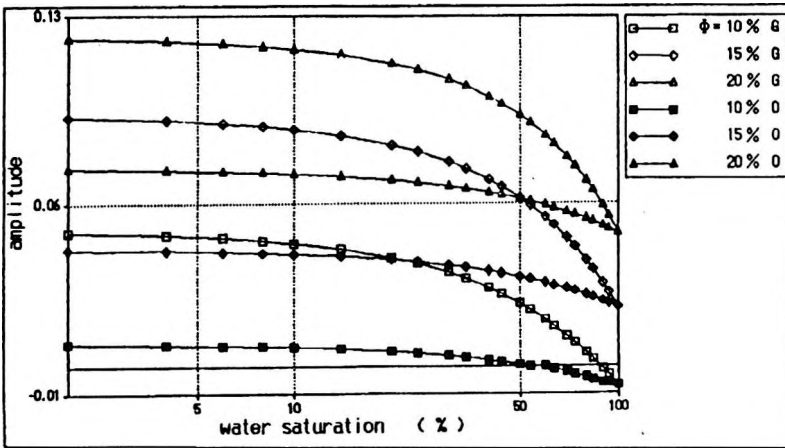


Fig. 16. Seismic amplitude and water saturation for different porosities at 10%, 15%, and 20% in limestone. G—gas; O—oil

16. ábra. Szeizmikus amplitúdó és víztelítettség különböző porozitásértékek (5, 10 és 15 %) esetén mészkövekben. G — gáz, O — olaj

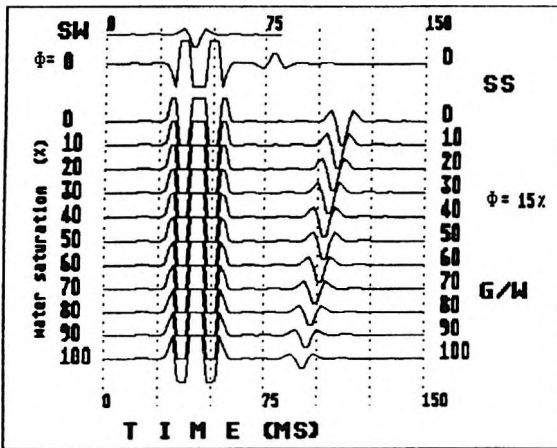


Fig. 17. Amplitudes as a function of  $S_w$  in partially gas-saturated sandstone for porosity of 15%

17. ábra. Amplitúdók az  $S_w$  függvényében gázzal részlegesen telített homokkövekben 15% porozitás mellett

limestone. A comparative representation of relative amplitude with water saturation at three porosity values is given in Fig. 23. Seismic amplitudes suffer small changes in high porous sandstone, at small water saturations. A low gas saturation causes a large decrease of relative amplitudes. This decrease is larger at low porosity values (i.e. porosity=15%)

Variations of seismic amplitudes against pore volume saturated with water are collected together in one plot (Fig. 24). The presence of gas in porous sandstone gives higher amplitudes than that of a partially oil saturated case. Amplitudes for both gas or oil mixed with water in sandstone are higher than that in limestone or dolomite. Low gas saturation causes a relatively large decrease of relative amplitudes in the three studied rocks. Nevertheless, the effects of gas saturation on seismic amplitudes are greater than that of oil.

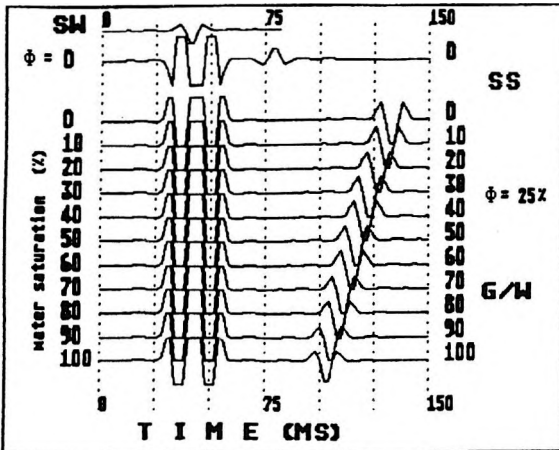


Fig. 18. As for Fig. 17 but for porosity of 25%  
18. ábra. Mint a 17. ábra, de 25 % porozitás esetén

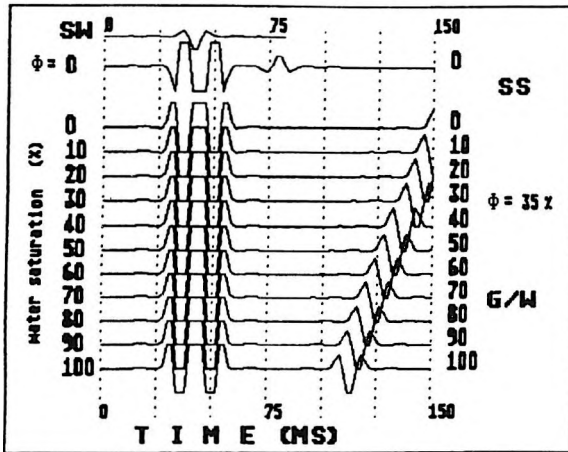


Fig. 19. As for Fig. 17 but for porosity of 35%  
19. ábra. Mint a 17. ábra, de 35 % porozitás esetén

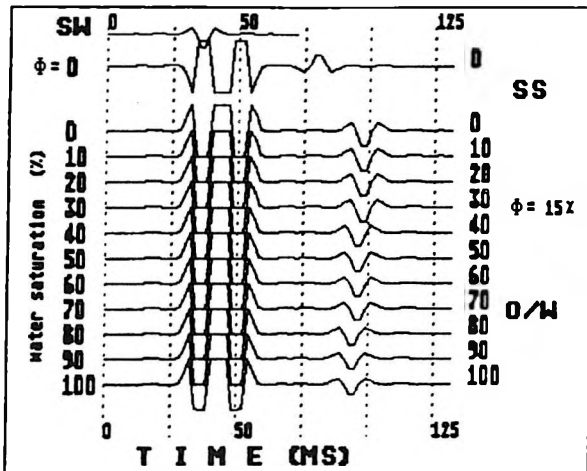


Fig. 20. Amplitudes as a function of  $S_w$  in partially oil-saturated sandstone for porosity of 15%  
20. ábra. Amplitúdók az  $S_w$  függvényében olajjal részlegesen telített homokkövekben 15 % porozitás mellett

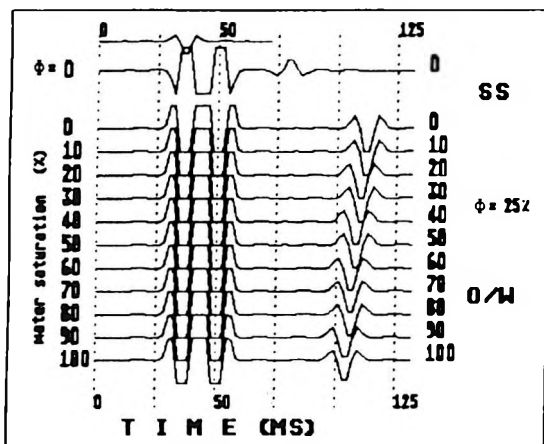


Fig. 21. As for Fig. 20 but for porosity of 25%  
21. ábra. Mint a 20. ábra, de 25 % porozitás esetén

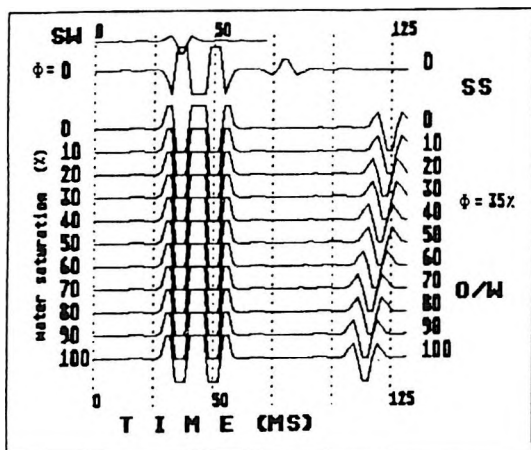


Fig. 22. As for Fig. 20 but for porosity of 35%  
22. ábra. Mint a 20. ábra, de 35 % porozitás esetén

## 5. Influence of attenuation and partial saturation on velocity

As stated in several previous works, e.g. WALSH 1969; ANDERSON, SPETZLER 1970; WHITE 1975, attenuation of waves in fluid saturated porous material may be due to the sum of the loss caused by the fluid motion and the loss caused by the solid framework. The solid framework loss may be regarded as two parts, a dry loss of the solid friction type and a viscous loss resulting from the chemical and physical effect of the fluid on the cementing material of the solid and within cracks of the grains themselves [WYLLIE et al. 1962]. In the low frequency limit, pore fluids influence the propagated waves through their density, compressibility, etc. But at higher frequencies, viscous and inertial interactions are introduced [BIOT 1956 a, b] In the studied model, the source wavelet is set to be of low predominant frequency.

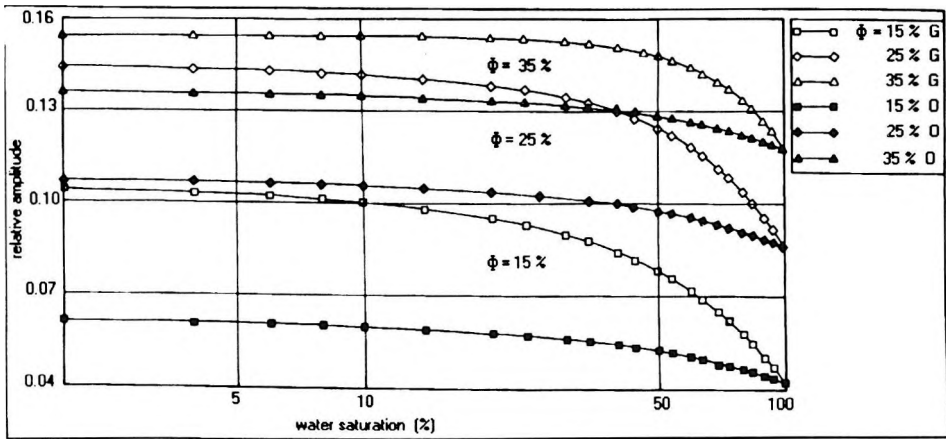


Fig. 23. Seismic amplitude and water saturation for different porosities at 15%, 25%, and 35% in sandstone. G—gas; O—oil

23. ábra. Szeizmikus amplitúdó és víztelíttség különböző porozitásértékek (15, 25 és 35 %) esetén homokkövekben. G — gáz, O — olaj

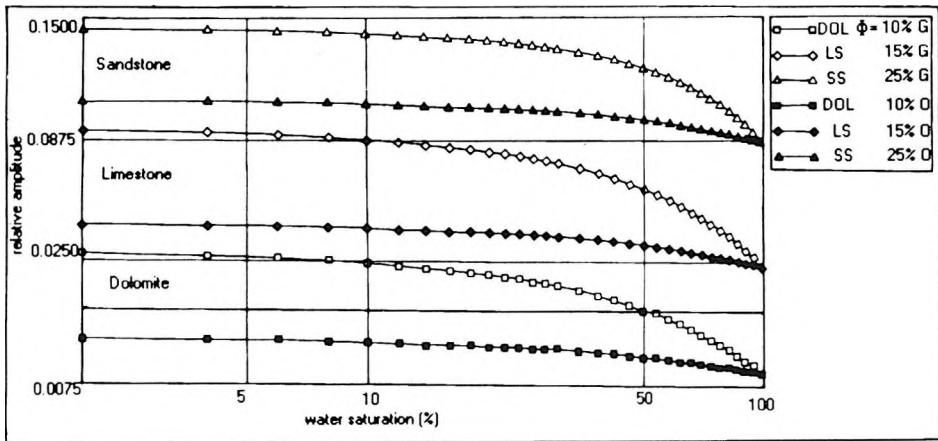


Fig. 24. Seismic amplitudes in both gas- and oil-saturated dolomite, limestone and sandstone as a function of water saturation ( $S_w$ ). G—gas; O—oil

24. ábra. Szeizmikus amplitúdók gázzal és olajjal telített dolomitokban, mészkövekben és homokkövekben, a víztelíttség ( $S_w$ ) függvényében. G — gáz, O — olaj

By neglecting the effects of chemical and physical interactions of the fluid with the adjacent material, the attenuation is only considered in accordance with the solid friction type. Therefore, a nearly constant  $Q$ -model is needed to calculate the effects of attenuation in saturated material on velocity.

The suggested nearly constant  $Q$ -model by KJARTANSSON [1979], was used for the following computations. In this model, the dependence of the velocity upon frequency is considered to be of the form:

$$V = V_r(f/f_r)^A \quad (11)$$

with

$$A = (\tan^{-1}[1/Q])/\pi \quad (12)$$

and equation (11) may be written as:

$$V \approx V_r(f/f_r)^{1/\pi Q} \quad (13)$$

where  $f$  is the frequency,  $f_r$  is a reference frequency,  $V_r$  is the calculated velocity by using a time average or modified time average equation, at the reference frequency.  $Q$  is the quality factor. MAVKO and NUR [1977] reported that for certain rocks with at least a small concentration of very flat pores, even a small amount of water can enhance the dissipation of energy of compressional waves.

Effects of attenuation on seismic velocity in partially saturated case are calculated and plotted in Fig. 25. The three values of  $Q$  are applied in the constant  $Q$  equation (13) to calculate velocity. These values of  $Q$  are equal to 10, 50, and 100 in both partially gas- and oil-saturated cases.

In general, all calculations were executed in both elastic (no dissipation effects), and anelastic cases, as shown in Fig. 25 A, B, and C. Seismic velocity as a function of water saturation for porosity equal to 10 %, in partially saturated dolomite is displayed in Fig. 25A. As shown in the figure; the velocity in a high absorbing oil-saturated case ( $Q=10$ ) increases with increasing water saturation values, and it is greater than that of partially saturated gas under the same conditions. With increasing  $Q$ -values, the velocities in both oil- and gas-saturated cases were decreased. It is obvious that the velocity curves are shifted downwards on the graph, with increasing  $Q$ -values, i.e. decreasing attenuation effects. The velocities of elastic media are of lower values than those of anelastic ones and this is true for both gas and oil partially saturated cases.

The last statement may be applied for Fig. 25B and 25C, these show the characteristic velocity for both gas and oil saturated cases, in elastic media, and also after introducing attenuation parameters in calculations. In Table I, compares some calculations for the three studied rocks to show the velocities in elastic and anelastic media for both partially gas- and oil-saturated cases, with  $Q$  equal to 10, and  $S_w$  equal to 50% (mixture case). These calculations demonstrate that velocity in a massive medium decreases according to the fluid content and fluid type. The relationship between the velocity and water saturation in the presence of attenuation effects shows that seismic velocity is highly affected by the degree of fluid concentration.

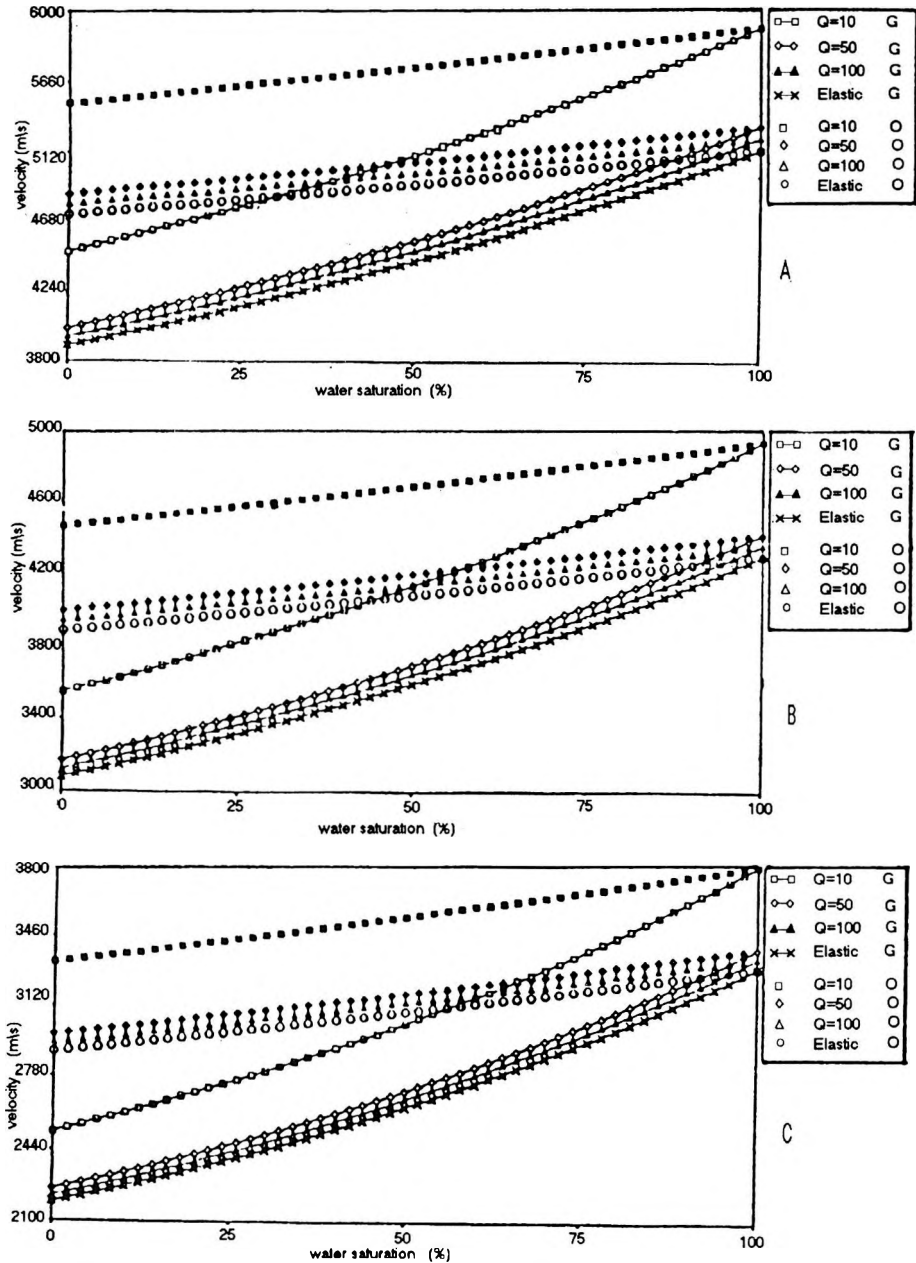


Fig. 25. Velocity and water saturation in partially gas- and oil-saturated sandstone, in both elastic and anelastic cases at Q equal to 10, 50, and 100 for porosities of (A) 10%, (B) 15%, and (C) 25%  
 25. ábra. Sebesség és víztelítettség gázzal és olajjal részlegesen telített homokkőben, rugalmas és rugalmatlan esetekre Q = 10, 50 és 100 valamint 10 % (A), 15 % (B) és 25 % (C) porozitás esetére

Rock type	Velocity (m/sec)			Porosity (%)
	massive	part. gas-sat.	part. oil-sat.	
dolomite	7000	4430.5	4912.2	10
limestone	6400	3590.4	4076.4	15
sandstone	5500	2637.1	3087.8	25

Table 1a: Comparison of seismic velocities in elastic case for partially gas- and oil-saturated rocks at  $S_w=50\%$

Ia. táblázat. A szeizmikus sebességek összehasonlítása rugalmas esetben gázzal és olajjal részlegesen telített kőzetekben  $S_w = 50\%$

Rock type	Velocity (m/sec)			Porosity (%)
	massive	part. gas-sat.	part. oil-sat.	
dolomite	7000	5093.6	5647.5	10
limestone	6400	4127.8	4686.5	15
sandstone	5500	3031.8	3549.9	25

Table 1b: Comparison of seismic velocities in anelastic case for partially gas- and oil-saturated rocks at  $Q=10$  and  $S_w=50\%$

Ib. táblázat. A szeizmikus sebességek összehasonlítása rugalmatlan esetben gázzal és olajjal részlegesen telített kőzetekben  $Q = 10$  és  $S_w = 50\%$  esetén

## 6. Field example

It was better to demonstrate synthetic seismograms for actual measured seismic traces to show the effect of the water saturation on it. Unfortunately, as a seismic time section was not available, instead of applying a measured amplitude, a computed one was used. This was done using the available petrophysical parameters. i.e, porosity and water saturation, in one of the oil fields in the Gulf of Suez in Egypt. This was Amal oil Field, which covers the area between longitudes 33.81°E to 33.88°E and latitudes 28.08°N to 28.13°N, as shown in Fig. 26. Five wells (W2, W3, W5, W7 and W9) were selected in which the sandstones of the Kareem Formation are presented. The previously calculated petrophysical parameters for the sand layers in Kareem Formation were utilized [EL HAMZY 1987]. Seismic amplitudes for both upper and lower interfaces for the sand layers in the studied wells, were computed; these are illustrated in Figs. 27A and 27B.

In order to understand the results clearly, it should be noted that these amplitudes are calculated for this sand layer under different porosity conditions and also different thicknesses, as cross plotted in Figs. 27B and 27C. It is obvious that the seismic amplitudes changed with changing water saturation: they decreased when the water saturation increased, for the lower interface at

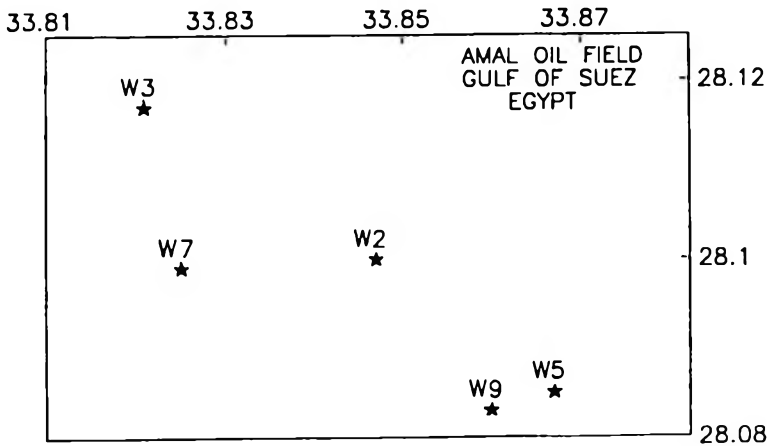


Fig. 26. Location map of Amal oil field, Gulf of Suez, Egypt  
 26. ábra. Az Amal olajmező helyszínrajza, Szuezi öböl, Egyiptom

wells 5 and 7, as shown in Fig. 27D. However, this is different for the upper interface, see Fig. 27A.

Another example is presented in Fig. 28 in which the sand layers were selected to be under similar porosity conditions within a small range of porosity values. This range is between 23% and 27%. for the present case, the seismic amplitudes are also computed for both the upper and lower interfaces of the selected layers, with different thicknesses and depths, as illustrated in Figs. 28B and 28C. However, the overlying and the underlying layers are not only shales: sometimes they are limestones, clays, or sandy shales. In general, with regard to the lower interface, minimum variation of the amplitudes was observed especially in W2, W5 and W7 (Fig 28D). This resulting amplitude variation is similar to that of the modelled curves in Fig. 23 for the water saturation range up to 40%. It is mentioned that in the studied geologic model, the thickness and the porosity values were stable throughout the computations. The upper interface shows amplitude variations with wavy nature versus water saturation due to the changes of the layer thicknesses as displayed in Fig. 28A.

## 7. Discussion and conclusion

The study deals with the effects of water content in rock pores in seismic velocity as well as gas and/or oil mixed with water. Attenuation effects are studied at the predominant frequency of the source event. A flow chart, Fig. 29, describes the processing steps needed to execute the computation operations to model a geophysical problem which could be useful,

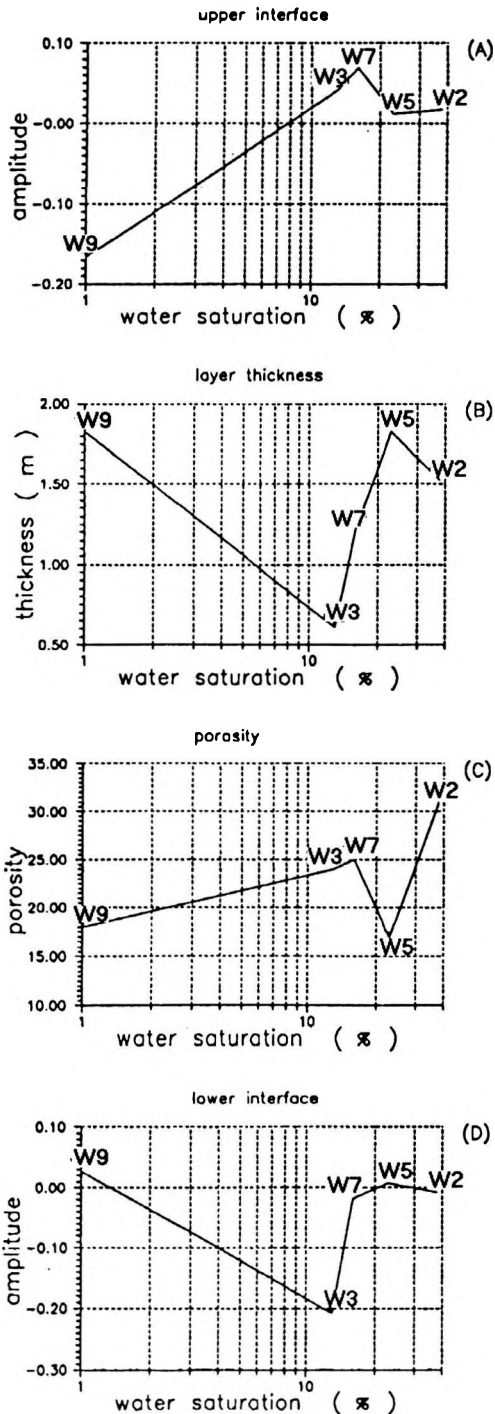


Fig. 27. Seismic amplitude variations versus water saturation for both interfaces i.e. upper (A) and lower one (D), at different porosities (C), and thicknesses (B). The layer is the same within the labelled wells

27. ábra. Szeizmikus amplitudó variációk a víztelítettség függvényében mindkét határfelületre, a felsőre (A) és az alsóra (D), különböző porozitásértékekre (C) és vastagságokra (B). A réteg a címkezett fúrássok között azonos

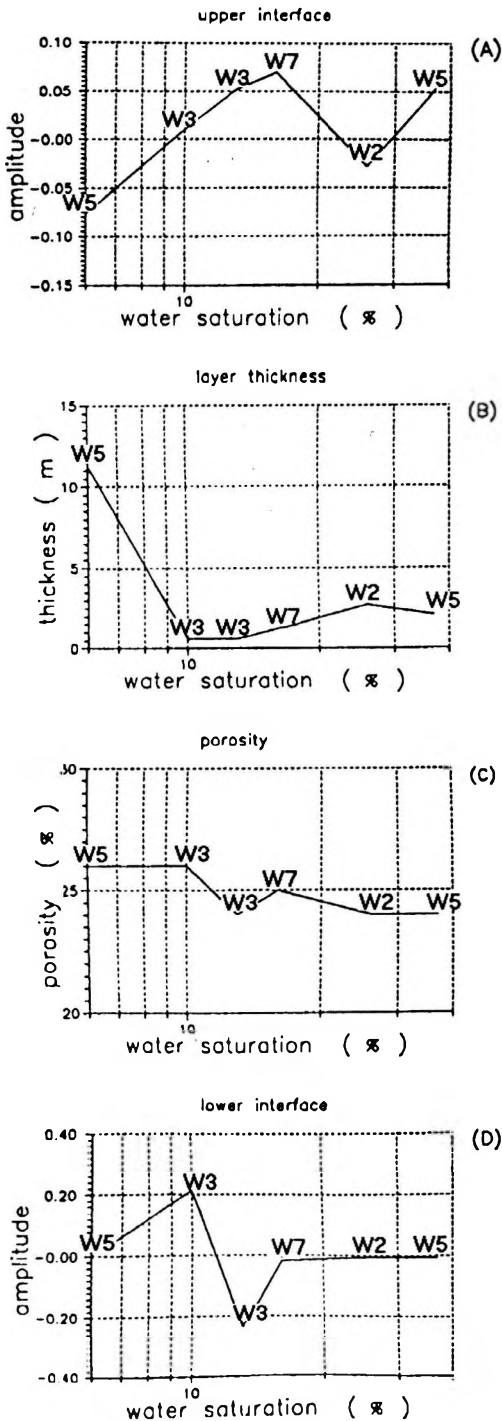


Fig. 28. Seismic amplitude variations versus water saturation for both interfaces i.e. upper (A) and lower one (D), at different thicknesses (B). This case is for different sand layers for the presented porosity range (C) within the labelled wells

28. ábra. Szeizmikus amplitudó variációk a víztelítettség függvényében mindkét határfelületre, a felsőre (A) és az alsóra (D), különböző vastagságokra (B). Ez az eset különböző homokrétegeket mutat az adott porozitás határok között (C) a címkézett fúrások között

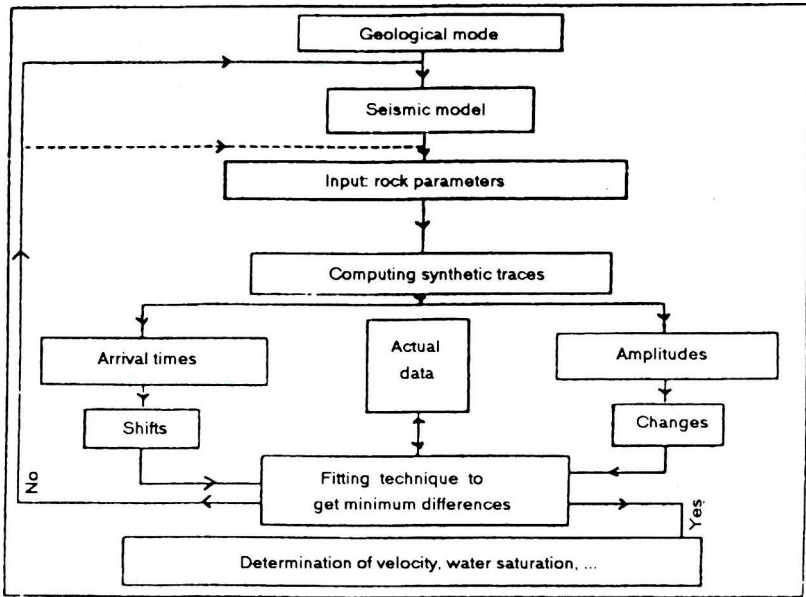


Fig. 29. Flowchart shows the processing steps that may be used to determine some geophysical parameters of a medium by seismic data

29. ábra. Egy közeg fizikai paramétereinek szeizmikus adatokból történő meghatározásához használható feldolgozási lépések blokkdiagramja

for determining the water saturation concentrations from seismic measurements.

Low water saturation causes a large decrease in seismic velocity, but higher concentration values of water decrease the relative amplitudes. A low gas saturation mixed with water causes a relatively large decrease of relative amplitude values. Low oil saturation also causes a decrease in relative seismic amplitude but lower than that of the partially gas-saturated case.

By introducing attenuation effects in the computations; seismic velocity decreases with increasing  $Q$ -values (i.e. decreasing the attenuation), in a partially saturated medium.

## REFERENCES

- ANDERSON D. L., SPETZLER H. 1970: Partial melting and the low-velocity zone. *Phys. Earth Planet. Inter.*, **4**, 1, pp. 62-64
- BIOT M. A. 1956a: Theory of propagation of elastic waves in a fluid-saturated porous solid. I. Low-frequency range. *J. Acoust. Soc. Am.*, **28**, pp. 168-178
- BIOT M. A. 1956b: Theory of propagation of elastic waves in a fluid-saturated porous solid. II. High-frequency range. *J. Acoust. Soc. Am.*, **28**, pp. 179-191

- DESAI K. P, MOORE E. J. 1967: Well log interpretation in permafrost. *Trans. Soc. Prof. Well log Anal.*
- DOMENICO S. N. 1974: Effect of water saturation on seismic reflectivity of sand reservoirs encased in shale. *Geophysics*, **39**, 6, pp. 759-769
- DUNN K. J. 1986: Acoustic attenuation in fluid-saturated porous cylinders at low frequencies. *J. Acoust. Soc. Am.*, **79**, pp. 1709-1721
- EL-HAMZY A. M. A. 1987: Well logging and geological studies for formation evaluation in Amal field area, Gulf of Suez, Egypt. Ph. D. thesis, Al Azhar University, Cairo
- ELLIOT S. E., WILEY B. F. 1975: Compressional velocities of partially saturated unconsolidated sands. *Geophysics*, **40**, 6, pp. 949-954
- KJARTANSSON E. 1979: Constant Q wave propagation and attenuation. *J. Geophys. Res.*, **84**, B9, pp. 4737-4748
- LERCHE I., D. PETROY 1986: Multiple scattering of seismic waves in fractured media: velocity and effective attenuation of the coherent components of P-waves and S-waves. *Pure Appl. Geophys.* **124**, pp. 975-1019
- HALPERN M. R., CHRISTIAN P. 1986: Steady-state response of rigid plate bearing on a liquid-saturated poroelastic halfspace. *Int. J. Earthquake Eng. Struct. Dyn.* **14**, pp. 439-454
- MAVKO G. M., NUR A. 1977: Wave attenuation in partially saturated rocks. *Geophysics*, **44**, 2, pp. 161-178
- MARSCHALL R. 1984: Some aspects of deconvolution. (preprint) CDC's Petroleum Seminar, Geneva
- NUR A. 1973: Role of pore fluids in faulting. *Trans. Phil. R. Soc. London A*, **247**, pp. 297-304
- NUR A., SIMMONS G. 1969: The effect of saturation on velocity in low porosity rocks. *Earth Planet. Sci. Lett.*, **7**, pp. 183-193
- OGUSHWITZ P. R. 1985: Applicability of Biot theory: I. low-porosity material. *J. Acoust. Soc. Am.*, **77**, pp. 429-440
- PHILIPPAPOPOULOS A. J. 1987: Waves in a partially saturated layered half-space: analytic formulation. *Bull. Seism. Soc. Am.*, **77**, 5, pp. 1838-1853
- PHILIPPAPOPOULOS A. J. 1989: Axisymmetric vibration of disk resting on saturated layered half-space. *J. Eng. Mech.*, **115**, pp. 2301-2322
- RANDALL M. J. 1976: Attenuative dispersion and frequency shifts of the earth's free oscillations. *Phys. Earth Planet. Inter.* **12**, 1, pp. 1-4
- SHERIFF R. E. 1975: Factors affecting seismic amplitudes. *Geophys. Prosp.*, **23**, 1, pp. 125-138
- STOLL R. 1974: Acoustic waves in saturated media. *In*: L. Hampton (ed), *Physics of sound in marine sediments*: Plenum Press, New York
- WALSH J. B. 1969: New analysis of attenuation in partially melted rocks. *J. Geophys. Res.*, **74**, pp. 4333-4337
- WHITE J. E. 1975: Computed seismic speeds and attenuation in rocks with partial gas saturation. *Geophysics*, **40**, 2, pp. 224-232
- WYLLIE M. R. J., GARDNER G. H. F., GREGORY A. R. 1962: Studies of elastic wave attenuation in porous media. *Geophysics*, **26**, 4, pp. 569-589
- WYLLIE M. R. J., GARDNER G. H. F., GREGORY A. R. 1963: Discussion. *Geophysics*, **28**, 6, p. 1074

## SZEIZMIKUS JEL-ANALÍZIS FOLYADÉKKAL RÉSZLEGESEN TELÍTETT KÖZEGBEN

Adel A. A. OTHMAN

A folyadék-telítettségnek a szeizmikus sebességre, és következésképpen a szeizmikus amplitúdókra gyakorolt hatásának tanulmányozására földtani modellt javasol. Bevezeti a parciális gáz-telítettség és a parciális olajtelítettség fogalmát. Szintetikus szeizmogramokat számol a kívánt hatások bemutatására. Csillapítást vezet be és kiszámolja ennek hatását.

A számítások megerősítették, hogy a pórusvíz nagyobb koncentrációja csökkenti a szeizmikus hullámok amplitúdóját, valamint, hogy a vízzel keveredett kis gáztelítettség a relatív amplitúdó viszonylag nagymértékű csökkenését eredményezi — és ez nagyobb, mint amit az olajporusok bevezetése okoz.

## FLOW OF THE TIBETAN PLATEAU AND TECTONICS ALONG THE BURMESE ARC

V. P. SINGH\* and D. SHANKER\*

The seismicity of northeast India and its surroundings (18 °N to 32 °N and 84 °E to 100 °E) is very complex. It includes the Himalayan thrust, the Burmese region and a small portion of the Tibetan plateau. It shows widespread distribution of earthquakes and constitutes one of the important tectonic features of the world. It has been reported that the northeast drift rate of the Indian plate and southeast flow of the Tibetan plateau are of the same order, i.e.  $18 \pm 7$  mm/year. Thus the effect of flow of the Tibetan plateau on seismicity distribution of the meeting zone of the Indian and Burmese plates and the Tibetan plateau would be greater than the Indian and Burmese plates because of its high crustal thickness. Normally shallow earthquakes are observed all over the region except the Burmese arc, where intermediate earthquakes occur to a depth of 200 km. The width of the arcuate seismicity is maximum around 24 °N and reduces on either sides terminating at 21 °N and 27 °N. The fault plane solutions suggest that the compressive stresses also act along the strike of the arc; extensional stresses are also observed. In the paper a model is presented to explain seismicity, focal depth, frequency and stress distribution in the arc zone taking into account the southeast flow of the Tibetan plateau.

**Keywords:** tectonics, seismicity, drift rate, stress distribution

### 1. Introduction

The northeast region of India is very complex from the geological, geophysical and seismological points of view. The tectonic features of the region comprise the Himalayan thrust, the Burmese region, and a small portion of the Tibetan plateau. The nature of the tectonic deformations has been studied by several authors: the Himalayas by FITCH [1970], VERMA et al. [1977], VERMA et al. [1980]; the Tibetan region by MOLNÁR, TAPPONIER [1978], MOLNÁR et al. [1987], VERMA, REDDY [1988]; and the Burmese region by

\* Department of Geophysics, Faculty of Science, Banaras Hindu University,  
Varanasi-221005, India  
Manuscript received (revised version): 27 April, 1993

RASTOGI et al. [1973], VERMA, KUMAR [1987]. The clockwise rotation of the Burmese region with the westward movement towards the Indian plate was reported by HAMILTON [1979] and CURRAY et al. [1982]. The above studies reveal drifting of the Indian plate towards the northeast, the extension of the southern Tibetan region towards the northwest, and the southeast, and the Burmese region towards the west.

The considered region shows widely distributed large earthquakes. Intermediate focal depth earthquakes are observed along the Burmese arc, which has been reported to be due to subduction of the Indian plate towards the Burmese region. However the characteristics of the seismicity distribution along the arc [TENG et al. 1987] suggest that the northeast drifting of the Indian plate would not be able to produce the existing nature of the subduction zone. MOLNÁR et al. [1987] reported the northeast drift rate of the Indian plate and southeast flow of the Tibetan plateau to be of the same order, i.e.  $18 \pm 7$  mm/year. Thus the effect of southeast flow of the Tibetan plateau on the seismicity distribution pattern on the region would be of the same order as the northeast drifting of the Indian plate.

The present study discusses a plausible model that would explain the distribution and concentration of earthquakes and the direction of tectonic stresses along the arc-shaped zone.

## 2. Seismicity data

The earthquake catalogues prepared by the National Geophysical Data Centre (NGDC), Boulder, Colorado, have been used so as to have uniformity in the data. As large earthquakes are recorded all over the world, the estimation of their hypocentres may be taken to be reliable. For the present study the data have been considered since 1912 to 1977 with magnitude  $M \geq 6.0$ . The seismicity distribution map prepared by TENG et al. [1987] with body wave magnitude  $m_b \geq 4.0$  for the period 1961 to 1980 has also been incorporated in the present study. *P*-wave first motion data have been taken from the Bulletin of the International Seismological Centre (ISC) for the selected events of the period 1969 to 1984. The bulletin reports first motions, compressions, and dilatations for a large number of observations (short and long period records).

## 3. Tectonic characteristics

The considered region has complex geological formations. It includes regional folding mainly striking north-south in the Burmese region, almost east-west in the Himalayas, as well as the Siling fold belt and Kunlun faults of the Tibetan plateau. The tectonic pattern of the region is highly complex.

YANSHIN [1966] and ZHANG [1983] published a tectonic map of China and the Tibetan plateau showing the lineaments and faults (*Fig. 1*). At present this plateau is under violent tectonic movement. An arcuate structural belt convex towards the east that strikes northeast is the principal characteristic of the structure of the plateau. The Himalayan regions are associated with intensive folding and thrusting [KROPOTKIN 1969, LOMNITZ 1974].

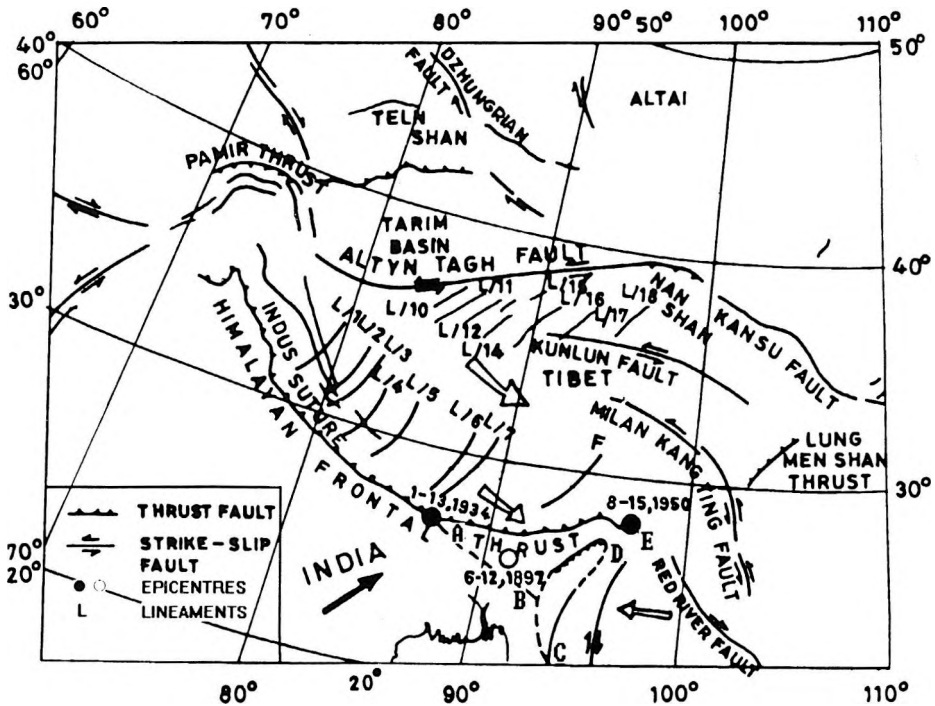


*Fig. 1.* Map showing recent tectonic features of Asia. Lineaments, faults and epicentres of the three major earthquakes of 1897, 1934, and 1950 are indicated. The demarcated area (A-B-C-D-E) is under the influence of southeast flow of the Tibetan plateau

*1. ábra.* Ázsia jelenlegi tektonikai jellegzetességeinek térképe. Az 1897, 1934 és 1950-es három fő földrengés lineamentjeit, vetőit és epicentrumait jelöltük be. A körülhatárolt terület (A-B-C-D-E) a Tibeti-fennsík délkelet irányú eltolódásának hatása alatt áll

#### 4. Focal mechanisms and orientation of stress

Tectonic motions have been inferred through fault plane solutions. Eleven focal mechanisms of earthquakes of the Burmese arc zone have been considered. Of these, six are new mechanisms whereas five have previously been reported. The focal mechanism solutions of the considered six events show different patterns along the strike of the arc zone. Mechanisms 1 and 4 show normal; 3, 5 and 6 indicate thrust; and 2 demonstrate strike slip faultings. The locations of epicentres of the considered earthquakes for the focal mechanism solutions and their ISC parameters are given in *Fig. 2* and *Table I*, respectively. *Table II* shows the orientation of the poles, and B, P, and T axes.

Event	Date	Time of origin (h:min:s)	Epicentre		Focal depth [km]	Magnitude (M)	Re-mark
			Lat [°N]	Long [°E]			
1	28 Apr. 1969	12:50:15.2	25.9	95.3	50	5.2	*
2	14 Oct. 1971	12:55:23.3	23.1	95.8	63	5.2	*
3	29 Dec. 1971	22:27:02.0	25.1	94.6	33	5.5	*
4	13 Dec. 1975	22:35:44.2	23.6	94.3	63	5.2	*
5	13 Oct. 1977	11:32:09.3	23.5	95.4	61	5.2	*
6	05 Marc. 1984	21:26:42.5	24.5	94.6	69	5.2	*
A	17 Oct. 1969	01:25:12.4	23.1	94.7	124	6.0	**
B	29 July 1970	10:16:19.3	26.0	95.4	59	6.5	**
C	08 July 1975	03:03:11.6	26.5	96.4	33	5.2	**
D	22 Jan. 1964	15:18:46.4	22.3	93.6	60	6.3	***
E	15 Dec. 1965	04:43:45.9	22.0	94.5	109	5.2	***

*Table I.* Parameters of earthquakes of arc-shaped zone of northeast India. \* denotes the present study, \*\* by LE DAIN et al. [1984] and \*\*\* by MUKHOPADHYAY, DASGUPTA [1988]

*I. táblázat.* Észak India ív-szerkezetű zónájában előfordult földrengések paraméterei. Jelölések: \* — jelen tanulmány, \*\* — LE DAIN et al. [1984] és \*\*\* — MUKHOPADHYAY, DASGUPTA [1988] nyomán

Event	Plane 'a'			Plane 'b'			B-axis		P-axis		T-axis		Remarks
	Dip direction [°]	Dip [°]	Strike [°]	Dip direction [°]	Dip [°]	Strike [°]	Trend [°]	Plunge [°]	Trend [°]	Plunge [°]	Trend [°]	Plunge [°]	
1	326	03	N56E	146	86	N56E	056	00	326	54	146	48	*
2	102	60	N14E	358	68	EW	062	52	228	25	138	04	*
3	210	70	N60W	030	18	N60W	302	00	210	26	030	64	*
4	270	16	NS	090	74	NS	000	00	270	62	090	29	*
5	352	56	N82E	214	43	N52W	280	24	013	06	116	64	*
6	356	62	N86E	176	28	N86E	086	00	355	16	175	72	*
A	000	72	EW	180	14	EW	090	00	000	30	180	60	**
B	356	52	N86E	088	76	NS	015	57	226	26	129	16	**
C	318	38	N52E	208	60	N62W	280	37	178	16	070	48	**
D	104	74	N14E	344	30	N74E	022	24	254	54	123	25	***
E	064	68	N26W	234	22	N34W	152	03	254	66	060	23	***

Table II. Focal mechanism solutions of the considered events of the Burmese arc. \* denotes the present study, \*\* and \*\*\* by LE DAIN et al. [1984] and MUKHOPADHYAY, DASGUPTA [1988], respectively

II. táblázat. A Burmai-ív vizsgált jelenségeinek fókuszmechanizmus megoldásai. Jelölések: \* — jelen tanulmány, \*\* — LE DAIN et al. [1984] és \*\*\* — MUKHOPADHYAY, DASGUPTA [1988] nyomán

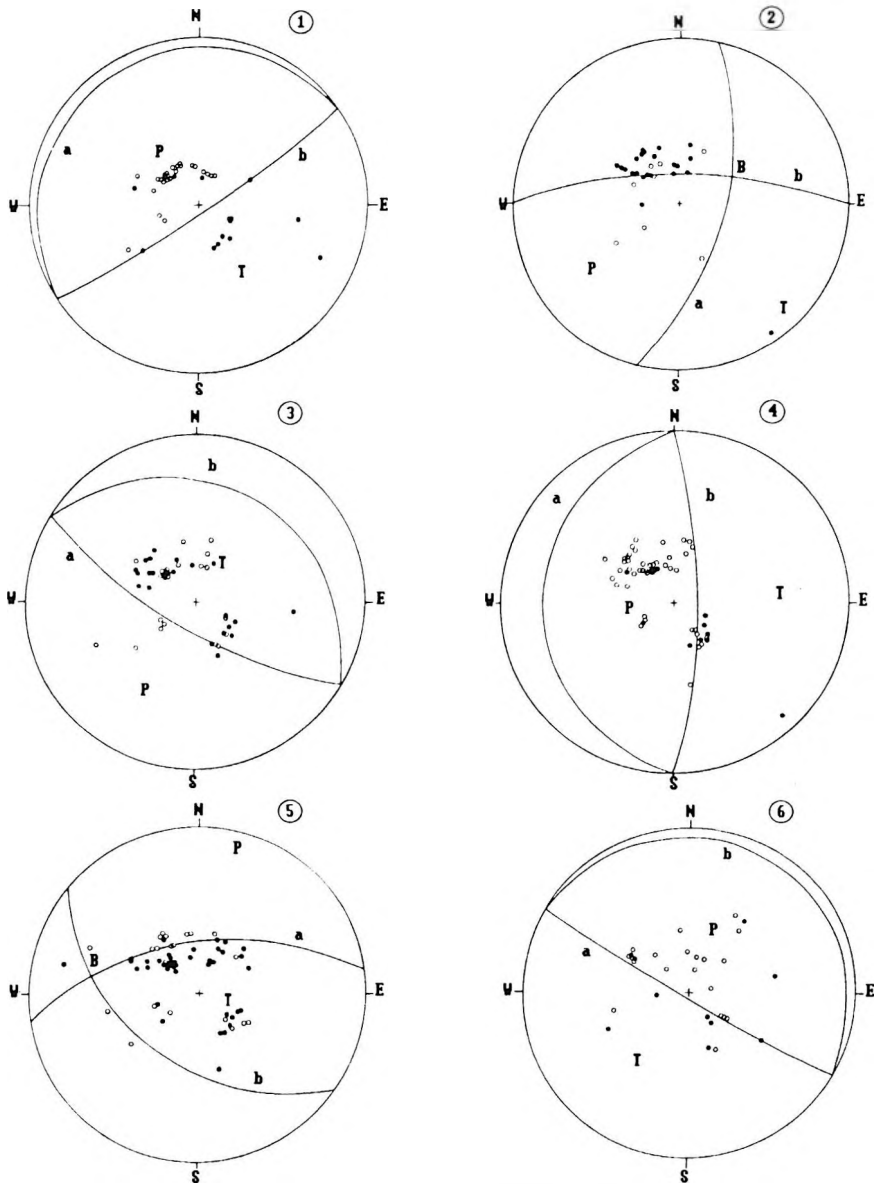


Fig. 2. Lower hemisphere equal area projection of fault plane solutions; open and solid circles indicate P-wave dilations and compressions, respectively, 'a' and 'b' are fault and auxiliary planes, P and T correspond to the axis of compression and tension, B is the null point

2. ábra. A vetősík megoldásával azonos területű vetületek az alsó féltekén; üres és telített körök jelzik a P-hullám megnyúlásokat illetve kompressziókat, 'a' és 'b' a vető és segédsíkok; P és T megfelelnek a kompressziós és tenziós tengelyeknek; B a nulla pont

### 5. Seismic characteristics of the region

The seismicity data for the region (15 °N to 35 °N and 80 °E to 100 °E) for the period 1961 to 1980 are shown in Fig 3. It includes all the events of  $m_b \geq 4.0$ . The seismicity distribution of large earthquakes ( $M \geq 6.0$ ) for the

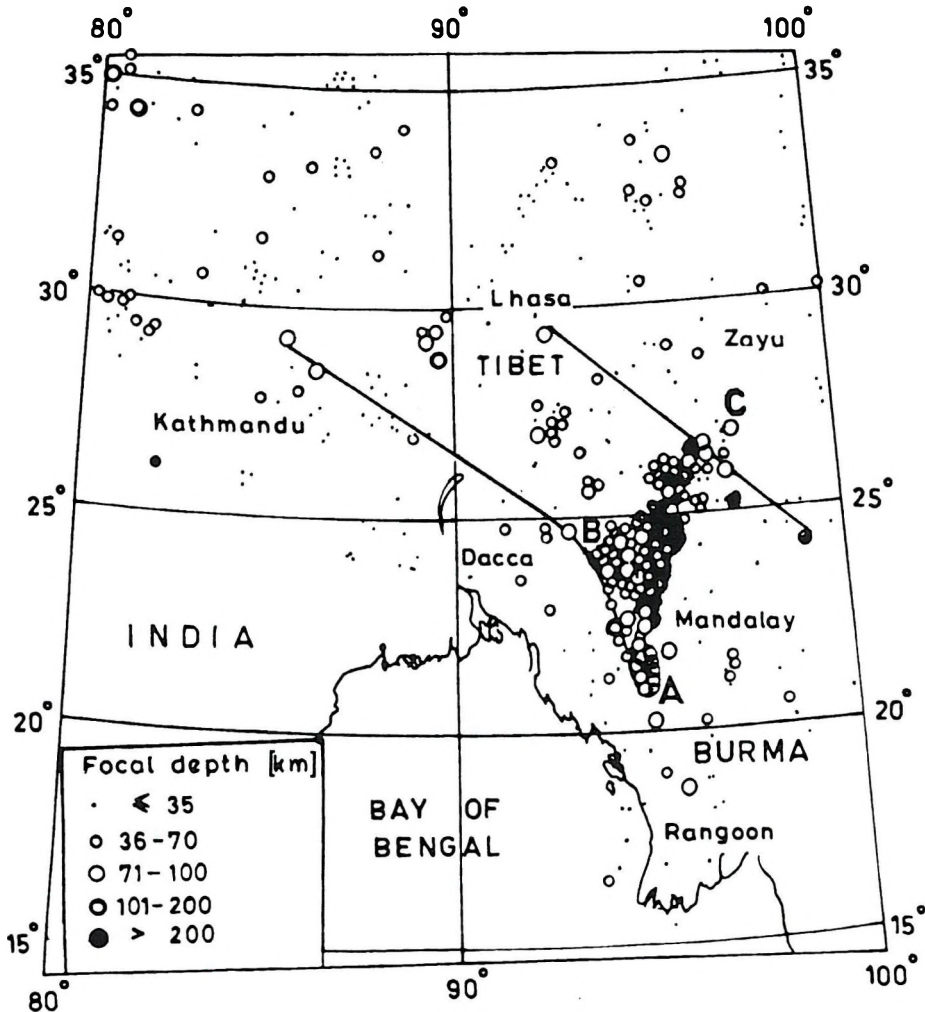


Fig. 3. Seismicity distribution of northeast India and its surroundings for the period 1961-1980 [TENG et al. 1987]. Intermediate focal depth earthquake zone is also demarcated by the two NW-SE trending lines

3. ábra. Északkelet India és környékének szeizmicitás eloszlása az 1961-1980-as időszakra [TENG et al. 1987]. A közepes fókuszmélységű földrengészónát is bejelöltük két ÉNY-DK irányú vonallal

period 1912 to 1977 is shown in Fig. 4. Intermediate focal depth earthquakes are also shown. The above figures reveal the seismic activity to be very high along the Burmese arc. The southern portion of the plateau is affected by widely distributed large earthquakes. Both the above figures reveal a seismically active arc-shaped zone showing the width of seismicity to be about 100 km at 24 °N. The width of seismicity decreases on either side terminating at 21 °N and 27 °N. The seismic belts AB and BC strike, respectively, north-south and northeast-southwest. The high seismic activity around 24 °N may be realized due to the fact that out of thirteen intermediate earthquakes, six have been occurred in a very limited area around 24 °N. The deepest earthquake to the east of Arakan-Yoma mountain is 250 km [VERMA et al. 1978]. Three intermediate earthquakes of magnitude  $M \geq 6.0$  have occurred outside the Burmese arc. TENG et al. [1987] and KAYAL [1987] reported a number of intermediate focal depth earthquakes of smaller magnitude in the southern Tibetan plateau and Assam region. The demarcation of these earthquakes is shown in Fig. 3 striking northwest-southeast. Of the considered earthquakes three show thrust, two normal faulting, and one strike-slip faulting.

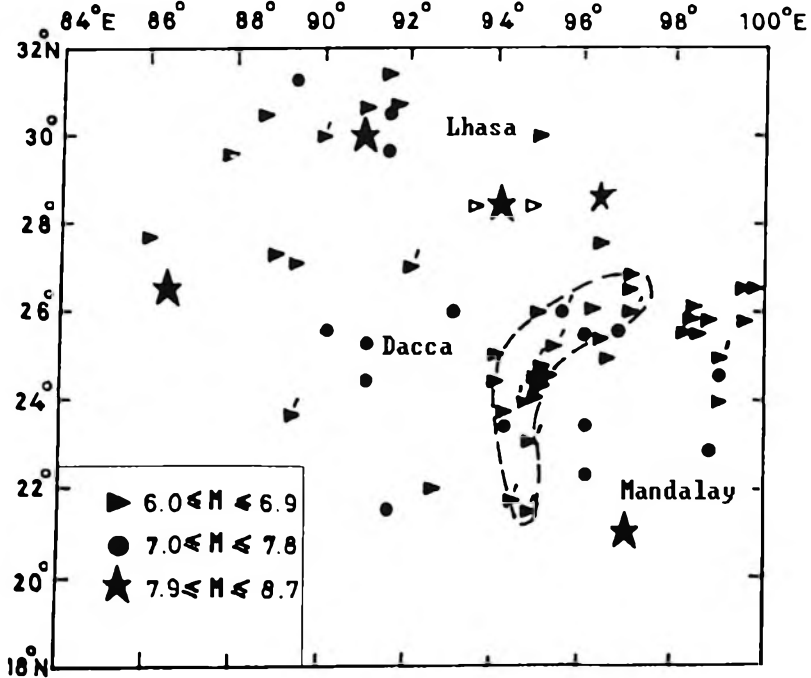


Fig. 4. The spatial distribution of large earthquakes  $M \geq 6.0$  for the period 1912–1977. Dashed symbol shows the earthquakes with focal depth  $\geq 70$  km. Note that intermediate earthquakes are observed maximum around 24 °N which reduced in space and time on either side along the arc

4. ábra. Az  $M \geq 6.0$  nagy földrengések térbeli eloszlása az 1912–1977-es periódusra. A szaggatott jelölés a 70 km-nél nagyobb fókuszmélységű földrengéseket mutatja. Megjegyezzük, hogy a közepes méretű földrengéseket maximum 24 °E körül észlelték, melyek mérete térben és időben csökkent az ív mindkét oldalán

Mechanisms 1 and 4, which are shallow events, show an extensional character of crustal movement. The nature of mechanisms for three shallow shocks (events 3, 5 and 6) of arc-shaped zone shows the peculiar nature of thrust faulting. The stresses are shallow dipping and oriented perpendicular to the strike of the seismic belt. Mechanism 2 shows strike-slip faulting. The directions of forces for these cases are shown in Fig. 5.

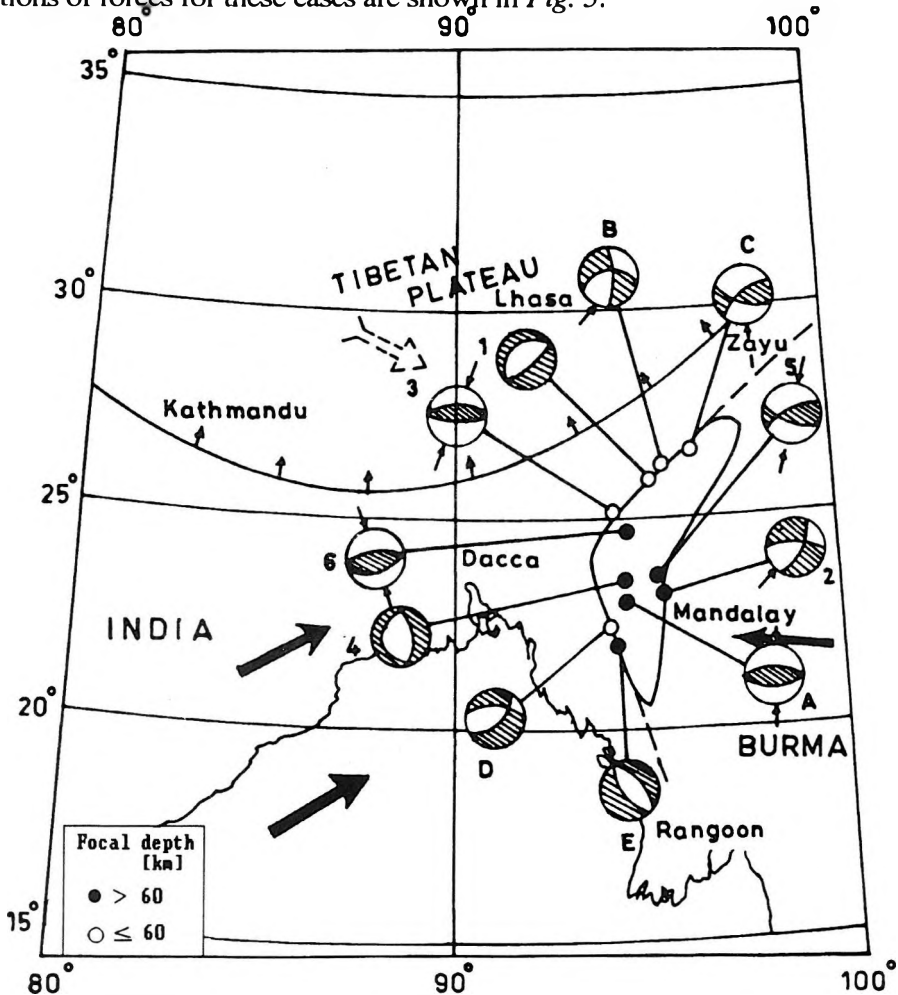


Fig. 5. A simplified map showing the direction of compressive forces. Big arrows indicate the direction of flow/drift of the surroundings. Direction of compressive stresses derived from fault plane solution and focal mechanisms for the considered earthquakes are also shown

5. ábra. A kompressziós erők irányát mutató egyszerűsített térkép. A nagy nyilak jelölik a környezet eltolódás/elfordulás irányait. A kompressziós feszültségek irányát a vető sík megoldásából vezettük le. A vizsgált földrengések fókuszmechanizmusait is bemutatjuk

The general nature of seismicity and stresses in northeast India does not show a systematic pattern because of the converging nature of the surroundings. The northeastern Indian region experienced three large earthquakes of  $M \geq 8.4$  as shown in Fig. 1. The generation of a large earthquake requires high strain rate accumulation. SINGH, SINGH [1987] studied the strain rate in the Himalayas and the nearby region. These authors reported the strain rate deformation to be maximum for the region. This suggests that the flow of the Tibetan plateau might have developed significant strain for the occurrences of such big earthquakes of northeast India, i.e. Shillong earthquake of 1897, Bihar earthquake of 1934, and Assam earthquake of 1950. The epicentre of the Shillong earthquake is not at the northern trench of the Indian plate.

TENG et al. [1987] have pointed out that an arcuate structure is formed only in the crustal layer. However, sixty-six years of seismicity data of large earthquakes indicate the arcuate structure to extend to about 150 km. The distribution of seismicity along the Burmese arc shows maximum width at 24 °N. The seismicity along AB and BC strikes north-south and northeast-southwest, respectively. The northeast drifting of the Indian plate cannot be the cause of the subduction of zone BC towards the southeast.

The fault plane solution of intermediate focal depth micro-earthquake studies for the Shillong plateau shows a northeast-southwest striking fault dipping towards the southeast [KAYAL 1987]. This cannot be explained by northeast drifting of the Indian plate and hence supports the seismic activity as being due to the southeast flow of the Tibetan plateau.

## 6. Earthquakes and tectonics of the arc

The earthquake distribution of the arc is of peculiar nature. The frequency and average focal depth distribution for the earthquakes of the zone are shown in Fig. 6a-b. Similar observations are also taken for the average focal depth of the region. The tectonic nature of the zone shows peculiar character [VERMA, KUMAR 1987]. The nature of the faults and direction of stresses show different orientations. For shallow earthquakes, the compressive stresses are characterized by shallow dipping and are directed towards the Burmese region [FITCH 1970, RASTOGI et al. 1973]. Here fault plane solutions for eleven events have been considered, including six new mechanisms. Fault plane solutions for five events have been taken from MUKHOPADHYAY, DASGUPTA [1988] and LE DAIN et al. [1984]. Of the eleven solutions four show normal, four thrust, and three strike-slip faulting. The above solution reveal both extensional and compressive forces, focal mechanisms 1, 4, D and E reveal normal faulting which may be interpreted as bending of the lithosphere into the upper mantle due to the southeast flow of the Tibetan plateau. This also reflects that the sinking of the dipping lithosphere in the arc is still continuing. Events 3, 5, 6 and A show thrust faulting. In these cases the faultings are almost perpendicular

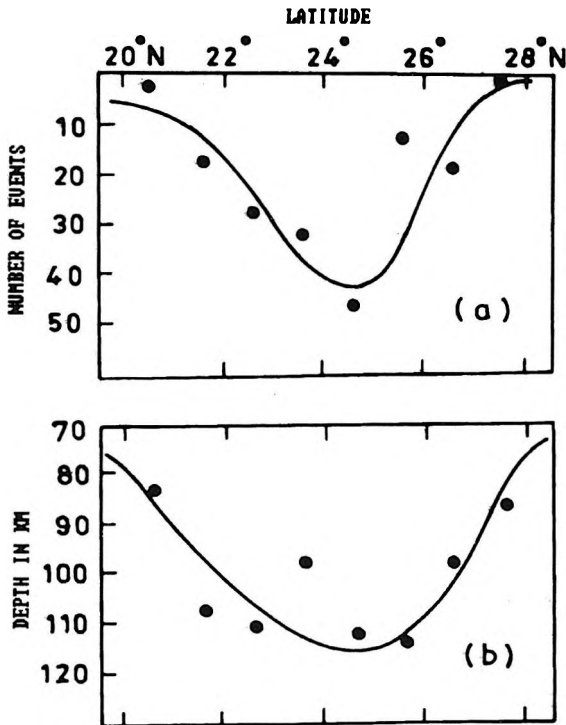


Fig. 6. a—Variation of frequency with latitude for the region 20 °N to 28 °N and 92 °E to 97 °E, based on 25-years (1960–1984) seismicity data as reported by the National Geophysical Data Centre. The considered region includes an arc-shaped zone; b—Average focal depth variation with latitude for the considered zone

6. ábra. a — A gyakoriság változásai a földrajzi szélességgel a 20 °É – 28 °É és a 92 °K és 97 °K tartományban, a 25 éves (1960–1994) szeizmicitás adatok alapján, a Nemzeti Geofizikai adatközpont jelentéseiből. A vizsgált terület egy ív-alakú zónát is tartalmaz; b — Átlagos fókuszmélység változás a földrajzi szélességgel a vizsgált zónában

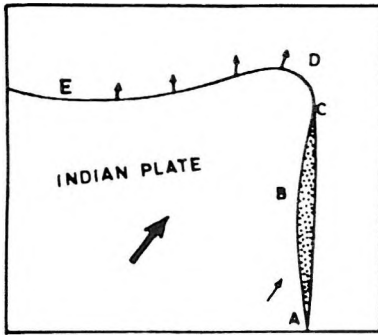
to the strike of the seismically active zone. The direction of stresses acting in thrust and strike-slip faultings (2, B and C) is along the strike of the arc.

## 7. Discussion

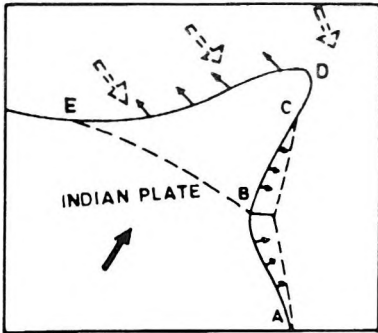
Several scientists have studied the seismicity of the Burmese arc and its adjoining areas [SANTO 1969, LE DAIN et al. 1984, MUKHOPADHYAY, DASGUPTA 1988]. The Benioff zone showing intermediate earthquakes along the Burmese region has been reported to strike north–south (from 21 °N to 24 °N) and northeast–southwest (from 24 °N to 27 °N). The tectonics and seismicity of the Burmese arc have been explained by northeast drifting of the Indian plate. The present nature of the arc-shaped zone cannot be explained by northeast drifting of the Indian plate as it cannot explain arcuate subduction. At the same time the distribution of intermediate earthquakes, the 100 km width of seismicity around 24 °N which reduces on either side, the earthquake frequency, the focal depth distribution, and the nature of forces acting along the arc cannot be explained by collision of the Indian and Burmese plates. The above observations may be explained in the light of bending of the eastern plate margin due to the southeast flow of the Tibetan plateau.

MOLNÁR et al. [1981] and MOLNÁR, CHEN [1983] revealed the extensional tectonics of the Tibetan plateau. MOLNÁR, TAPPONNIER [1975] showed the southeast-south flow of the block along the Kang-Ting fault. MOLNÁR et al. [1987] reported the drift rate of the Indian plate and the slip rate of the plateau to be of the same order. The crustal thickness of the Tibetan plateau, and the Indian and Burmese plates are, respectively, 60–70 km, 35–45 km and 30–35 km [SHIH et al. 1979]. The Tibetan plateau is very large in comparison to northeast India (Fig. 3), therefore its southeast extension with the rate of  $18 \pm 7$  mm/year [MOLNÁR et al. 1987] would produce considerable effect in the seismicity pattern of the region. As the subduction is not observed along the plateau-Himalayas boundary, it would push north-east India (e.g. events EDB) and would make it rotate clockwise causing the bending of the eastern margin at B down to the upper mantle. The lateral movement of the Shillong plateau along the Dauki fault was reported by EVANS [1964] to form a gap — known as the Garo-Raj Mahal gap.

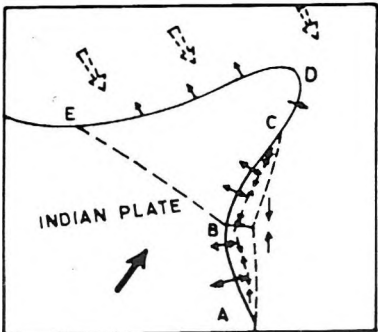
A schematic diagram explaining the distribution of seismic activity and the stress in the arc zone is shown in Fig. 7a–c. Figure 7a shows the northern and eastern boundaries of the zone, the direction of movement of the Indian plate, and the southeast flow of the Tibetan plateau. Owing to the southeast flow of the 70 km thick Tibetan plateau, boundary E-D would become concave towards the Indian plate. It would push the E-D-B zone (rotating clockwise) giving rise to the arc-shape at the eastern boundary (Fig. 7b). In doing so the zone of the eastern boundary, i.e. A-B-C-A, would be compressed and buckle down to the upper mantle showing strike of zone B-C along northeast-southwest. Bending would cause the maximum width of seismicity to take place at B with decreasing trend on either sides. Zone A-B is virtually undisturbed whereas C has shifted from southeast to the present position changing the strike of B-C from north-south to northeast-southwest. Since the drifting of the Indian plate and extension of the plateau have been continuing throughout the geologic past, the subduction of zone A-C would take place showing maximum frequency and average focal depth around B. Bending would generate compressive stress along the strike of the seismicity zone A-B and B-C. The stresses thus developed may be responsible for thrust faulting perpendicular to the strike of the seismic zone and strike-slip faultings causing right-lateral motion (solutions 2, 3, 5, 6, A, B and C; VERMA, KUMAR [1987]). The drifting of the Burma plate towards the west has also played a role in the development of the folded mountain chain of the arc zone. Though the tectonic nature and seismicity distribution are very complex and are the results of the converging pattern of the surrounding plates, the nature of orientation of subduction, frequency and average focal depth distribution and stress acting in the arc are due to the extension of the Tibetan plateau towards the southeast. The present study thus offers a new means of understanding the nature of seismicity and the tectonic pattern in the arc zone.



(a)



(b)



(c)

Fig. 7. Proposed model for the development of the Burmese arc zone. (a) demonstrates the stresses acting at the northern boundary of the Indian plate; (b) exhibits the southeast flow of the Tibetan plateau and its effect on the eastern boundary of the Indian plate; (c) illustrates the direction of stress, distribution of seismicity in the arc zone

7. ábra. A Burmai-ív kialakulására javasolt modell (a) bemutatja az Indiai-lemez északi határán működő feszültségeket; (b) a Tibeti-fennsík délkeleti áramlását, és annak hatását az Indiai-lemez keleti határára; (c) a feszültség irányait és a szeizmicitás eloszlását az ívelt zónában

## 8. Conclusions

The following conclusions have been drawn:

1. The compressive stresses acting along the strike of the Burmese arc are the result of the pushing of the northeast India region by the southeast flow of the Tibetan plateau.
2. Normal faultings are also observed in the arcuate zone, which suggests that subduction of the lithosphere is still continuing.

3. The intermediate focal depth earthquakes and the present shape of the seismically active arc zone are the result of the southeast flow of the Tibetan plateau. This flow is also responsible for the frequency and focal depth distribution of the events.

### Acknowledgements

The financial support provided by CSIR (Council of Scientific and Industrial Research), New Delhi is gratefully acknowledged.

### REFERENCES

- Bulletin of the International Seismological Centre. 1969-1984
- CURRAY J. R., EMMEL F. J., MOORE D. G., RAITT R. W. 1982: Structure, tectonics and geological history of the northeastern Indian Ocean. *In*: NAIRN A. E. M., STEHLI F. G. (eds.) *The Ocean Basins and Margins* 6, pp. 399-450, Plenum, New-York
- EVANS P. 1964: The tectonic framework of Assam. *J. Geol. Soc. India* 5, pp. 80-86
- FITCH T. J. 1970: Earthquake mechanisms in the Himalayan, Burmese and Andaman regions and continental tectonics in Central Asia. *J. Geophys. Res.* 75, 14, pp. 2699-2709
- HAMILTON W. 1979: Tectonics of the Indonesian region. *U. S. Geol. Surv. Prof. Pap.* 1078, 345 p.
- KAYAL J. R. 1987: Microseismicity and source mechanism study: Shillong plateau, northeast India. *Bull. Seismol. Soc. Am.* 77, 1, pp. 184-194
- KROPOTKIN P. N. 1969: Problem of continents drifting (mobilism). (in Russian) *Izv. Acad. Nauk. SSSR, ser. Fiz. Zemli* 3, pp. 3-19
- LE DAIN A. Y., TAPPONNIER P., MOLNÁR P. 1984: Active faulting and tectonics of Burma and surrounding regions. *J. Geoph. Res.* 89, B1, pp. 453-472
- LOMNITZ C. 1974: Global tectonics and earthquake risk. *In*: *Developments in Geotectonics* 5, Elsevier, Amsterdam-London-New-York
- MOLNÁR P., TAPPONNIER P. 1975: Cenozoic tectonics of Asia: Effects of a continental collision. *Science* 189, 4201, pp. 419-426
- MOLNÁR P., TAPPONNIER P. 1978: Active tectonics of Tibet. *J. Geophys. Res.* 83, B11, pp. 5361-5375
- MOLNÁR P., CHEN W.-P. 1983: Focal depths and fault plane solutions of earthquakes under the Tibetan plateau. *J. Geophys. Res.* 88, B2, pp. 1180-1196
- MOLNÁR P., TAPPONNIER P., CHEN W.-P. 1981: External tectonics in Central and Eastern Asia, a brief summary. *Phil. Trans. Roy. Soc. London, ser. A*, 300, pp. 403-406
- MOLNÁR P., BURCHFIELD, KUNANGYI C. B., LIANG Z. Z. 1987: Geomorphic evidence for active faulting in the Altyn Tagh and Northern Tibet and quantitative estimates of its contribution to the convergence of India and Eurasia. *Geology* 15, pp. 249-253
- MUKHOPADHYAY M., DASGUPTA S. 1988: Deep structure and tectonics of the Burmese arc: Constraints from earthquake and gravity data. *Tectonophysics* 149, 3/4, pp. 299-322
- RASTOGI B. K., SINGH J., VERMA R. K. 1973: Earthquake mechanisms and tectonics in the Assam-Burmese region. *Tectonophysics* 18, 3/4, pp. 355-366

- SANTO T. 1969: On the characteristic seismicity in south Asia from Hindukush to Burma. *Bull. Int. Inst. Seismol. Earthq. Eng.* **6**, pp. 81-95
- SHIH C.-L., WEN-LIN H., JIA-QUAN Y., SU-YUN W., CHIH-KANG W. 1979: On recent tectonics of China and its vicinity. *In: VOGEL (ed.) Terrestrial and Space Techniques in Earthquake Prediction Research.* pp. 549-566, F. Vieweg and S. Braunschweig (publisher)
- SINGH V. P., SINGH J. 1987: Precursory swarm and its application for long range earthquake forecasting in Taiwan region. *Proc. Indian Acad. Sci. (Earth Planet Sci.)* **96**, pp. 15-23
- TENG J.W., WEI S.Y., SUN K.Z., XUE C.S. 1987: The characteristics of the seismic activity in the Qinghai-Xizang (Tibet) Plateau of China. *Tectonophysics* **134**, 1-3, pp. 129-144
- VERMA R. K., KRISHNA KUMAR G. V. R. 1987: Seismicity and the nature of plate movement along the Himalayan arc, Northeast India and Arakan-Yoma: a review. *Tectonophysics* **134**, 1-3, pp. 153-175
- VERMA R. K., REDDY Y. S. K. 1988: Seismicity, focal mechanisms and their correlation with the geological/tectonic history of the Tibetan plateau. *Tectonophysics* **156**, 1/2, pp. 107-131
- VERMA R. K., MUKHOPADHYAY M., ROY B. N. 1977: Seismotectonics of the Himalaya, and the continental plate convergence. *Tectonophysics* **42**, 2-4, pp. 319-335
- VERMA R. K., MUKHOPADHYAY M., BHUIN N. C. 1978: Seismicity, gravity and tectonics in Andaman Sea. *J. Phys. Earth* **26** (suppl.), pp. 5233-5248
- VERMA R. K., MUKHOPADHYAY M., NAG A. K. 1980: Seismicity and tectonics in south China and Burma. *Tectonophysics* **64**, 1/2, pp. 85-96
- YANSHIN A. L. 1966: Tectonic map of Eurasia. *Geol. Inst. Acad. Sci. USSR, Moscow*
- ZHANG W.-Y. 1983: The marine and continental tectonic map of China and its environs. scale 1:5 000 000. *Sci. Press, Beijing*

## A TIBETI-FENNISÍK ELTOLÓDÁSA ÉS TEKTONIKÁJA A BURMAI-ÍV MENTÉN

V. P. SINGH és D. SHANKER

Északkelet-India és környékének (18°É és 84°K-tól 100°K-ig) szeizmicitása nagyon összetett. Magában foglalja a himalájai áttolódást, a Burmai-régiót és a Tibeti-fennsík kisebb hányadát. A földrengések nagymértékű szóródását mutatja és a föld egyik legfontosabb tektonikai jellegzetességét alkotja. Beszámoltak arról, hogy az Indiai-lemez északkeleti eltolódási sebessége és a Tibeti-fennsík délkeleti irányú eltolódása azonos nagyságrendű, azaz 18±7 mm/év. Így a Tibeti-fennsík eltolódásának hatása a szeizmicitás eloszlására — a lényegesen nagyobb kéregvastagság miatt — az Indiai- és Burmai-lemezek, valamint a Tibeti-fennsík találkozási zónájában nagyobb lenne, mint magukon az Indiai- és Burmai-lemezeken. Általában az egész területen sekély földrengéseket észlelnek, kivéve a Burmai-ívet, ahol közepes földrengések jelennek meg 200 km mélységig. Az ívszerű szeizmicitás szélessége maximum 24°É körüli, és mindkét oldalán csökken, befejeződik 21°É és 27°É-nál. A vető sík megoldások azt sugallják, hogy a kompresszív feszültségek az ív csapása mentén is hatnak; extenzionális feszültségeket is megfigyeltek. A cikkben egy modellt mutatunk be, hogy megmagyarázzuk a szeizmicitást, a fókuszmélységet, a frekvencia és feszültség eloszlást az ív zónájában, figyelembe véve a Tibeti-fennsík délkelet irányú eltolódását is.



## **DIRECT INTERPRETATION OF SELF-POTENTIAL ANOMALIES DUE TO SPHERICAL STRUCTURES — A HILBERT TRANSFORM TECHNIQUE**

**N. SUNDARARAJAN<sup>\*</sup> and M. NARASIMHA CHARY<sup>\*\*</sup>**

A direct interpretation is developed by means of horizontal and vertical derivatives of self-potential anomalies due to point poles and spheres. The vertical derivative is obtained via the Hilbert transform. The depth to the centre of the sphere, the angle of polarization and the multiplicative factor comprising the resistivity of the surrounding medium and current density are evaluated directly by simple mathematical expressions based on the abscissae of the points of intersection of these derivatives. The procedure is illustrated with a theoretical example in each case. The effect of random noise on the interpretation is studied by adding Gaussian noise to the anomaly whereupon it was found that noise has little influence on the process of interpretation. Analysis of the field data pertaining to the 'Weiss' anomaly of eastern Turkey substantiates the validity of the method. This interpretive procedure can easily be automated.

**Keywords: self-potential, anomaly, convolution, Hilbert transform, spherical structure**

### **1. Introduction**

Of all the electric methods, the use of the self-potential method enjoys wide application including engineering, ground water, subsurface temperature distribution as well as mineral investigations. Fast and refined techniques for interpreting self-potential anomalies are not in vogue: this is because self-potential data are complicated by a considerable amount of noise, and may be constant or varying. High noise levels pose serious interpretational hazards in developed areas. However, scrupulously performed field procedures combined

\* Centre of Exploration Geophysics, Osmania University, Hyderabad-500 007, India

\*\* Presently with the Central Ground Water Board, Southern Region, Hyderabad-500 027, India

with noise source mapping will certainly give reproducible data and prevent noise from being mistaken for signals.

In general the quantitative interpretation of SP anomalies is accomplished by approximating the source to simple regular geometrical shapes such as cylinders, spheres, sheets, etc. The available techniques are similar to those developed for gravity and magnetic interpretation. Despite there being quite a few methods for interpreting SP anomalies, they are subject to many constraints.

Estimates of anomaly source configuration, depth and other parameters for simple models can be made using analytical formulae. Some of these methods make use either of certain characteristic points on the anomaly or of nomograms [YÜNGÜL 1950]. The use of nomograms based on the method of BHATTACHARYA, ROY [1981], is somewhat crude and inadequate [RAJAN et al. 1986]. Curve matching techniques [MEISER 1962] proved to be cumbersome, especially when there are too many parameters to be determined. The least squares method involves a series of trials in minimizing the difference between observed and calculated values. All these methods have their own interpretational drawbacks.

AGARWAL [1985] made use of the amplitude of the analytic signal for interpreting self-potential anomalies caused by spherical structures. Despite the fact that this approach is essentially based on the use of the Hilbert transform, the method remains an empirical one wherein the parameters of the causative body are somewhat related to the shape and size of the amplitude curve [NABIGHIAN 1972].

We present herein a simple and refined mathematical procedure using the Hilbert transform for a straightforward evaluation of the parameters of the body. This method is based on the use of horizontal and vertical derivatives of the anomalous field. The vertical derivative is obtained via the Hilbert transform. The method is bound to yield more accurate results than the methods listed above since the present method is based on the real roots of the derivatives of the SP anomalies [SUNDARARAJAN et al. 1990, SUNDARARAJAN et al. 1994]. Similar methods are made use of in the gravity and magnetic interpretation and found to be much simpler as well as being elegant and accurate [MOHAN et al. 1982, SUNDARARAJAN 1982, SUNDARARAJAN et al. 1983].

If  $HD(x)$  and  $VD(x)$  are the horizontal and vertical derivatives respectively of any order of the self-potential anomaly then, according to SUNDARARAJAN [1982], they form a Hilbert transform, which implies that the vertical derivative of the field can be computed from the horizontal derivative or vice versa. This is expressed as:

$$HD(x) \xleftrightarrow{HT} VD(x)$$

where  $HT$  is the Hilbert transform operator.

This can mathematically be stated as:

$$VD(x) = \frac{P}{\pi} \int_{-\infty}^{\infty} \frac{HD(y)}{(x-y)} dy \quad (1)$$

The divergence of  $x=y$  is allowed for by taking Cauchy's principal value ( $P$ ) of the integral [BRACEWELL 1986]. The function  $VD(x)$  is a linear function of  $HD(x)$  which in fact is obtainable from  $HD(x)$  by convolution with  $(1/\pi x)$ . This relationship is stated as:

$$VD(x) = (1/\pi x) * HD(x) \quad (2)$$

where  $*$  denotes the convolution.

The discrete form of the above relation is expressed as [TANER et al. 1979]:

$$VD(x) = \frac{2}{\pi} \sum_{n=-\infty}^{\infty} HD(x - n\Delta x) \frac{\sin^2(n\pi/2)}{n} \quad n \neq 0 \quad (3)$$

where  $\Delta x$  is the station interval and  $n$  is the total number of stations on a profile.

Alternatively, the discrete Hilbert transform (DHT) can also be computed via the discrete Fourier transform (DFT) very efficiently using the fast Fourier transform (FFT) algorithm. The DHT as a function of DFT can be defined as [MOHAN et al. 1982]:

$$VD(n\Delta x) = \sum_{m=0}^{N-1} \text{Im } HD(mw_0) \cos(mw_0n\Delta x) - \text{Re } HD(mw_0) \sin(mw_0n\Delta x) \quad (4)$$

where  $\text{Re } HD(mw_0)$  and  $\text{Im } HD(mw_0)$  are real and imaginary components of the DFT of the horizontal derivative,  $w_0$  is the fundamental frequency expressed in radian/unit length and is given as  $w_0 = 2\pi/N\Delta x$ , and  $N$  is the total number of samples on a profile.

Further, the complex analytical signal  $A(x)$  can be defined as a complex function whose real and imaginary parts are the horizontal and vertical derivatives of the potential function:

$$A(x) = HD(x) + iVD(x) \quad (5)$$

The amplitude of the analytical signal helps to locate the origin of the causative body. The amplitude is given as:

$$AA(x) = [HD(x)^2 + VD(x)^2]^{1/2} \quad (6)$$

The function  $AA(x)$  attains its maximum over the origin. It is true for all two- and three-dimensional structures. In addition, the amplitude is also useful for interpreting structures of arbitrary shape. The location of origin based on amplitude is the unique feature of this method. The method remains the same for all potential field anomalies of 2-D and 3-D structures irrespective of their geometrical configuration.

## 2. SP field due to a point pole

Figure 1 represents the geometry of the pole. Let  $SPI(x)$  be the potential at a point  $P(x, y = 0, 0)$  due to a point pole of strength  $E$  placed at a point  $Q(x', z)$ . The potential due to such a pole is given as [AGARWAL 1985]:

$$SPI(x) = \frac{E}{[(x - x')^2 + z^2]^{1/2}} \quad (7)$$

where  $z$  is the depth to the pole.

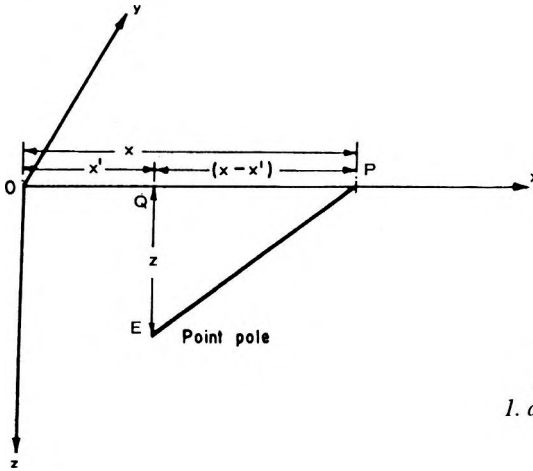


Fig. 1. Geometry of point pole  
1. ábra. Pontszerű pólus geometriája

Performing partial differentiation of Eq. (7) with respect to  $x$  and  $z$ , the horizontal and vertical derivatives of  $SPI(x)$  are obtained as:

$$HDI(x) = \frac{-E(x - x')}{[(x - x')^2 + z^2]^{3/2}} \quad (8)$$

$$VDI(x) = \frac{-Ez}{[(x - x')^2 + z^2]^{3/2}} \quad (9)$$

Since Eqs. (8) and (9) are of first degree in  $x$ , we have:

$$HDI(x) = VDI(x) \quad \text{at} \quad x = x_1$$

which implies that,

$$z = (x - x') = x_1 \quad (10)$$

i.e. the depth to the point pole is equal to the abscissa of the point of intersection of the horizontal and vertical derivatives.

Since the potential or the derivatives are known at every  $x$ , the pole strength  $E$  can be calculated from Eqs. (7), (8) or (9).

### 3. SP field due to a sphere

With reference to Fig. 2, the geometry of the obliquely polarized sphere with radius  $a$  is considered. In the cartesian coordinate system,  $O$  is the origin: on the surface at a point vertically above the centre of the sphere. The axis of the sphere is parallel to the  $y$ -axis.  $AA'$  is the axis of polarization,  $\Theta$  is included between the polarization- and  $x$ -axis.  $P$  is the point of observation at a distance  $x$  from the origin,  $\alpha$  is the angle between the axis of polarization and the line passing through the centre of the sphere and  $P$ .  $Q$  is the point where the potential is zero. Therefore, the potential at a point  $P$  on the surface is given as [AGARWAL 1985]:

$$SP2(x) = C \frac{(z \cos\Theta + x \sin\Theta)}{(x^2 + z^2)^{3/2}} \tag{11}$$

where  $z$  is the depth to the centre of the sphere,  $\Theta$  is the angle of polarization, and  $C$  is a constant comprising the current density ( $I$ ) and the resistivity ( $\rho$ ) of the surrounding medium as:

$$C = I\rho/2\pi .$$

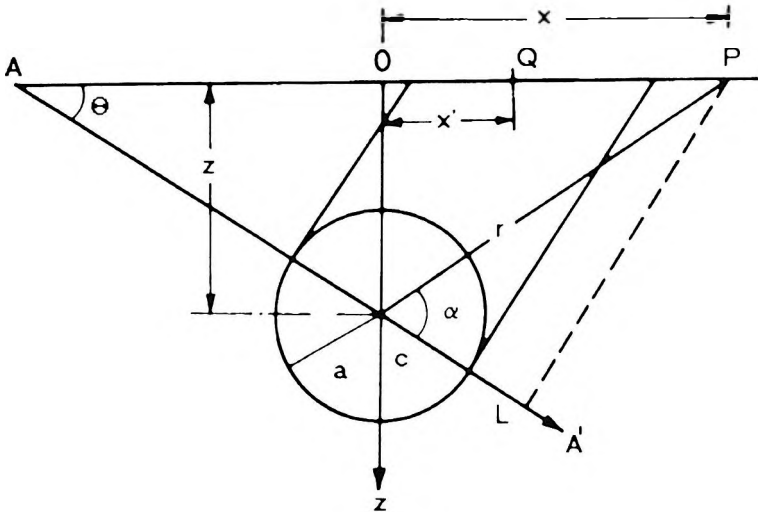


Fig. 2. Geometry of sphere  
2. ábra. Gömb alakú pólus geometriája

Partial differentiation of Eq. (11) with respect to  $x$  and  $z$  yields the horizontal and vertical derivatives of  $SP2(x)$ :

$$HD2(x) = C \frac{(z^2 - 2x^2) \sin\Theta - 3xz \cos\Theta}{(x^2 + z^2)^{5/2}} \quad (12)$$

and

$$VD2(x) = C \frac{(x^2 - 2z^2) \cos\Theta - 3xz \sin\Theta}{(x^2 + z^2)^{5/2}}. \quad (13)$$

Analyzing the results we obtain that at  $x=0$ , Eqs. (12) and (13) reduce to:

$$HD2(0) = C \sin\Theta / z^3 \quad (14)$$

$$VD2(0) = -2C \cos\Theta / z^3 \quad (15)$$

The angle of polarization  $\Theta$  can be evaluated from Eqs. (14) and (15) as:

$$\Theta = \tan^{-1} [-2HD2(0)/VD2(0)] \quad (16)$$

Since Eqs. (12) and (13) are of second degree in  $x$ , we have:

$$HD2(x) = VD2(x) \quad \text{at} \quad x = x_1, x_2 \quad (17)$$

Further simplification leads to the solution of  $z$  as:

$$z = (x_1 + x_2) \frac{(\cos\Theta + 2\sin\Theta)}{3(\sin\Theta - \cos\Theta)} \quad (18)$$

It would be worth mentioning here that  $z$  tends to infinity when  $\Theta=45^\circ$ ; this is purely a hypothetical case and it can be attributed to the fact that  $(x_1+x_2)=0$  which introduces catastrophe in the mathematical procedure. That is, the magnitude of the real roots of the derivatives are equal with opposite sign. In this case, which is seldom encountered in practice, the depth is simplified as:

$$z = x_1 = -x_2 \quad (19)$$

Also, from Eqs. (12) and (13), the constant term  $C$  is obtained as:

$$C = \frac{2z^3[HD2(0)^2 + VD2(0)^2]^{1/2}}{(1 + 3\cos^2\Theta)} \quad (20)$$

Thus, equation (20) yields either the current density ( $I$ ) or the resistivity ( $\rho$ ) of the surrounding medium provided the other parameters are known.

#### 4. Theoretical example

The interpretive process detailed above is illustrated with a theoretical example in each case. The self-potential anomalies (*Figs. 3 and 4*) pertaining to point pole and sphere are computed using Eqs. (7) and (11) for a set of model parameters (*Table 1*). *Figures 5 and 6* correspond to the first horizontal

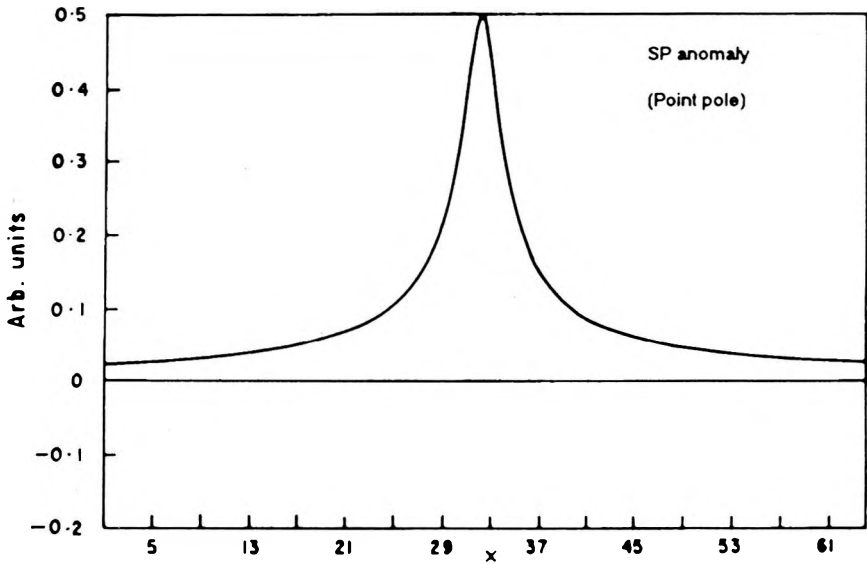


Fig. 3. SP anomaly due to a point pole  
 3. ábra. Pontszerű pólus által keltett SP anomália

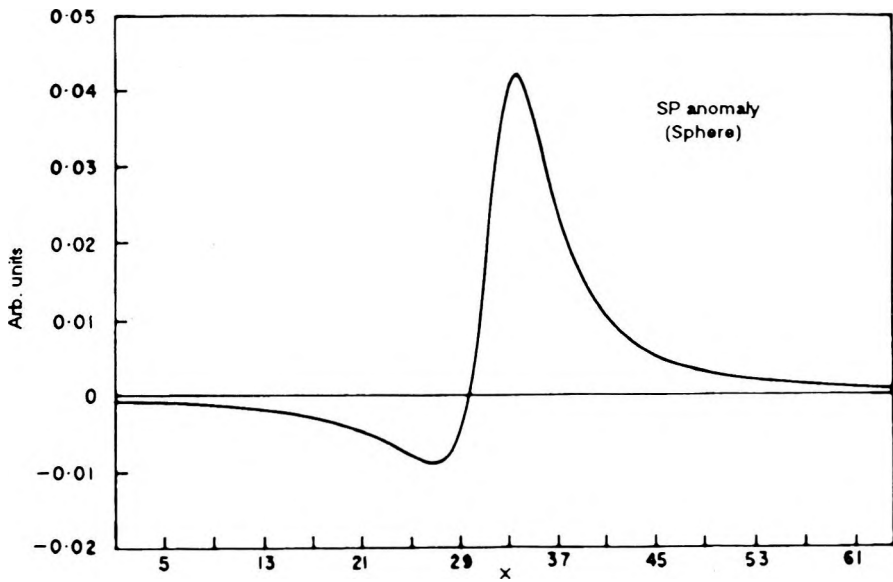


Fig. 4. SP anomaly due to a sphere  
 4. ábra. Gömb alakú pólus által keltett SP anomália

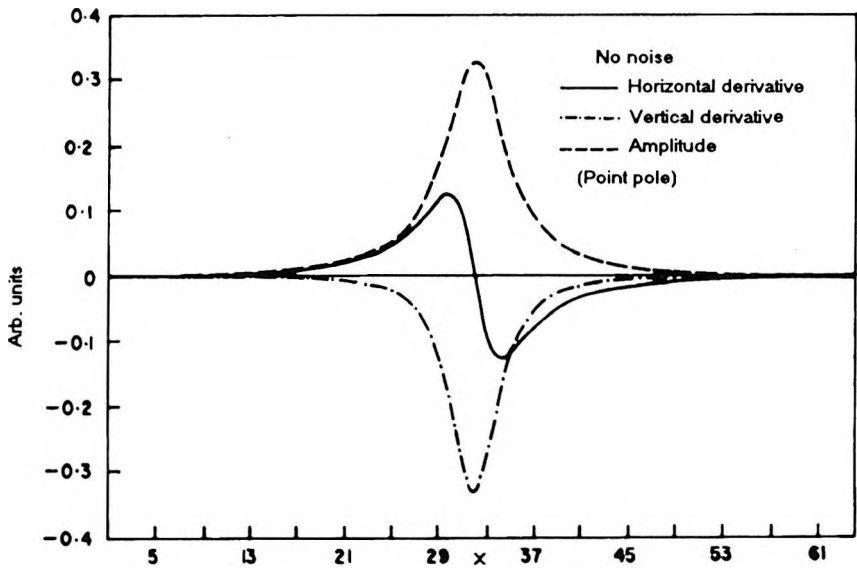


Fig. 5. First horizontal derivative, vertical derivative and amplitude of point pole  
5. ábra. Pontszerű pólus első horizontális deriváltja, vertikális deriváltja és amplitúdója

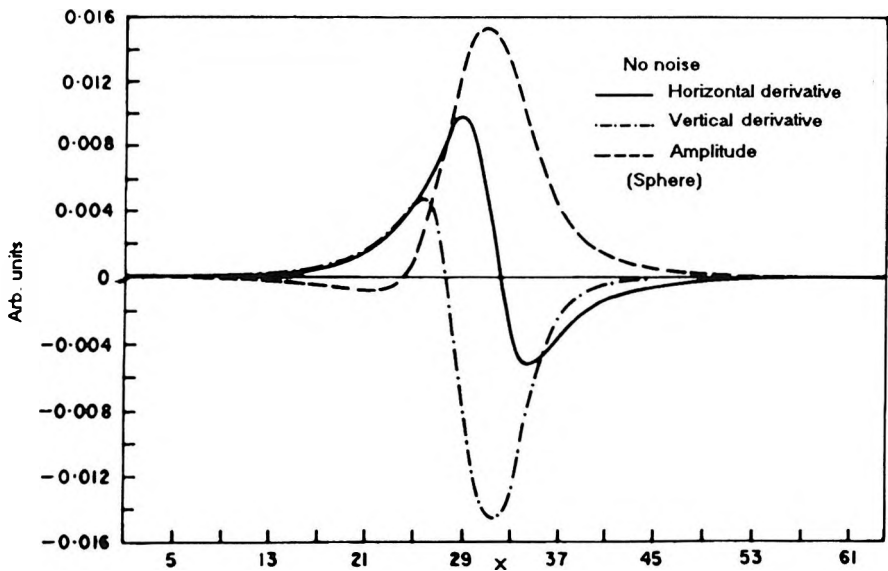


Fig. 6. First horizontal derivative, vertical derivative and amplitude of sphere  
6. ábra. Gömb alakú pólus első horizontális deriváltja, vertikális deriváltja és amplitúdója

derivative, the Hilbert transform and the amplitude in the case of point pole and sphere respectively. After precise location of origin with a knowledge of amplitude, the parameters of the causative bodies are evaluated based on the procedure detailed in the text. The assumed and interpreted values of the parameters are given in Table I and are in very good agreement.

Models	Parameters	$\Theta$ [degree]	$h^*$	$C^*$
Point pole	Assumed	-	1.50	0.75
	Interpreted (noise free)	-	1.55	0.79
	Interpreted (with noise)	-	1.41	0.86
	Error	-	6 %	14.66 %
Sphere	Assumed	60.00	4.00	1.00
	Interpreted (noise free)	60.10	3.96	1.15
	Interpreted (with noise)	62.15	3.60	1.14
	Error	3.5 %	10 %	14 %

Table I. Theoretical examples (\* in arbitrary units)  
I. táblázat. Elméleti példák (\* tetszőleges egységekben)

## 5. Noise analysis

The effect of random noise on the interpretation is studied by incorporating Gaussian noise (Fig. 7) with SP anomalies. A part of this noise is added separately to the SP anomaly in both cases depending upon the magnitude of the SP field. The noisy SP anomalies due to these structures are shown in Figs. 8 and 9 along with the noise free anomalies. The first horizontal derivative of these anomalies is computed by means of numerical differentiation, then their Hilbert transforms are obtained by a discrete convolution process and thereby the amplitudes are computed. Figures 10 and 11 show the horizontal derivative, the Hilbert transform and the amplitude in the case of point pole and sphere respectively. As discussed earlier, the origin is located based on the amplitude information and the interpretation is carried out. The results are presented in Table I and it is observed that they showed no appreciable change due to the presence of noise in the SP anomalies.

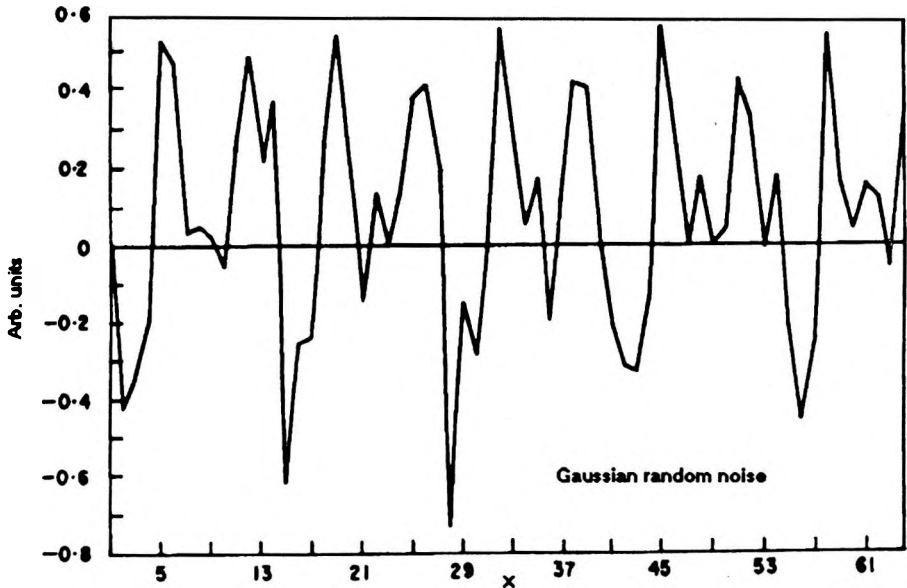


Fig. 7. Gaussian random noise  
7. ábra. Gauss eloszlású véletlen zaj

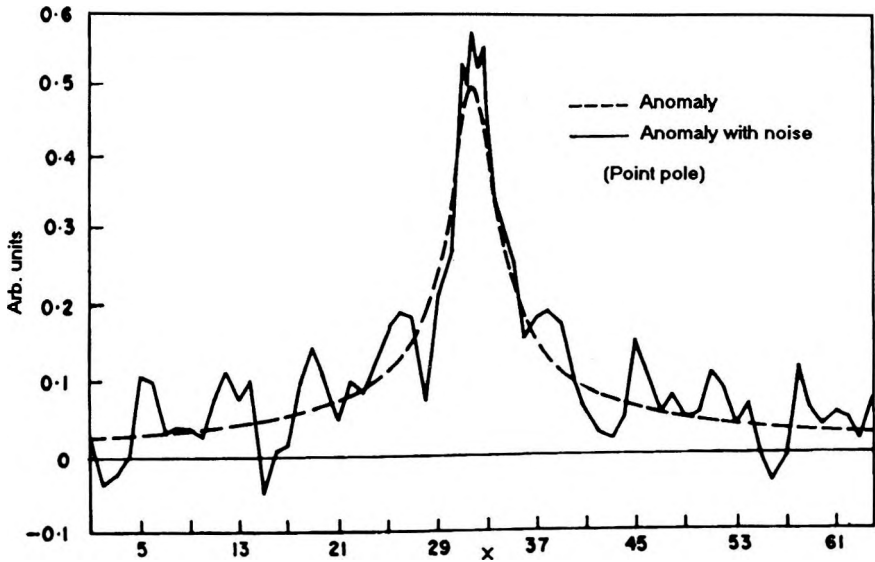


Fig. 8. SP anomaly with and without noise (point pole)  
8. ábra. SP anomália zajjal és zaj nélkül (pontoszerű pólus)

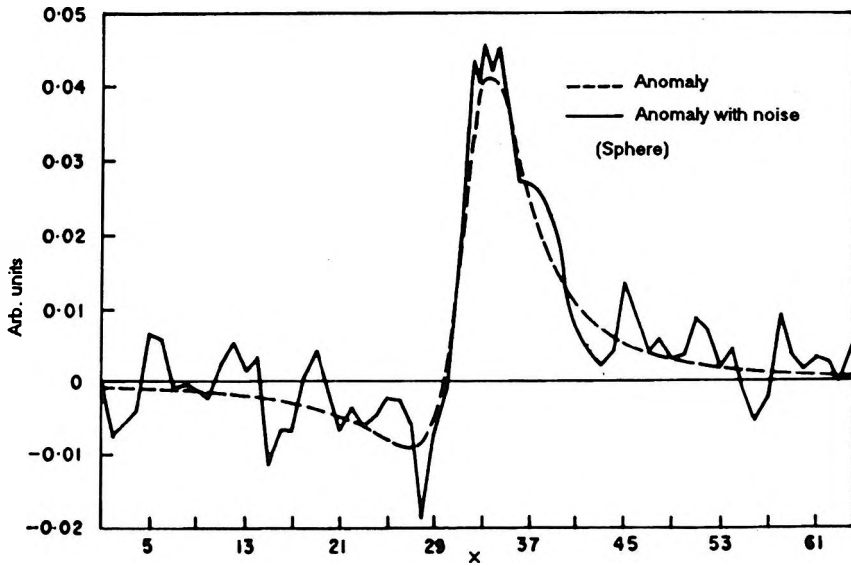


Fig. 9. SP anomaly with and without noise (sphere)  
 9. ábra. SP anomália zajjal és zaj nélkül (gömb alakú pólus)

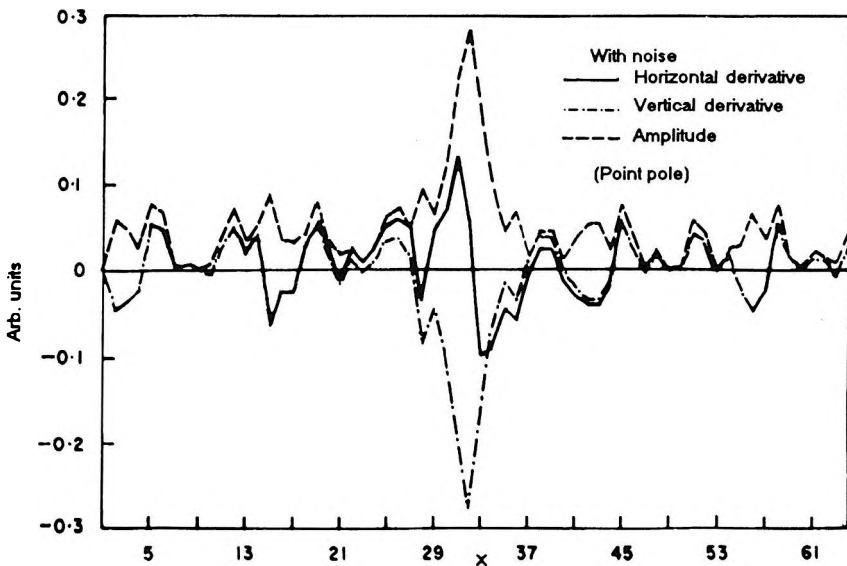


Fig. 10. First horizontal derivative of the noisy SP anomaly, the vertical derivative and the amplitude due to a point pole  
 10. ábra. Zajjal terhelt SP anomália első horizontális deriváltja, vertikális deriváltja és az amplitúdó, pontszerű pólus esetében

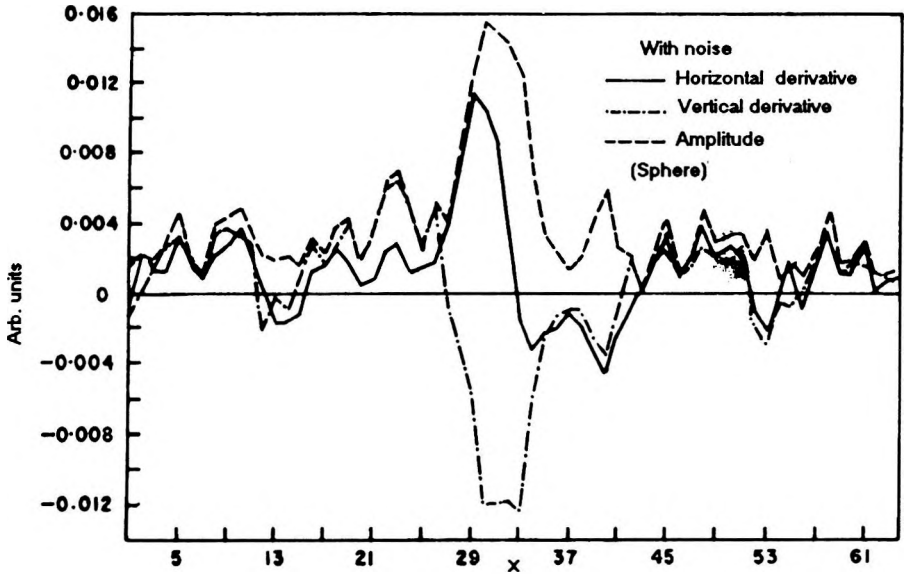


Fig. 11. First horizontal derivative of the noisy SP anomaly, the vertical derivative and the amplitude due to a sphere

11. ábra. Zajjal terhelt SP anomália első horizontális deriváltja, vertikális deriváltja és az amplitúdó, gömb alakú pólus esetében

## 6. Field example

The procedure just described is exemplified by the well known 'Weiss anomaly' (Fig. 12) of the copper deposit in eastern Turkey [BHATTACHARYA, ROY 1981]. This anomaly is one kilometer northwest of the Madam copper mine and is assumed to be due to spherical structure. At an appropriate scale the entire anomaly is digitized and then the first horizontal derivative is computed by means of numerical differentiation. Then the vertical derivative is obtained using the Hilbert transform. The horizontal derivative, the vertical derivative and the amplitude are shown in Fig. 13. The parameters are evaluated based on the procedure discussed above and the results are compared with those of YÜNGÜL [1950] and BHATTACHARYA, ROY [1981] and are presented in Table II.

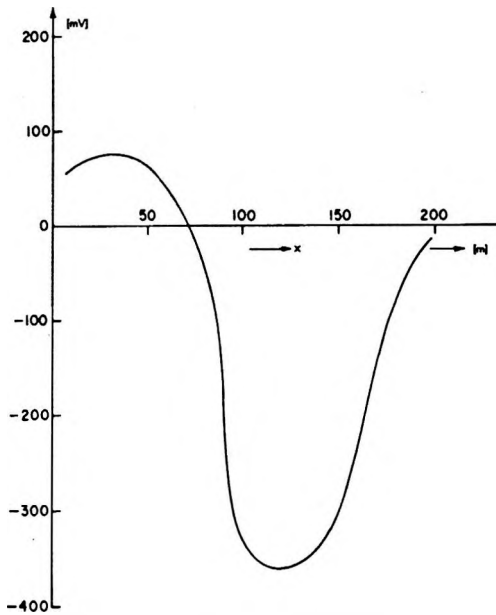


Fig. 12. SP anomaly (Weiss) of the Ergani copper deposit in eastern Turkey  
 12. ábra. Az Ergani rézlefordulás (Weiss) SP-anomáliája, Kelet-Törökország

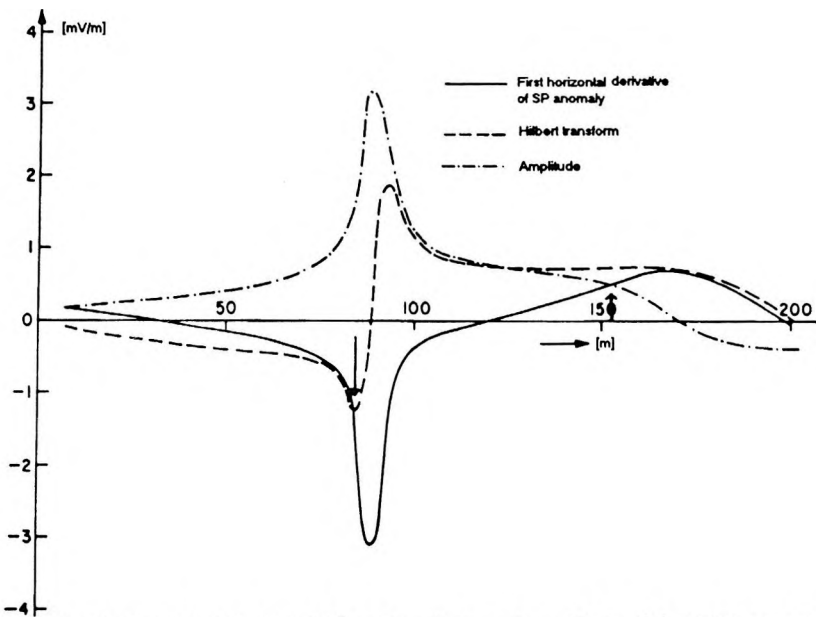


Fig. 13. First horizontal derivative, Hilbert transform and amplitude of the 'Weiss anomaly'  
 13. ábra. A „Weiss” anomália első horizontális deriváltja, Hilbert transzformáltja és amplitúdója

Parameters	$\Theta$ [degree]	$z$ [meter]
Present method	79.00	52.30
YÜNGÜL [1950]	64.00	53.80
BHATTACHARYA, ROY [1981]	54.00	30.00

Table II. Field example (Weiss anomaly)  
II. táblázat. Terepi példa (Weiss anomália)

## 7. Discussion

It is observed from the results (Table I) of noisy and noise free anomalies that there is no drastic change due to the presence of low level noise. However, there is a difference of around 5% to 15% between the assumed and interpreted (with noise) values. The maximum difference is seen only in the constant term comprising the resistivity of the surrounding medium and the current density.

Thus, the results testify that the method has no appreciable effect on the presence of random noise in the SP anomalies. A similar trend is observed even when the noise level is increased. However it is to be noted that for a very large amount of noise, the origin is slightly shifted either to the left or right of the actual origin without altering the values of the abscissae of the points of intersection of the derivatives.

A degree of error is inevitable in any method that makes use of discrete analysis and perhaps the error can be minimized by choosing an optimum sampling interval for processing. Further, the precise location of origin together with the exact values of the abscissae of the point of intersection of the derivatives ensure better accuracy of the interpreted results. The amplitude is not only useful in locating the origin but can also be made use of in estimating the parameters particularly when the causative bodies are of arbitrary structure [NABIGHIAN 1972].

Thus, the various parameters of the causative body are obtained by simple mathematical expressions as functions of real roots of the derivatives of SP anomalies and hence the method can easily be automated. Therefore the method is practicable and can be recommended to practising geophysicists.

## Acknowledgments

The authors wish to record their profound thanks to Mr. Udaya Shankar and his colleagues, Action for Food Production-Field Investigation Team-VI (AFPRO-FIT-VI), Hyderabad, for the computer facilities extended to them. The reviewers are thanked for their useful suggestions.

## REFERENCES

- AGARWAL P. N. 1985: Quantitative interpretation of self potential anomalies. Presented at the SEG Conference, Atlanta, USA
- BHATTACHARYA B. B., ROY N. 1981: A note on the use of a nomogram for self-potential anomalies. *Geophys. Prosp.* **29**, 1, pp. 102-107
- BRACEWELL B. 1986: Fourier transform and its applications. McGraw-Hill, New York
- MOHAN N. L., SUNDARARAJAN N., SESHAGIRI RAO S.V. 1982: Interpretation of some two-dimensional bodies using Hilbert transform. *Geophysics*, **47**, 3 pp. 376-387
- MEISER P. 1962: A method for quantitative interpretation of selfpotential anomalies. *Geophys. Prosp.* **10**, 2, pp. 203-218
- NABIGHIAN M. N. 1972: The analytical signal of two-dimensional magnetic bodies with polygonal cross-section: its properties and use for automated anomaly interpretation. *Geophysics* **37**, 3, pp. 507-517
- RAJAN N. S., MOHAN N. L., NARASIMHA CHARY M. 1986: Comment on 'A note on the use of a nomogram for self-potential anomalies'. *Geophys. Prosp.* **34**, 8, pp. 1292-1293
- SUNDARARAJAN N. 1982: Interpretation techniques in geophysical exploration using the Hilbert transform. Ph.D. thesis, Osmania University, Hyderabad
- SUNDARARAJAN N., MOHAN N. L., SESHAGIRI RAO S. V. 1983: Gravity interpretation of two dimensional fault structures using the Hilbert transforms. *J. Geophys.* **53**, 2, pp. 34-42
- SUNDARARAJAN N., ARUN KUMAR I., MOHAN N. L., SESHAGIRI RAO S. V. 1990: Use of the Hilbert transform to interpret self-potential anomalies due to two-dimensional inclined sheets. *Pure Appl. Geophys.* **133**, pp. 117-126
- SUNDARARAJAN N., SUNITHA V., SRINIVASA RAO P. 1994: Analysis of self potential anomalies due to inclined sheets of infinite depth extent. *Geophysics* (Accepted)
- TANER N. T., KOEHLER F., SHERIFF R. E. 1979: Complex seismic trace analysis. *Geophysics* **44**, 6, pp. 1041-1063
- YÜNGÜL S. 1950: Interpretation of spontaneous polarization anomalies caused by spheroidal orebodies. *Geophysics* **15**, 2, pp. 237-246

## GÖMB ALAKÚ SZERKEZETEK ÁLTAL KELTETT SAJÁTPOTENCIÁL ANOMÁLIÁK KÖZVETLEN ÉRTELMEZÉSE — EGY HILBERT TRANSZFORMÁCIÓS ELJÁRÁS

N. SUNDARARAJAN és M. NARASIMHA CHARY

Közvetlen értelmezési módszert dolgoztak ki pontszerű pólusok és gömbök okozta sajátpotenciál anomáliák horizontális és vertikális deriváltjainak alkalmazásával. A vertikális derivált Hilbert transzformációval nyerhető. Ezen deriváltak metszéspontjainak abszcisszáin alapuló, egyszerű matematikai kifejezésekkel becsülik a gömb középpontjának felszíntől mért távolságát, a polarizációs szöveget, és azt a szorzótényezőt, mely magába foglalja a környező közeg fajlagos ellenállását és az áram sűrűségét. Az eljárást minden esetben elméleti példával illusztrálják. A véletleneloszlású zaj értelmezésre gyakorolt hatását az anomáliához Gauss-eloszlású zajt adva tanulmányozzák és megállapítják, hogy a zajnak csekély hatása van az értelmezésre. A kelet-törökországi „Weiss” anomália terepi adatainak elemzése igazolja a módszer érvényességét. Ez az értelmezési eljárás könnyen automatizálható.



## BEHAVIOUR OF SP LOG IN A GRANITE RESERVOIR

Ali Belgasem BOURIMA \*

Spontaneous potential (SP) curves generally do not show clear responses in most igneous rocks since these rocks do not possess the electrochemical activities required to generate SP anomalies.

In other cases, however, the mineralogical structure of igneous rocks is accompanied by rich development of electrochemically active minerals, such as clay minerals, zeolites, and pyrite. In these cases significant SP anomalies can be recorded. In the Nafoora-Augila field of the Sirte basin, Libya, such SP anomalies were recorded in a granite reservoir. These anomalies are investigated and the related geochemical and hydraulic background is revealed. Accordingly, theoretical petrophysical models were elaborated based on the contribution of electromotive forces generated by electrochemically active minerals as well as on the contribution of fractures.

**Keywords:** SP anomalies, positive anomalies, negative anomalies, granite reservoir, fractures

### 1. Introduction

Shales are mixtures of various clay minerals, which are generally composed of silicon, aluminium, and oxygen. The most common clay mineral in granite is chlorite, which develops as a result of hydrothermal alteration of biotite, and kaolinite as a result of hydrothermal alteration of alkali feldspars. All clay minerals have one feature in common: their crystalline structure is dominated by tetrahedral disposition of the silicon and oxygen atoms and an octahedral arrangement of the aluminium and oxygen atoms.

The nature of the structure of the clay mineral crystals in which oxygen ions occupy the outer extremities, determines the net negative charge on the lattice [SERRA 1986].

\* The Libyan National Oil Corporation (NOC), Joint Venture Dep. Elsyadi street, Tripoli, Libya  
Current address: Geophysical Department, Eötvös Loránd University (ELTE), H-1083 Budapest, Ludovika tér 2.  
Manuscript received: 4 March, 1992

The resulting negative charge loosely binds the cations to clay and repulses the anions. In effect, a clay bed acts as an ion sieve allowing only cations to permeate or pass through its structure. This property gives rise to the clay potential [HELANDER 1983].

If the water of formation is more saline than the mud, a larger number of ions from the formation water than from the mud will move into the clay. The net effect will be a flow of cations (+) through the clay to the mud.

Because of the predominantly excess negative charges of the clay framework, anions cannot migrate in the same way so each cation transferred from the formation water to the mud leaves a negative charge behind in the formation water and adds a positive charge to the mud. This accumulation of charges makes the electrical potential of the formation water more negative and that of the mud more positive. This potential difference across the clay is then equal to the electromotive force (emf) of the cell. Zeolites are also deposited along fractures in the granite [ROBERTSON Group 1990]. They are believed to behave similarly to clay minerals with respect to their electrochemical activity. Both clay minerals and zeolites exhibit the same SP responses, namely they will show positive SP anomalies in the drilling mud when this mud is less saline than the interstitial water (i.e. in the 'normal' case).

On the other hand, metallic minerals, such as pyrite, are characterized by their dominant positive charges at their inner surfaces that are in contact with the less saline drilling mud. Hence, the electrochemical activity of pyrite is attributed to the potential difference generated by excess positive charges on pyrite which charges are, in turn, compensated by excess negative charges in the drilling mud [DAKNOV 1967]. The result is that the pyritic zones will show negative SP anomalies. The depositional manner of pyrite along the fractures governs the magnitude of the SP amplitude.

In a borehole drilled in a granite reservoir in the Nafloora-Augila field, Sirte basin (*Fig. 1*), the SP curve demonstrates a number of informative features. The granite shows complicated mineral development. The upper level of the interval is dominated by weathered granite, where orthoclase was partially or totally kaolinized. The lower part is characterized by extensive fractures of different magnitude (i.e. aperture, density, number of fractures/meter, extension). These features were the sites for precipitation of some transported minerals such as pyrite and zeolites. Chlorite developed in some zones as a result of hydrothermal alteration of biotite. Besides, some fractures are assumed to be partially or totally open.

## 2. Qualitative analysis of the SP anomalies

*Figure 2* shows the recorded SP versus depth along with other measured logs. Quite distinctive SP features can be seen from this curve. By quick look investigation, one can attribute these anomalies to different minerals which developed within the granite.

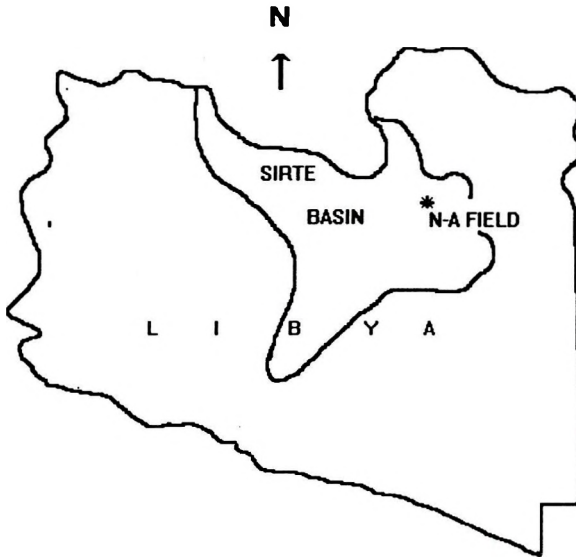


Fig. 1. Nafoora-Augila field of the Sirte Basin, Libya (not to scale)  
 1. ábra. Nafoora-Augília mező a Sirte-medencében (nem méretarányos)

In the Nafoora-Augila borehole under investigation the mud resistivity ( $R_m$ ) is equal to  $0.375 \Omega\text{m}$  at bottom-hole temperature (BHT), while the formation-water resistivity ( $R_w$ ) is about  $0.0178 \Omega\text{m}$ . This means  $R_m$  is greater than  $R_w$  by more than twenty-one times, which is quite favourable for the development of SP anomalies of electrochemical nature in the granite.

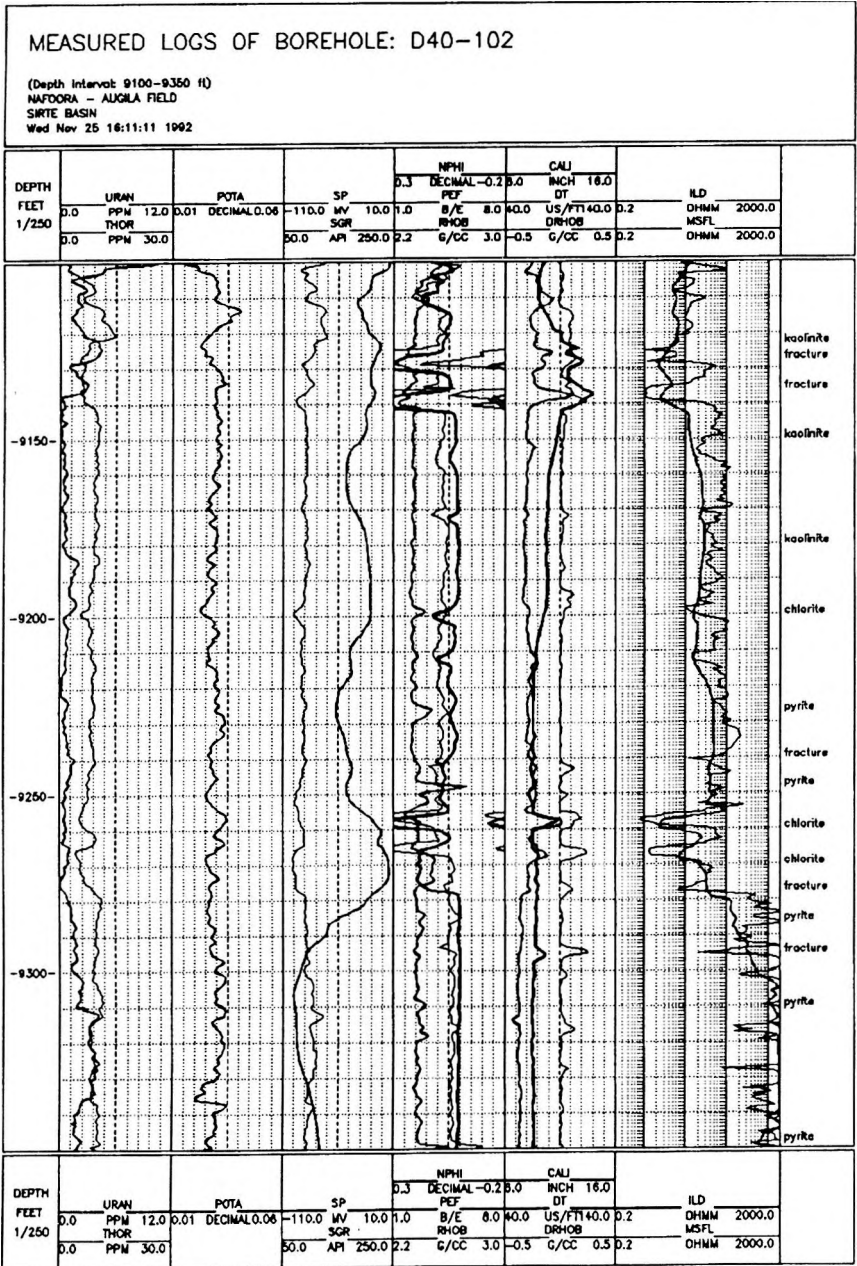
There are four main electrochemically active minerals within the granite body in this borehole. They include clay minerals (i.e. kaolinite and chlorite), zeolite minerals, and pyrite. These minerals can be classified into two groups on the basis of electrochemical activity:

- electrochemically positive minerals: i.e. kaolinite, chlorite, and zeolites;
- electrochemically negative minerals: i.e. pyrite.

The SP anomalies are generated by these electrochemically active minerals. However, the open fractures play only a minor role since they do not generate SP currents but contribute to the SP current flow as passive electrical conductances if they (i.e. the fractures) are filled with electrolytes, namely conductive mud and/or interstitial water.

Nuclear-type geochemical logs (Pe, formation density  $\log \rho_b$ , neutron porosity  $\log \phi_N$ , and spectral gamma ray  $\log \text{SGR}$ ) were utilized to identify electrochemically active minerals based on the criteria explained in Appendix I. By analysing all these logs I found that the revealed zones of electrochemically active minerals are in accordance with the developed SP anomalies (Fig. 2).

Pyrite was revealed at about eleven intervals or places (Fig. 2). The SP curve exhibits good agreement with the pyritic zones, where negative anoma-



Continuation of Fig. 2.

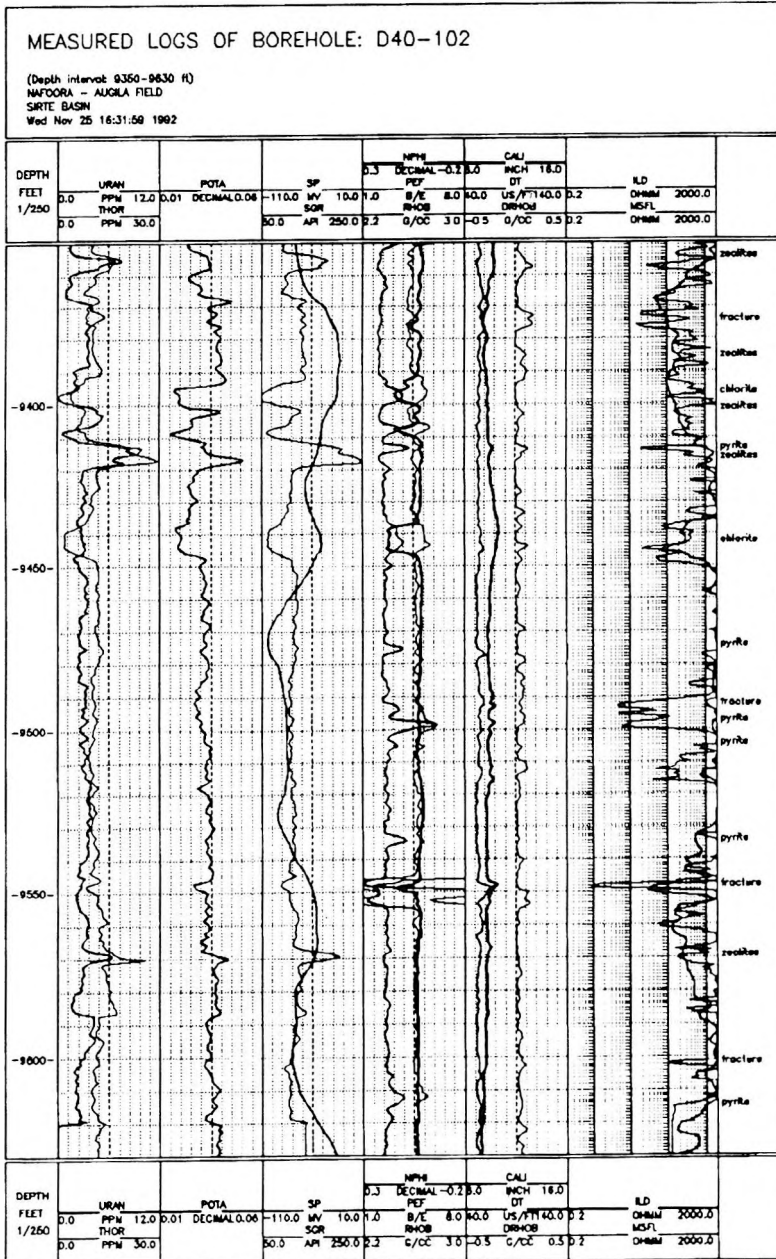


Fig. 2. Recorded SP log along with other measured logs in the granite studied  
2. ábra. Mért SP szelvény, a tanulmányozott gránitban felvett egyéb szelvényekkel

lies were recorded. Chloritic zones were assumed to be developed at about six sites, and the SP represented these zones by positive excursions. The same is the case with respect to zeolitic zones, where the SP responded with positive anomalies (Fig. 2, Fig. 3). At the upper interval indicated in Fig. 2, kaolinite-rich places also responded with positive SP anomalies.

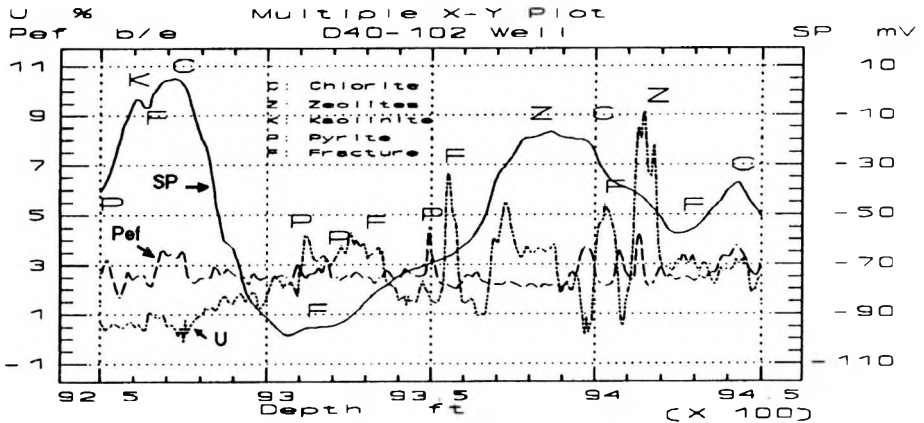


Fig. 3. SP, Pef and U logs of depth interval 9250-9450 ft (2819-2880 m) of well D40-102 showing the general relationships between the SP curve, Pef and U logs responses to electrochemically active minerals as well as fractures

3. ábra. A 9250-9450 ft (2819-2880 m) mélységintervallum SP, Pef és U szelvényei a D40-102 fúrólukban, általános összefüggéseket mutatnak az SP, Pef és U szelvényeknek az elektrokémiai aktív ásványokra és a repedezettségekre adott válaszaikra

Figure 4 is a multi crossplot representing relations of thorium versus photoelectric cross section index and potassium logs as well as K-40 versus Pef and Th. All the possible fractures, open and partially or totally blocked were detected by combined application of the Micro Spherically Focused Resistivity log (MSFL) and the geochemical logs that will be explained later. All the nuclear logs were affected by a rugosity problem at the same places to different degrees. For this reason, it was rather difficult to identify the kind of minerals within these places. However, the SP curve was helpful as a means of recognizing these minerals. Chlorite was the most probable mineral to be developed within the rugose zones since positive SP anomalies were observed here.

One of the major tasks of well log analysis in granite is to reveal the hydraulically open fractures and to distinguish them from the closed ones. I analysed the possible contribution of the SP log to this challenging problem when there are no electrokinetic SP anomalies generated in the open permeable fractures as is the case in this borehole (Fig. 3 and Fig. 5). The open fractures serve as passive conductors, they will modify only the shape of the electrochem-

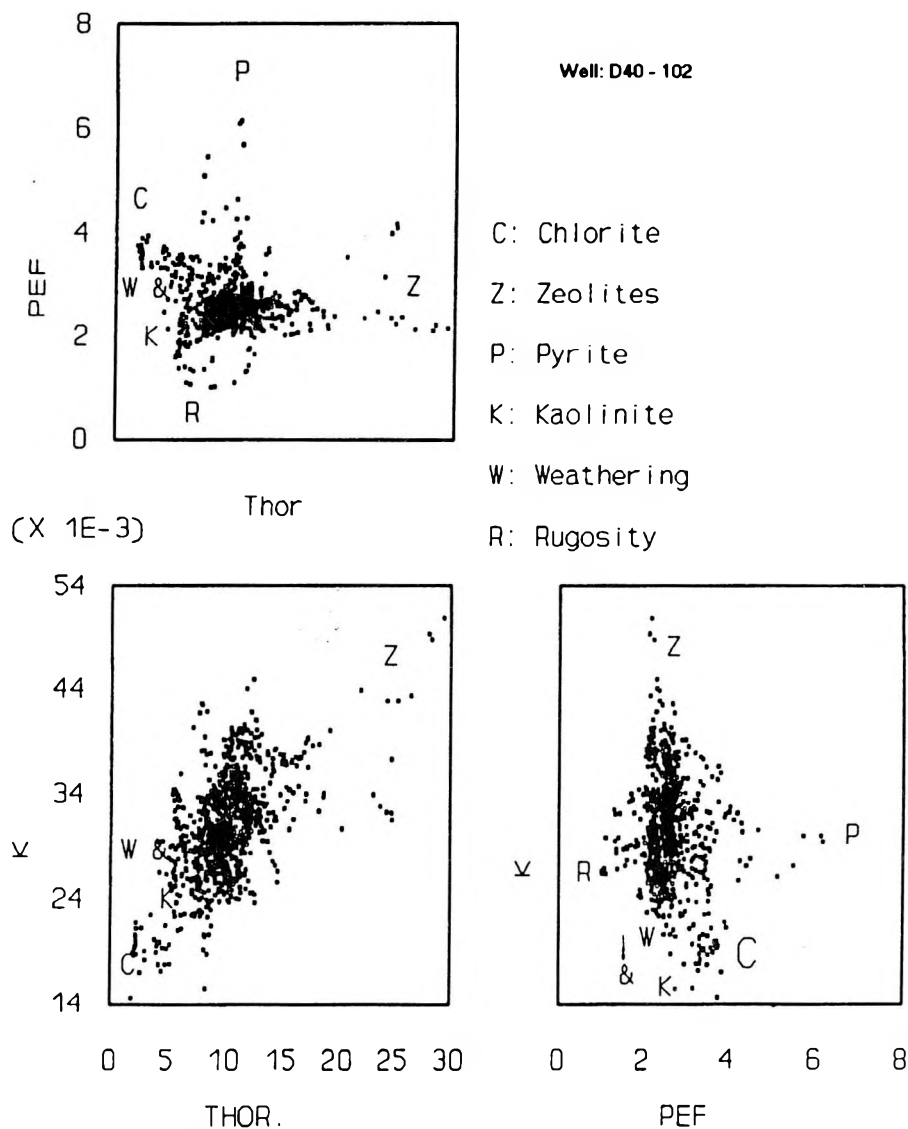


Fig. 4. Multicrossplot representing relations of thorium (Th), versus photoelectric cross section index (Pef), and potassium (K-40), measurements; as well as K-40 versus Pef and Th measurements

4. ábra. Többszörös korreláció a tórium (Th), a fotoelektromos keresztmetsvény index (Pef), és a kálium (K-40) mérések adatai; továbbá a K-40 és a Pef valamint Th mérések között

ical anomalies by providing a current path from the rock to the borehole or vice versa, the open fractures create positive or negative curvatures on the SP log which are superimposed on the negative or positive local SP anomalies caused by electrochemically active solid minerals.

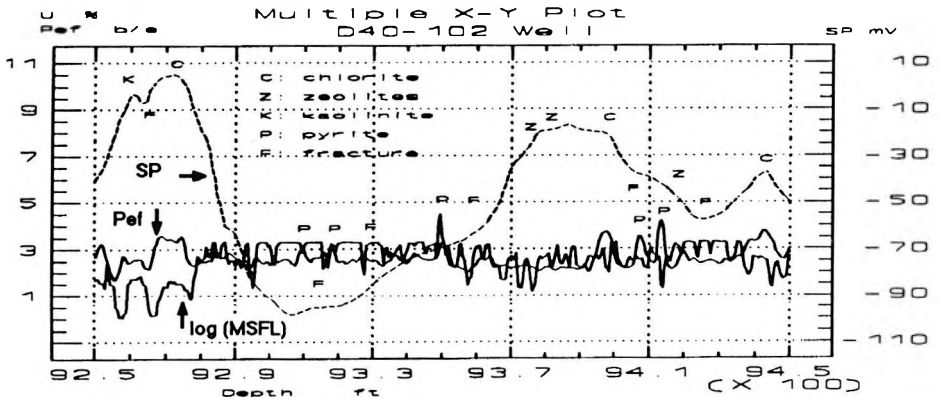


Fig. 5. SP, Pef and log(MSFL) of depth interval 9250-9450 ft (2819-2880 m) of D40-102 well showing the general relationship between the SP, Pef and MSFL logs responses to electrochemically active minerals as well as fractures

5. ábra. A 9250-9450 ft (2819-2880 m) mélységintervallum SP, Pef és log(MSFL) szelvényei, a D40-102 fúrólyukban, általános összefüggéseket mutatnak az SP, Pef és MSFL szelvényeknek az elektrokémiai aktív ásványokra és a repedezettségekre adott válaszaikra

One can conclude that the positive and negative curvatures on the SP logs which cannot be attributed to electrochemically active minerals are facing open fractures, accordingly they (i.e. negative and positive curvatures on SP logs) can indicate the sites of open fractures. Generally, fractured places are mainly located adjacent to hydrothermally altered zones which are clearly shown by SP curves (Figs. 2, 3 and 5, where some fractured sites are indicated).

### 3. Petrophysical models for the SP observations in the granite reservoir

Petrophysical models for the SP observations in granite are simply based on the fact that granite reservoir body includes some electrochemically active minerals. These minerals are distributed along the total interval. The SP anomalies are real reflections for these active electrochemical minerals because they are responsible for generating the SP electromotive forces. However, fractured zones and possibly permeable vuggy zones contribute only as passive conductors to the SP field. For this reason, fracture sites sometimes do not show significant correlation with the SP anomalies [BOURIMA 1993].

Figure 6 shows a model for simulating SP excursions. It is composed of pyritic active zone, hard granite, a chloritic zone of low concentration, fractured granite, and a chloritic active zone of relatively high concentration of chlorite.

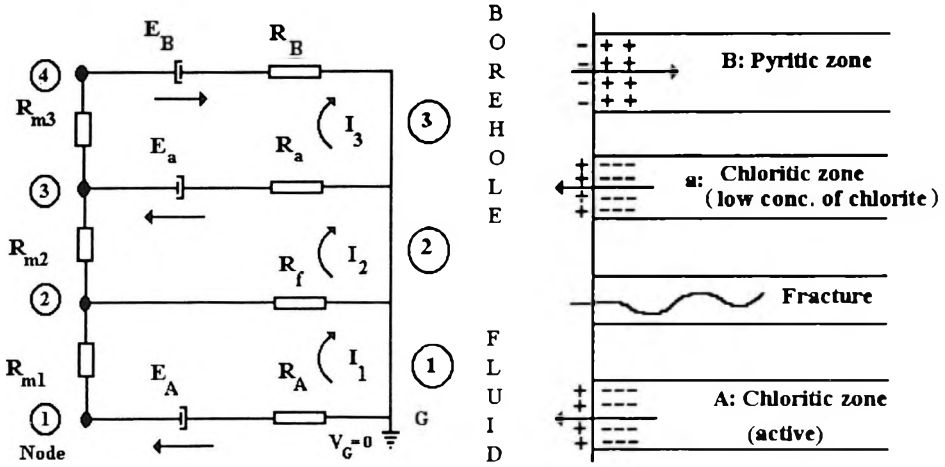


Fig. 6. Simple model composed of pyritic active zone, chloritic zone of low concentration, fractured granite, and active chloritic zone (right side) and related analog electrical network (left side).  $E$ —electromotive force;  $I$ —loop current;  $R_m$ —mud resistivity;  $R$ —resistivity of the rock zone

6. ábra. Aktiv pirites zónából, alacsony koncentrációjú zónából, repedezett gránitból és aktív kloritos zónából felépített egyszerű modell (jobb oldalon), valamint a hozzá tartozó analog elektromos hálózat (bal oldalon).  $E$ —elektromotoros erő;  $I$ — a hurokbani áram;  $R_m$ —fajlagos iszapellenállás;  $R$ —a kőzetzóna fajlagos ellenállása

The rock model of Fig. 6 is associated with the related analog electric network. This electric network is composed of a chain-structure of  $\pi$ -shaped cells which contain active electromotive forces, and passive resistances. The electromotive forces simulate the electrochemically active minerals such as pyrite, chlorite, zeolites and kaolinite. The fractures, as passive electrical conductances, are also taken into account. The electrical network also includes the mud column and the rock zones in the form of passive resistances. The presented network can be extended as far as the simulated rock components extend.

The analog network in Fig. 6 comprises three independent network loops: 1, 2, and 3. Loop currents  $I_1$ ,  $I_2$  and  $I_3$  are attributed to each loop, respectively, indicating also the expected positive direction of the loop currents. The active emf's are also included with their positive direction from the negative to the positive side of the active electric sources. The network is mathematically treated by means of the so-called loop voltage equations including the passive ohmic potential drops along the resistivities on the left side, and the active emf's on the right side of the equations:

$$I_1 (R_A + R_{m1} + R_f) + I_2 (R_f) = E_A \quad (1)$$

$$I_1 (-R_f) + I_2 (R_f + R_{m2} + R_a) + I_3 (-R_a) = -E_a \quad (2)$$

$$I_2 (R_a) + I_3 (R_a + R_{m3} + R_B) = E_B + E_a \quad (3)$$

By assuming all the included resistivities and the electromotive forces are known quantities, Eqs. (1), (2), and (3) can be solved by common mathematical rules in order to find out the three unknowns:  $I_1$ ,  $I_2$ , and  $I_3$ .

Accordingly:

$$D = (R_A + R_{m1} + R_f) [R_a^2 - (R_f + R_{m2} + R_a) (R_a + R_{m3} + R_B)] + R_f^2 (R_a + R_{m3} + R_B) \quad (4)$$

$$D_1 = E_A [R_a^2 - (R_f + R_{m2} + R_a) (R_a + R_{m3} + R_B)] + R_f [E_a (R_a + R_{m3} + R_B) - R_a (E_B + E_a)] \quad (5)$$

$$D_2 = (R_A + R_{m1} + R_f) [E_a (R_a + R_{m3} + R_B) - R_a (E_B + E_a)] - E_A R_f (R_a + R_{m3} + R_B) \quad (6)$$

$$D_3 = (R_A + R_{m1} + R_f) [E_a R_a - (E_B + E_a) (R_f + R_{m2} + R_a)] + R_f^2 (E_B + E_a) - E_A R_f R_a \quad (7)$$

Hence, the solution of the three unknowns can be obtained from these relations:

$$I_1 = \frac{D_1}{D} \quad (8)$$

$$I_2 = \frac{D_2}{D} \quad (9)$$

$$I_3 = \frac{D_3}{D} \quad (10)$$

Moreover, the voltage at the indicated nodes: 1, 2, 3 and 4 can be simply given by:

$$V_1 = -I_1 R_A + E_A \quad (11)$$

$$V_2 = V_1 - I_1 R_{m1} \quad (12)$$

$$V_3 = V_2 - I_2 R_{m2} \quad (13)$$

$$V_4 = V_3 - I_3 R_{m3} \quad (14)$$

Theoretically, the SP current enters the pyritic zone from the mud and leaves the chloritic zone into the mud column. The open fracture will be a possible path for the currents generated in the electrochemical cells. The mud column will also provide passive electrical conductances for the generated currents.

It has been proven by numerical values for the analog electric network (Appendix 2) that the SP voltage will give always distinct values for electrochemically active minerals. However, if a fracture site is located between two active mineral zones of different charges, the SP curve will show a reading lying not far from the straight line which connects the two active zones. The SP reading of the fracture shapes a positive curvature. The sharpness of this curvature is governed by the number of components in the electric network. *Figure 7* shows an example of numerical values for Fig. 6. The two curves represent the same parameters, with the exception of the fracture aperture which has been considerably increased. The right side curve is shifted to the right because of the larger width of fracture aperture, and the fracture is indicated by a stronger curvature. We can see that when the open fractures are located

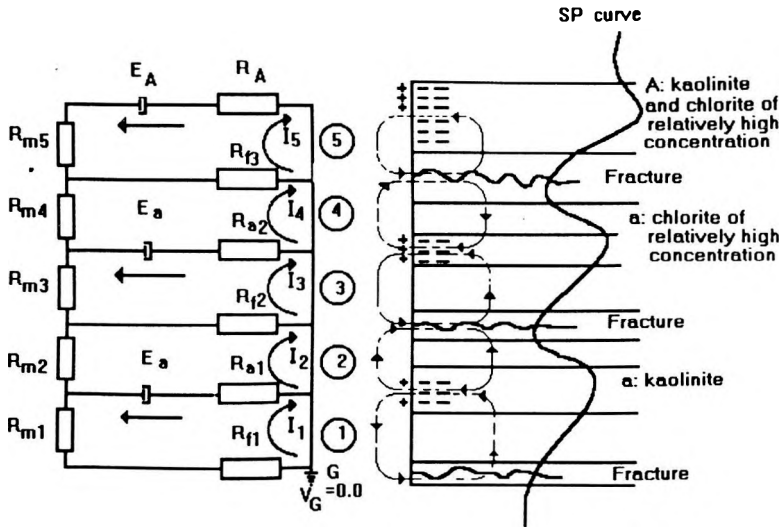


Fig. 7. Numerical calculations of the SP anomalies generated by the electrochemically active minerals and fractures presented in the model of Fig. 6

7. ábra. A 6. ábra modelljében szereplő kőzetpedés és az elektrokémiailag aktív ásványok által előállított SP anomáliák numerikus számítása

between mineralized zones of different electrochemical nature, the SP curve alone will generally not help much in identifying the open fractures.

Figure 8 is a model simulating the SP curve recorded within the interval 9120–9160 ft (2780–2792 m). Relatively positive anomalies were recorded at three different levels of chloritic and kaolinitic zones. However, in between, two negative anomalies can be seen on the SP curve caused by open fractures. In this case the SP log is useful for detecting the open fractures. From the nuclear-type geochemical logs, there was no indication of developments of electrochemically active minerals of negative SP anomalies, such as pyrite at high concentration. This means that the recorded negative SP anomalies were not generated by any active minerals. A possible explanation of these two SP negative anomalies is provided by open fractures as presented by the petrophysical model.

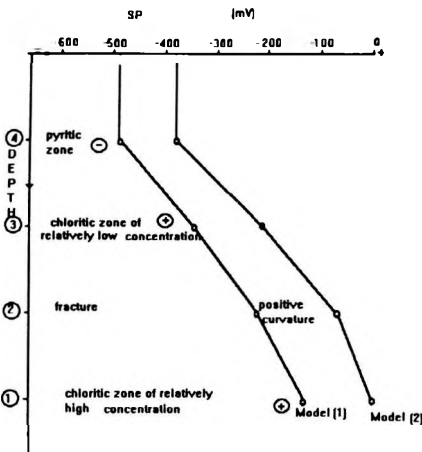


Fig. 8. Model simulating the SP curve recorded within the depth interval 9120–9160 ft (2780–2792 m). The related analog electrical network is shown on the left side

8. ábra. A 9120–9160ft (2780–2792 m) mélységintervallumban felvett SP görbét szimuláló modell. A hozzá tartozó analóg elektromos hálózat a bal oldalon látható

In the depth interval 9437.5–9549.5 ft (2876.5–2910.7 m) (Fig. 9) the SP curve responded to electrochemically positive chlorite at both the top and the bottom of the interval. Two negative electrochemically active zones (pyrite) were reflected by the SP curve at two separate sites that are adjacent to the indicated chloritic zones. Meanwhile in the middle of this interval the SP curve as well as the nuclear-type geochemical logs indicate a combined development of pyrite and zeolites. In this particular interval heavy fractures were assumed to be partly filled with pyrite, partly with zeolites, as a result of hydrothermal alterations. In Fig. 9 the petrophysical model (Appendix 3) to the depth interval can be seen; the measured SP curve is demonstrated at the upper part of this figure, the curve represents the estimated theoretical SP curve obtained by substituting optimized parameters for the lower analog electrical network.

Because of the complexity of this petrophysical model, where the number of the unknown loop currents is rather large, it is tedious to obtain a theoretical curve of close values to the measured one. Accordingly, a computer optimiza-

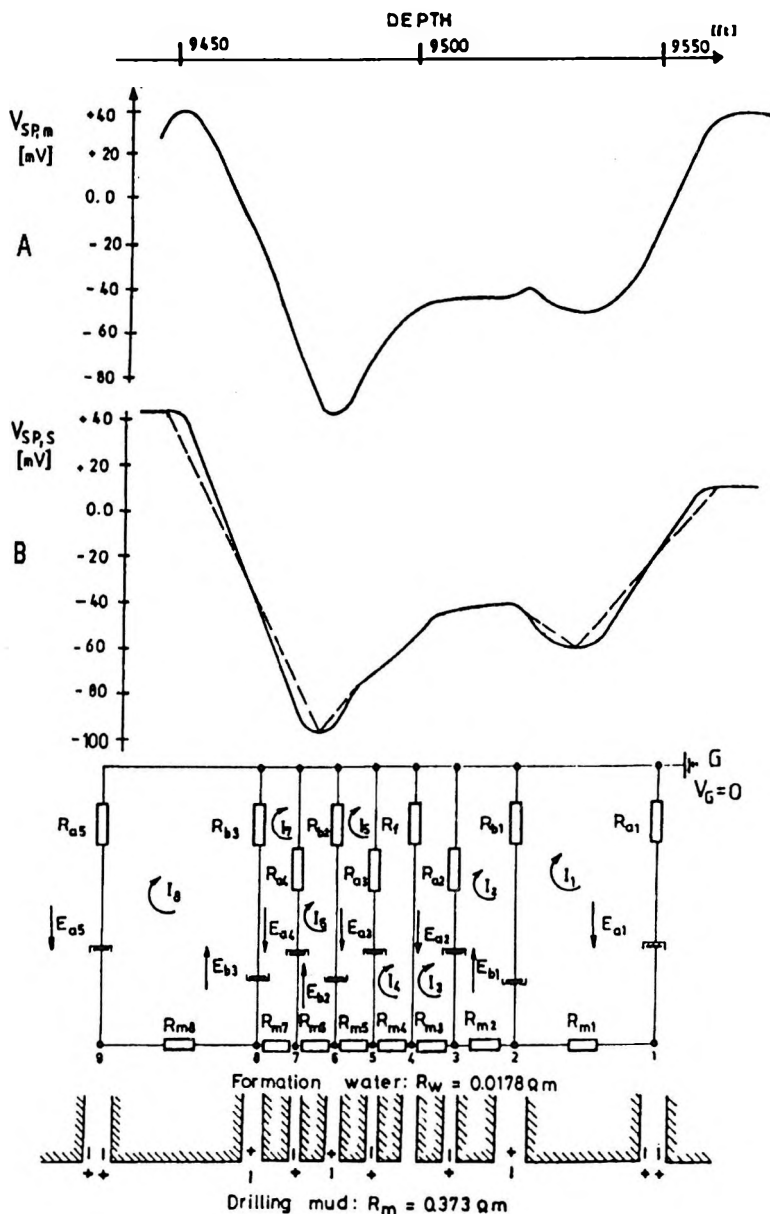


Fig. 9. SP curves and the analog electrical network of the petrophysical model. A—SP curve measured in the depth interval 9437.5–9549.5 ft (2876.5–2910.7 m) ( $V_{SP,m}$ ); B—estimated SP curve with optimized parameters of the network ( $V_{SP,s}$ )

9. ábra. Kőzettani modell SP görbéje és analóg elektromos hálózata. A—9437,5–9549,5 ft (2876,5–2910,7 m) mélységintervallumban mért SP görbe ( $V_{SP,m}$ ); B—a hálózat optimalizált paramétereivel becsült SP görbe ( $V_{SP,s}$ )

tion technique is recommended for similarly detailed and complicated models in order to obtain greater accuracy.

#### 4. Conclusions

The granite oil reservoir investigated here represents considerably useful SP excursions; these are mainly of electrochemical nature, where electrochemically active minerals, such as chlorite, kaolinite, zeolites and pyrite are the main minerals responsible for the SP anomalies. Both the nuclear-type geochemical logs and the SP log are correlated to indicate the electrochemically active minerals. In spite of the fact that the SP log does not show a distinct correlation with fracture sites, it is useful as a means of recognizing the possible fractures, particularly the open ones, along with other logs.

It has been found that the open fractures serve only as passive conductors. Because they cannot generate electrochemical emf's, they will only modify the shape of the electrochemical anomalies by providing a current path from the rock to the borehole or vice versa.

These petrophysical models and the related analog electrical network model offer a powerful technique for revealing the petrochemical and petrophysical background of the SP anomalies in the granite. In addition, these models are helpful in demonstrating the role of the open fractures in the SP excursions.

The proposed analog electric network calculations indicate that the SP will give distinctive extreme values for the emf's of electrochemically active minerals. However, if a fracture is located between two active zones of different electrical polarities, the SP curve will show readings lying not far from the straight line connecting the two active zones. At the same time, the SP log responds in a more clear manner to fractures located between two mineralized zones of the same electrochemical nature.

#### Acknowledgements

The author would like to thank the Libyan National Oil Corporation (NOC), for making the data for this work available. My great thanks are also due to Prof. Zoltán BARLAI for his helpful directives and constructive criticism during the analysis and writing-up of this paper. Sincere thanks are also expressed to Prof. Attila MESKÓ, head of the Geophysical Department of Eötvös Loránd University, Budapest, and Dr. Dezső DRAHOS for their help and support. This work is sponsored in part by the Libyan National Oil Corporation.

## REFERENCES

- BOURIMA A. B. 1993: New Synergetic Approach for An Oil-bearing Granite Reservoir Evaluation by Means of Well Logs, Ph.D. thesis, Hungarian Academy of Sciences, MTA, 1993, pp. 52-78
- CLAVIER C., HEIM A., SCALA C. 1976: Effect of pyrite on resistivity and other logging measurements. Paper HH, in the 17th Annual Logging Symposium Transactions: SPWLA, 1976, pp. 1-34
- CLIFTON R. 1986: Natural and Synthetic zeolites, United States of the Interior Bureau of Mines, pp. 2-10
- DAKNOV V. N. 1967: Electrical and magnetic methods of investigation of boreholes; Fundamentals of theory (in Russian), Published by Nedra, Moscow, 1967, pp. 345-348
- HELANDER D. P. 1983: Fundamentals of formation evaluation. OGCI Publications, pp. 77-97
- JUDSON S., KAUFFMAN M. E. 1990: Physical Geology, Eighth Edition, Prentice Hall Englewood Cliffs, New Jersey, pp. 39-133
- The Rebertson Group plc, 1990: Reservoir description and petrophysical study of the Nafoora-Augila Unit, Report prepared for The Arabian Gulf Oil Company, 1990.
- SERRA 1986: Fundamentals of well interpretation (part one). Elsevier, Amsterdam

## APPENDIX 1

## THE MAIN SECONDARY MINERALS IDENTIFIED AND THE CRITERIA USED FOR THEIR DISCRIMINATION

## KAOLINITE

Kaolinite is one of the main clay minerals. It is a hydrous aluminous silicate  $\text{Al}_4(\text{Si}_4\text{O}_{10})(\text{OH})_8$ . The structure consists of one sheet of silicon-oxygen tetrahedron each of which shares three oxygens to give the ratio of  $(\text{Si}_4\text{O}_{10})^{4-}$  linked with one sheet of aluminum hydroxyl.

The igneous rocks of the Nafoora-Augila field were affected by a diagenetic process where in certain parts of rock a series of transformations had taken place. Kaolinite was developed mainly in the weathered parts and possibly within fractures, brecciation and leached feldspar pores as a result of hydrothermal alteration of potassium feldspars.

Because of the weathering process that results in the development of kaolinite, Th, U, and K-40 were leached out from the affected zones. Thus, the spectral gamma ray logs generally show low values at these levels. On the other hand, neutron porosity shows increased values in such zones due to the hydrous structure of kaolinite and a possible increase in the total porosity, partly due to the created

unblocked part of fractures and/or vugs. However, it should be mentioned that the neutron porosity tools (CNL) are calibrated in limestone rock and different versions have some differences with respect to different rock matrix responses.

Lithodensity logs,  $\rho_b$  and  $P_{ef}$ , exhibit comparatively low values in response to kaolinite, however, they are not conspicuous enough to be used as an indicator for kaolinite accumulation.

The SP log is an important indicator showing positive SP anomalies for the existence of kaolinitic zones within the granite, where it is not easy to identify them by other geophysical well logs, especially when the kaolinite developed in limited quantities.

The importance of the SP is enhanced for kaolinite identification when it exists in a dehydrated form. In this case, the neutron porosity log, which usually gives distinctive values for kaolinite, becomes useless. Nevertheless, neutron porosity as well as lithodensity logs, can be utilized to discriminate between kaolinite and chlorite, which have the same positive SP anomalies.

### CHLORITE

Chlorite is a phyllosilicate of magnesium, aluminum, iron and calcium. Chlorite exhibits a cleavage similar to that of mica, but the small scales produced by the cleavage are not elastic, like those of mica [JUDSON, KAUFFMAN 1990].

In the granite of the Nafuora-Augila field, chlorite is the most dominant hydrothermally altered mineral. It is encountered in almost every weathered and non-weathered level. The chlorite is generated as a result of hydrothermal alteration of biotite. The alteration process usually takes place in fractures, breccia, faults and interconnected spaces where the circulation of fluids is possible.

Chlorite is characterized by relatively high lithodensity logs ( $\rho_b$  and  $P_{ef}$ ) and neutron porosity logs. Furthermore, chlorite exhibits positive (+) SP anomalies in the normal case. Thus, it is easy to recognize chlorite at first sight when the composite log is being investigated.

Chlorite is also conspicuously detected by natural gamma ray spectrometer logs. Chloritic zones usually exhibit considerably low gamma ray values. Evidently, the hydrothermal alteration processes are largely responsible for leaching out most of the existing radioactive host minerals.

### ZEOLITES

Zeolites consist of a crystalline framework of aluminous silicates. The structure contains channels and interconnected voids occupied by cations and water molecules [CLIFTON 1987].

The development of zeolite in igneous rocks can be related to:

- zeolites precipitated in hydrothermal systems from alkaline to weakly acidic hot water. Zeolites, when they occur in deep and hot zones, are in low forms; they may be, partly or totally dehydrated.
- zeolites crystallized during the late stages of formation of magmatic rocks. They commonly occur as fine crystals lining fractures and vugs in basic igneous rocks although they also occur as interstitial particles and globules. Crystalline zeolite forms through interaction of fluids with the surrounding rock.

Aluminum-rich zeolite occurs in basic igneous rocks with low silicon-to-aluminum ratio, whereas aluminum-poor zeolite occurs in igneous rocks which are rich in silicon [CLIFTON 1987].

Zeolite and clay minerals, such as kaolinite and montmorillonite, are composed of the same chemical elements in their crystal structures. Concerning the clay minerals, with the exception of smectites, their intercrystalline and interlayer water cannot be displaced by other molecules, such as radioactive radicals, but only the outer adsorption water can be displaced. Hence, the neutron porosity log usually records high values in clay minerals. With regard to the smectites, their interlayer water can be displaced, however, because of their instability, they are not found in old rocks such as Precambrian granite.

For the reasons given, the zones indicated in Fig. 2, which are characterized by high radioactivities, are considered as zeolites in spite of their low neutron porosity values; they are usually characterized by relatively low  $P_{ef}$  and  $\rho_b$  values which are also the cases shown by the recorded logs in Fig. 2.

The manifested absorption water contained in the interconnected void channels of zeolites is most likely displaced by potassium, thorium, and uranium which are transported from the nearby hydrothermally affected zones. Fig. 2 gives the evidence for this explanation; here the gamma ray spectral logs show erratic high values opposite the zeolitic zones. Moreover, the SP log proves the precipitation of zeolites by showing positive anomalies. This is related to the fact that zeolites are characterized by an excess of negative charges. Therefore, each counter-cation transferred from the zeolitic formation to the mud causes a positive SP potential in the mud.

## PYRITE

Pyrite is a sulphide mineral, iron sulphide,  $FeS_2$ . Pyrite in granite was found lining fractures and veins. It is deposited as a result of transportation process.

Unlike the usual rock minerals, pyrite exhibits good electrical conductivity, usually comparable to or higher than the conductivity of the formation water. It is a conduction of metallic (electronic) nature and, consequently, any transfer of current between water and pyrites involves a process of conversion from ionic to electronic conduction and vice versa [CLAVIER et al. 1976]. On the other hand,

pyrite is characterized by its dominant positive charges at its inner surface, which is in contact with less saline drilling mud. Hence, the pyritic zones will show negative SP anomalies. The depositional manner of pyrite along the fractures will govern the magnitude of the SP amplitude.

Density tools exhibit an apparent density of 4.985 g/cc in pyritic zones whereas the photoelectric cross section index,  $P_{ef}$ , indicates these zones by their high value (17 b/e). Because of these two distinctive characteristics of pyrite (high  $\rho_b$  and  $P_{ef}$  values) it is easy to recognize pyritic zones within the granite (see Fig. 2 where pyritic zones are indicated).

The neutron porosity from limestone matrix calibration shows low values in a pyritic matrix ( $\approx -2\%$ ).

## APPENDIX 2

Fig. 6 represents an analog electrical network composed of three independent network loops 1, 2 and 3 with loop currents  $I_1$ ,  $I_2$  and  $I_3$  respectively. The following two examples exhibit numerical values demonstrating the role of fracture between different electrochemically active minerals in modifying the SP anomalies (See also Fig. 7);

*Numerical Example 1:*

$$\begin{aligned} E_A &= 1.0 \text{ V} ; E_B = 2.0 \text{ V} ; E_a = 0.50 \text{ V} \\ R_A &= R_B = 100 \Omega ; R_{m1} = R_{m2} = R_{m3} = 10.0 \Omega \\ R_f &= 200 \Omega ; R_a = 300 \Omega \end{aligned}$$

By substituting these values into the related parameters of eqs. (4) through (14) one can obtain the following results, respectively:

$$I_1 = \frac{D_1}{D} = 0.0111 \text{ A}$$

$$I_2 = \frac{D_2}{D} = 0.0122 \text{ A}$$

$$I_3 = \frac{D_3}{D} = 0.0150 \text{ A}$$

The branch current in loop 2 will be:

$$I_1 - I_2 = -0.0011 \text{ A}$$

this means that the current will flow from the fracture to the borehole.

$$I_2 - I_3 = -0.0028 \text{ A}$$

this means that the current will flow from the chloritic zone to the borehole. The node voltages at the indicated nodes are given;

$$V_1 = -I_1 R_A + E_A = -0.1115 \text{ V}$$

$$V_2 = R_f (I_1 - I_2) = -0.2227 \text{ V}$$

$$V_3 = V_2 - I_2 R_{m2} = -0.3450 \text{ V}$$

$$V_4 = V_3 - I_3 R_{m3} = -0.4954 \text{ V}$$

### Numerical Example 2:

In this example all the proposed parameter values of the previous example have been retained with only one exception, namely the fracture aperture has been increased ten-fold. Hence the related resistance decreased to the one-tenth value, i.e. to  $R_f = 20 \Omega$ .

Accordingly, the calculations by means of eqs. (4) through (14) are given by the following, respectively;

$$I_1 = \frac{D_1}{D} = 0.0098 \text{ A}$$

$$I_2 = \frac{D_2}{D} = 0.0138 \text{ A}$$

$$I_3 = \frac{D_3}{D} = 0.0162 \text{ A}$$

The branch currents in loop 2 will be:

$$I_1 - I_2 = -0.0040 \text{ A}$$

this means that the current will flow from the fracture to the borehole.

$$I_2 - I_3 = -0.0024 \text{ A}$$

this means that the current will flow from the chloritic zone to the borehole.

The node voltages at the indicated nodes are given by;

$$V_1 = -I_1 R_A + E_A = 0.0183 \text{ V}$$

$$V_2 = R_f (I_1 - I_2) = -0.0800 \text{ V}$$

$$V_3 = V_2 - I_2 R_{m2} = -0.2180 \text{ V}$$

$$V_4 = V_3 - I_3 R_{m3} = -0.3800 \text{ V}$$

### APPENDIX 3

The petrophysical model represented by Fig. 9 is numerically evaluated here, in order to obtain a simulated SP curve which is close to the measured one. As can be seen from this figure the related analog electric network contains eight loops. More generally, a mathematical algorithm for simulating an electrical circuit consisting of  $K$  loops is suggested.

Without violating the generality of the formulation of the problem, the system of linear equations for an electric network containing  $K$  loops can be introduced by the following special band limited matrix:

$$\begin{vmatrix} -a_1 & 1 & \cdot & \cdot & \cdot & \cdot & \cdot & \cdot \\ -\tilde{a}_2 & -a_2 & 1 & \cdot & \cdot & \cdot & \cdot & \cdot \\ \cdot & -\tilde{a}_3 & -a_3 & 1 & \cdot & \cdot & \cdot & \cdot \\ \cdot & \cdot \\ \cdot & \cdot \\ \cdot & 1 \\ \cdot & \cdot & \cdot & \cdot & \cdot & \cdot & -\tilde{a}_k & -a_k \end{vmatrix} \begin{vmatrix} I_1 \\ I_2 \\ \cdot \\ \cdot \\ \cdot \\ \cdot \\ I_k \end{vmatrix} = \begin{vmatrix} b_1 \\ b_2 \\ \cdot \\ \cdot \\ \cdot \\ \cdot \\ b_k \end{vmatrix} \tag{15}$$

where  $\tilde{a}_m$  denotes the matrix elements standing only in the  $m$ th line, which is not in the main diagonal and it is not necessary for it to be equal to 0 or 1.

$I_m$  can be expressed by using only  $I_{m-1}, I_{m-2}$  in the form;

$$I_m = b_{m-1} + a_{m-1} * I_{m-1} + \tilde{a}_{m-1} * I_{m-2} \tag{16}$$

This formula is valid when  $m=3, 4, 5 \dots k$ , and after the definition of  $\tilde{a}_1 = 0.0$ , eq. (16) becomes valid for  $m=2$  as well.

The strategy followed for solving the system presented by eq. (15) is as follows: We denote  $I_1$  by  $X$  and using the 1, 2, ...( $k-1$ )th row of the system,  $I_2, I_3, \dots I_k$  are expressed in successive order and only with the aid of  $X$ . Then, the value of  $X$  can be obtained by using the  $k$ th row of equation system. Since  $X=I_1$ , equation (16) is now used to find the values  $I_2, I_3, \dots I_k$ .

As a realization of the above described process, a definition for  $X$ , and equation (16), in the case of  $m=2, 3, 4, \dots$ , is as follows:

$$I_1 = X \tag{17}$$

$$I_2 = b_1 + a_1 I_1 \tag{18}$$

$$I_3 = b_2 + a_2 I_2 + \tilde{a}_2 I_1 \tag{19}$$

$$I_4 = b_3 + a_3 I_3 + \tilde{a}_3 I_2 \tag{20}$$

We substitute the first eq. (17) of the system of equations (i.e the  $X$  value) into the right side of the second equation of system (18), and the new values of  $I_1$  and  $I_2$  (i.e. the second equation of the system), accordingly, have to be substituted into the right side of the next equation and so forth with respect to  $I_3, I_4$  etc. This is simply given by:

$$\begin{aligned} I_1 &= 0 + 1 \cdot X \\ I_2 &= b_1 + a_1 \cdot X \\ I_3 &= (b_2 + a_2 b_1) + (a_2 a_1 + a_2 \tilde{a}) \cdot X \\ I_4 &= (b_3 + a_3 b_2 + a_3 a_2 b_1 + a_3 \tilde{a} b_1) + (a_3 a_2 a_1 + a_3 a_2 \tilde{a} + a_3 \tilde{a} a_1) \cdot X \end{aligned}$$

However, the following equation represents the general term:

$$I_m = v_m + w_m \cdot X \quad (21)$$

So, as a result of the generation rule (16), it is not difficult to realize that both  $v_m$  (the constant part of  $I_m$ ) and  $w_m$  (the coefficient of  $X$ ), can be derived according to the sequences with non-constant coefficients as follows:

$$\begin{aligned} v_1 &= 0 \\ v_2 &= b_1 \\ &\vdots \\ &\vdots \\ &\vdots \\ v_m &= b_{m-1} + a_{m-1} \cdot v_{m-1} + a_{m-1} \tilde{a} \cdot v_{m-2} \end{aligned} \quad (22)$$

$$\begin{aligned} w_1 &= 1 \\ w_2 &= a_1 \\ &\vdots \\ &\vdots \\ &\vdots \\ w_m &= a_{m-1} \cdot w_{m-1} + a_{m-1} \tilde{a} \cdot w_{m-2} \end{aligned} \quad (23)$$

By substituting eq. (21), in the case of  $m = k$  and  $m = k-1$  into the last row of the system of eqs. (15), the result can be rearranged as follows;

$$-(a_k \cdot w_k + a_k \tilde{a} \cdot w_{k-1}) \cdot X = b_k + a_k \cdot v_k + a_k \tilde{a} \cdot v_{k-1} \quad (24)$$

By substituting eqs. (22) and (23), in the case of  $m = k+1$ , into eq. (24), the final formula is as follows:

$$X = - \frac{V_{k+1}}{W_{k+1}} \quad (25)$$

When the  $X$  becomes a known quantity, the values of  $I_2, I_3, \dots, I_k$  can be obtained sequentially by means of eq. (21).

### *Numerical Example:*

The trial and error technique is followed to determine the appropriate set of network parameters involved in the eight network equations describing the petrophysical model of Fig. 9. However, a computer optimization technique is recommended for future work in order to solve more complicated network models with efficient time and accuracy conditions. In the final stage of trial and error optimization the following set of network parameter values were obtained:

$$\begin{aligned} E_{b3} &= 0.60 \text{ V}, & E_{b2} &= 0.15 \text{ V}, & E_{b1} &= 1.00 \text{ V}, & E_{a5} &= 1.2 \text{ V} \\ E_{a4} &= 0.15 \text{ V}, & E_{a3} &= 0.45 \text{ V}, & E_{a2} &= 0.35 \text{ V}, & E_{a1} &= 0.3 \text{ V} \\ R_{m1} &= 23.70 \Omega, & R_{m2} &= R_{m3} = R_{m4} = R_{m5} = R_{m6} = R_{m7} &= 10.0 \Omega, \\ R_f &= 300.0 \Omega, & R_{a1} &= 100.0 \Omega, & R_{a3} &= 400.0 \Omega, & R_{a5} &= 150.0 \Omega \\ R_{a2} &= R_{a4} = R_{b1} = R_{b2} &= 200.0 \Omega, & R_{b3} &= 50.0 \Omega, & R_{m8} &= 18.10 \Omega \end{aligned}$$

The above explained mathematical steps, for  $k=8$ , have been followed by using these parameter values, and finally the following results were obtained:

*The loop currents are:*

$$\begin{aligned} I_1 &= 0.0029 \text{ A} \\ I_2 &= -0.0018 \text{ A} \\ I_3 &= 0.0002 \text{ A} \\ I_4 &= 0.0003 \text{ A} \\ I_5 &= 0.0016 \text{ A} \\ I_6 &= 0.0012 \text{ A} \\ I_7 &= 0.0023 \text{ A} \\ I_8 &= -0.0077 \text{ A} \end{aligned}$$

*The branch currents are:*

$$\begin{aligned} I_1 - I_2 &= 0.0047 \text{ A} \\ I_2 - I_3 &= -0.0019 \text{ A} \\ I_3 - I_4 &= -0.0002 \text{ A} \\ I_4 - I_5 &= -0.0012 \text{ A} \end{aligned}$$

$$\begin{aligned} I_5 - I_6 &= 0.0004 \text{ A} \\ I_6 - I_7 &= -0.0011 \text{ A} \\ I_7 - I_8 &= 0.0100 \text{ A} \end{aligned}$$

The node voltages at the indicated nodes are given by;

$$V_4 = R_f(I_3 - I_4) = -0.0452$$

$$V_3 = V_4 + R_{m3}I_3 = -0.0433$$

$$V_2 = V_3 + R_{m2}I_2 = -0.0611$$

$$V_1 = V_2 + R_{m1}I_1 = 0.0081$$

$$V_5 = V_4 + R_{m4}I_4 = -0.0486$$

$$V_6 = V_5 + R_{m5}I_5 = -0.0645$$

$$V_7 = V_6 + R_{m6}I_6 = -0.0761$$

$$V_8 = V_7 + R_{m7}I_7 = -0.0990$$

$$V_9 = V_8 + R_{m8}I_8 = -0.0408$$

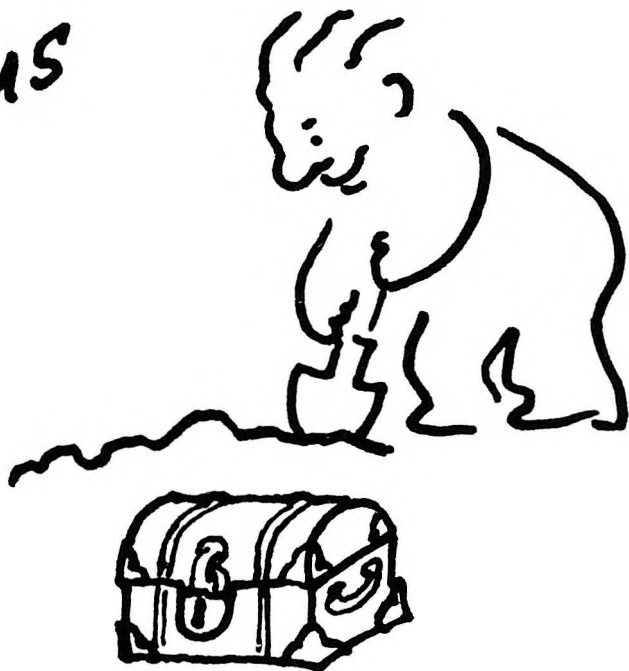
With the optimized set of network parameters there is a fairly good agreement between the estimated SP curve and the measured one, which proves the usefulness of the above explained method.

## SP SZELVÉNYEZÉS TULAJDONSÁGAI GRÁNIT TÁROZÓBAN

Ali Belgasem BOURIMA

A legtöbb magmás kőzet esetében a spontán potenciál (SP) szelvényezés válaszgörbéi nem jellegetesek, mivel ezen kőzetek nem rendelkeznek olyan elektrokémiai aktivitással, mely szükséges az SP anomáliák létrejöttéhez. Egyes esetekben azonban, a magmás kőzet ásványos-szerkezetét elektrokémiaiailag aktív ásványok gazdag kifejlődése jellemzi, mint például agyagásványok, zeolitok és pirit. Ezekben az esetekben jelentős SP anomáliák rögzíthetők. A líbiai Sirte-medencében található Nafóra-Augila mezőben ilyen SP anomáliákat rögzítettek egy gránit tározóban. A cikk ezeket az anomáliákat vizsgálja és a hozzájuk kapcsolódó geokémiai és hidrodinamikai hátteret tárja fel. Elméleti kőzettani modelleket dolgoz ki, melyek az elektrokémiaiailag aktív ásványok által generált elektromotoros erők, valamint a kőzet-repedések anomália kialakulásához való hozzájárulásán alapszik.

Strike oil  
by advertising  
with us



**GEOPHYSICAL TRANSACTIONS OFFERS YOU  
ITS PAGES TO WIDEN THE SCOPE OF YOUR  
COMMERCIAL CONTACTS**

Geophysical Transactions,  
contains indispensable information  
to decision makers of the geophysical  
industry. It is distributed to 45  
countries in 5 continents.

**Advertising rates (in USD)**

	Page	Half page
Black and white	400/issue	250/issue
Colour	800/issue	450/issue

Series discount: 4 insertions — 20%

For further information, please contact:  
Geophysical Transactions, Eötvös Loránd Geophysical Institute of Hungary

P.O.B. 35, Budapest, H-1440, Hungary  
tel: (36-1) 163-2835      telex: 22-6194  
fax: (36-1) 163-7256





# EÖTVÖS L. GEOPHYSICAL INSTITUTE OF HUNGARY

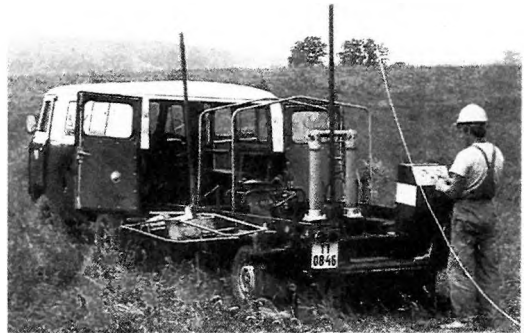
THE OLDEST INSTITUTION FOR APPLIED GEOPHYSICS  
OFFERS THE LATEST ACHIEVEMENTS FOR  
GROUND-WATER PROSPECTING  
and  
ENVIRONMENTAL PROTECTION

The most often occurring demands:

- local geophysical measurements for the water supply of small communities by a few wells
- regional geophysical mapping to determine hydrological conditions for irrigation, regional agricultural development,
- large-scale exploration for the water supply of towns, extended areas i.e. regional waterworks,
- determination of bank storage of river terraces, planning of bank filtered well systems,
- thermal water exploration for use as an energy source, agricultural use or community utilization,
- cold and warm karst water prospecting,
- water engineering problems, water construction works



*The Maxi-Probe electromagnetic sounding and mapping system – produced under licence by Geoprobe Ltd. Canada – is an ideal tool for shallow depths, especially in areas where seismic results are poor or unobtainable*



*ELGI has a vast experience in solving problems of environmental protection such as control of surface waters, reservoir construction, industrial and communal waste disposal, protection of surface and ground water etc. ELGI's penetrolgger provides in-situ information – up to a maximum depth of 30 m – on the strength, sand/shale ratio and density without costly drilling.*



*Field work with ELGI's 24 channel portable seismograph*

**ELGI offers contracts with co-operating partners to participate in the whole complex process of exploration–drilling–production.**

**For further information ask for our booklets on instruments and applications. Let us know your problem and we will select the appropriate method and the best instrument for your purpose.**

*Our address: ELGI POB 35. Budapest,  
H-1440. HUNGARY  
Telex: 22-6194 elgi h*

# ALLIED ASSOCIATES GEOPHYSICAL LTD.

79-81 Windsor Walk Luton Beds England LU1 5DP Tel: (0582) 425079 Telex: 825562 Fax: (0582) 480477

## UK's LEADING SUPPLIER OF RENTAL GEOPHYSICAL, GEOTECHNICAL, & SURVEYING EQUIPMENT

### SEISMIC EQUIPMENT

Bison IFF 9000 Seismograph  
ABEM Mark III Seismograph  
Nimbus ES1210F Seismograph Complete  
Single Channel Seismograph Complete  
DMT-911 Recorders  
HVB Blasters  
Geophone Cables 10.20.30M Take Outs  
Geophones  
Single Channel Recorders  
Dynasource Energy System  
Buffalo Gun Energy System

### MAGNETICS

G-856X Portable Proton Magnetometers  
G-816 Magnetometers  
G-826 Magnetometers  
G-866 Magnetometers

### GROUND PROBING RADAR

SIR-10 Consoles  
SIR-8 Console  
EPC 1600 Recorders  
EPC 8700 Thermal Recorders  
120 MHz Transducers  
80 MHz Transducers  
500 MHz Transducers  
1 GHz Transducers  
Generators  
Various PSU's  
Additional Cables  
Distance Meters

### GRAVITY

Model 'D' Gravity Meters  
Model 'G' Gravity Meters

### EM

EM38  
EM31 Conductivity Meter  
EM16 Conductivity Meter  
EM16/16R Resistivity Meters  
EM34 Conductivity Meter 10, 20, 40M Cables  
EM37 Transient EM Unit

### RESISTIVITY

ABEM Terrameter  
ABEM Booster  
BGS 128 Offset Sounding System  
BGS 256 Offset Sounding System  
Wenner Array

*In addition to rental equipment we currently have equipment for sale. For example ES2415, ES1210F, EM16/16R, G-816, G856, G826/826A, equipment spares*

**NOTE:** Allied Associates stock a comprehensive range of equipment spares and consumables and provide a repair & maintenance service.

*We would be pleased to assist with any customer's enquiry*

**Telephone (0582) 425079**

**Place your order through our first agency in Hungary.**

To place an order, we request the information listed in the box below.

1. Customer name  
(a maximum of 36 characters)
2. Customer representative
3. Shipping address
4. Mailing or billing address  
(if different)
5. Telephone, Telex or Fax number
6. Method of shipment

**ELGI c/o L. Veró**

Columbus St. 17-23

H - 1145 Budapest, Hungary

PHONE: 36-1-1637-438

FAX: 36-1-1637-256

*\* Orders must be placed and prepaid with ELGI.*

**SOFTWARE**  
*for Geophysical and  
Hydrogeological  
Data Interpretation,  
Processing & Presentation*

**INTERPEX  
LIMITED**

715 14th Street ■ Golden, Colorado 80401 USA ■ (303) 278-9124 FAX: (303) 278-4007

## *Copyright*

Authorization to photocopy items for internal or personal use in research, study or teaching is granted by the Eötvös Loránd Geophysical Institute of Hungary for individuals, instructors, libraries or other non- commercial organizations. We permit abstracting services to use the abstracts of our journal articles without fee in the preparation of their services. Other kinds of copying, such as copying for general distribution, for advertising or promotional purposes, for creating new collective works, or for resale are not permitted. Special requests should be addressed to the Editor. There is no charge for using figures, tables and short quotes from this journal for re-publication in scientific books and journals, but the material must be cited appropriately, indicating its source.

Az Eötvös Loránd Geofizikai Intézet hozzájárul ahhoz, hogy kiadványainak anyagáról belső vagy személyes felhasználásra kutatási vagy oktatási célokra magánszemélyek, oktatók, könyvtárak vagy egyéb, nem kereskedelmi szervezetek másolatokat készítsenek. Engedélyezzük a megjelentetett cikkek összefoglalóinak felhasználását referátumok összeállításában. Egyéb célú másoláshoz, mint például: terjesztés, hirdetési vagy reklám célok, új, összefoglaló jellegű anyagok összeállítása, eladás, nem járulunk hozzá. Az egyedi kéréseket kérjük a szerkesztőnek címezni. Nem számolunk fel díjat a kiadványainkban szereplő ábrák, táblázatok, rövid idézetek más tudományos cikkben vagy könyvben való újrafelhasználásáért, de az idézés pontosságát és a forrás megjelölését megkivánjuk.

